出藍　第 38 号

2025 年 4 月

目次

【解説記事・紹介記事】

【口頭発表】

【修士論文】

Colloids and Surfaces A: Physicochemical and Engineering Aspects 688 (2024) 133572

Contents lists available at ScienceDirect

Colloids and Surfaces A: Physicochemical and Engineering Aspects

journal homepage: www.elsevier.com/locate/colsurfa

Effects of scanning direction and remelting on surface morphology and wettability of laser powder bed fusion Ti6Al4V mono- and bi-layers

Zhenjun Li [a,*], Masayoshi Mizutani [b]

[a] School of Engineering, Tokyo University, Japan
[b] Graduate School of Engineering, Tohoku University, Japan

GRAPHICAL ABSTRACT

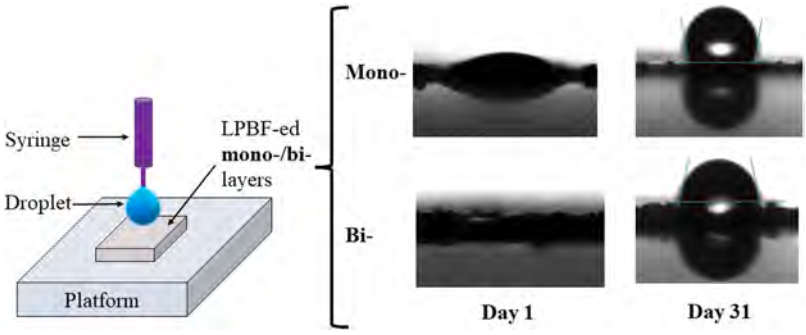

ARTICLE INFO

Keywords:
Ti6Al4V
Mono- and bi-layers
Contact angle
Surface morphology
LPBF

ABSTRACT

Laser powder bed fusion manufactured (LPBF-ed) porous Ti6Al4V materials have attracted much attention in the biomedical industry due to their functional properties. In this study, mono- and bi-layer LPBF-ed surfaces were prepared to better understand the dynamics of pore formation and the impact of one layer on the next. The powder spreading direction was regarded as the direction here, and then LPBF-ed surfaces could be defined as x- and y- scanned ones. As for LPBF-ed monolayers, the y-scanned surface was rougher than the x-scanned surface, in good agreement with the surface profile of the powder layer extracted from the numerical work. The finding indicates that the morphology of LPBF-ed layers is affected by the relationship between the powder spreading direction and the laser scanning direction. Besides, surfaces scanned with varying laser numbers were used to analyze the effect of the remelting phenomenon, which confirmed that additional laser scans prone to reshaping the pore distribution. The wettability was further studied to investigate their biocompatibility initially. No obvious changes were observed between the CAs of the x- and y-scanned surfaces, whereas the remelting accelerated the surface stabilization of LPBF-ed monolayers. LPBF-ed bilayers were much rougher and more hydrophilic compared to monolayers, and the same result could be verified on xy- and yx-scanned surfaces. The study contributes to better control pores and even performance within LPBF-ed samples by investigating the surface morphology and wettability of LPBF-ed layers.

* Correspondence to: 2-22 Shirakata Shirane, Tokai, Naka, Ibaraki 319-1188, Japan
E-mail address: lizhenjun@g.ecc.u-tokyo.ac.jp (Z. Li).

https://doi.org/10.1016/j.colsurfa.2024.133572
Received 23 December 2023; Received in revised form 28 January 2024; Accepted 23 February 2024
Available online 24 February 2024

1. Introduction

The Ti6Al4V alloy is one of the promising biomaterials because of its excellent biological and mechanical performance [1–3]. However, current Ti6Al4V bioimplants are easily leading to bone tissue resorption due to the high elastic modulus of commercial bulk Ti6Al4V materials [4]. To narrow the differences between Ti6Al4V materials and bones, materials with porous structures have been introduced into the biomedical field [3,5]. A significant decrease in elastic modules has been achieved by using lattice structures [6,7] that even include hierarchical porous structures [8] or controlling laser parameters such as laser power, scan speed, and hatch distance [9] in additive manufacturing (AM) technology. Special lattice structures always put forward strict requirements on CAD design, whereas the latter only adopts simple solid design. Thus, adjusting processing parameters has been an effective way to develop AM materials such as Ti6Al4V. Further, samples with high pore volume were reported to promote tissue generation and integration [10] in the biomedical field.

Among all kinds of AM techniques, the LPBF technology has attracted considerable attention in fabricating porous structures with desired mechanical properties due to its advantages in generating high-resolution features and internal passages, and maintaining dimensional control [11,12]. Based on the track-by-track and layer-by-layer features of LPBF, Dilip et al. [5] produced single-track deposits and bulk samples by verifying laser power and scan speed, and confirmed that the width of the track reduces at a low power level and high scan speed, and the depth of penetration of the melt pool decreases with slower scan speed, leading to changes in porosity in the bulks parts. Stamp et al. [13] easily obtained porous structure with controlled porosity through a beam overlap procedure (i.e. laser hatch spacing), and confimed a microtexture and spherical metal powder particles on the as-built LPBF manufactured (LPBF-ed) surfaces. In both cases, porous samples with various pore size and porosity were successfully fabricated by controlling laser parameters because of unmelted powders caused by low laser energy and gas atmospheres. However, the correlation between pores and laser parameters deserves further study to precisely control their microstructures and performance.

Except for the above-mentioned changes in the pores of LPBF Ti6Al4V samples, changes in the surface morphology [14] also play a key role in improving the biocompatibility through significant effects on wettability [15,16]. Song and Fan [17] investigated synergistic effects of surface roughness coupled with temperature and pressure on contact angle and proved that the droplet on a rougher surface corresponded to a lower contact angle when temperature and pressure were the same. Besides, special structures like the rectangle convex structure [18] and microgrooves [19], were produced on the surface to optimize the wettability. Evenmore, many mechanical and chemical surface modification techniques were also used to optimize the bioactive character of Titanium-based biomaterials. Cotrut et al. [20] highlighted differences in wettability, roughness, in vitro corrosion resistance, and biomineralization ability of different modified Ti-based biomaterials, and demonstrated that surface properties can be controlled and enhanced by modifying the roughness and reducing internal tension in the superficial layer. Huang et al. [21] analyzed the wettability, and biocompatibility of Ti-based surfaces and showed that a high contact angle surface corresponds to high compatibility. All these works prove the necessity of investigation in wettability for biomedical applications as it is highly related to biocompatibility. Furthermore, the layer-stacking process makes the surface morphology of a single layer closely related to the pores of the bulk LPBF-ed sample. Thus, investigation of LPBF-ed monolayers and bilayers is beneficial to clarify the pore formation mechanism in LPBF-ed samples.

Considering the general scanning strategy consisting of straight lines pattern with a rotation of 90° between each successive layer [22], monolayer surfaces scanned by 0° (x) and 90° (y) lasers referring to the powder spreading direction, and bilayer surfaces of xx and yx were characterized to compare the formation dynamics of pores and their distribution, as well as the corresponding wettability. In addition to changing laser parameters (laser power, laser scanning speed, and laser hatching spacing to promote pore vacancies by lowering the average laser energy), the remelting also has been shown to effectively modify both surface and interior pore vacancies [23–25]. Thus, monolayer and bilayer surfaces under different laser scans were also prepared and characterized in the study. The study is expected to control and reshape pores and even modify their wettability of LPBF-ed Ti6Al4V samples.

2. Experimental methodology

2.1. Preparation of LPBF-ed layers

An LPBF machine ProX100 (3D systems) was used to sinter powders on a wrought Ti6Al4V plate (100 ×100×10 mm^3). A fiber laser with a spot diameter of 80 μm and wavelength of 1070 nm is packed inside the 3D printer. The Ti6Al4V powder used in the study has a gaussian distribution with an average value of 18 μm.

Based on its layer-by-layer stacking process [13], a single layer and double layers were developed to investigate the combination performance with the basic plate. Considering the roller rolling direction ν, the same direction as ν is x, and the direction perpendicular to ν is y. The combinations of xx and yx were formed when the laser tracks in the second layer were all parallel to ν, which could be used to compare the impact of overlayer strategies and identify mechanisims of the inner pore generation. Fig. 1 displays the detailed design.

2.2. Extraction and characterization of powder bed surface

Due to the limitations of the closed chamber of packaging 3D printers, powders spread on the base plate are difficult to be characterized using morphological analysis equipment. Instead, the powder spreading process was numerically investigated with the help of the software EDEM to study the powder distribution in the x and y directions (defined as Section 2.1). Physical models and methodologies have been described in the previous publication [26]. To allow enough powders spread on the base plate, the roller and bed in Fig. 2 were enlarged to dimension of Φ0.3 mm×2.4 mm and 8 mm×2.4 mm×0.5 mm, respectively. Particles from the paved particle layer will be extracted to

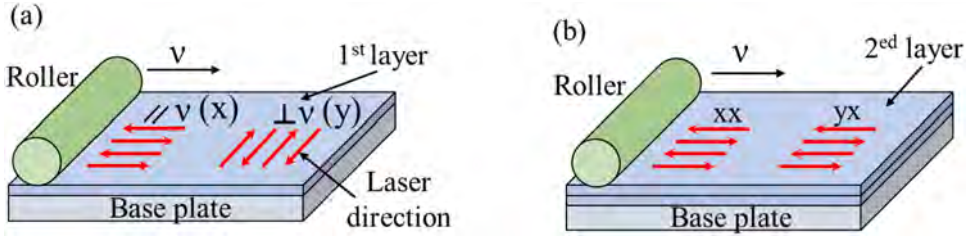

Fig. 1. Schematic diagram of the LPBF-ed layers prepared by different laser trajectories: (a) x- (parallel to ν) and y- (vertical to ν) scanned monolayers, (b) xx- and yx-scanned bilayers.

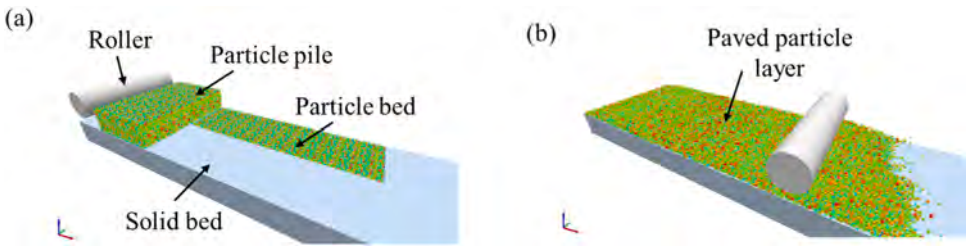

Fig. 2. The DEM model for generating a paved particle layer, (a) geometry details with particle piles; (b) a paved particle layer after the roller rolling.

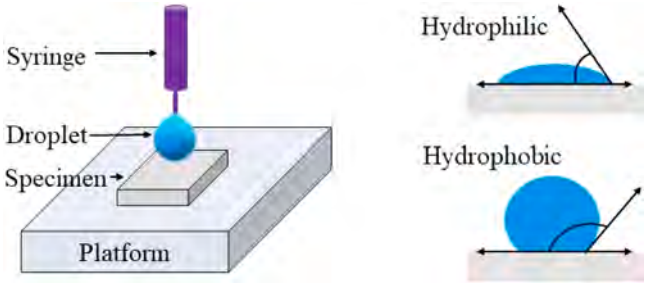

Fig. 3. Schematic diagram of contact angle measurement.

analyze the surface topography, and then compute the particle distribution in the x and y directions. The particle position and diameter data were exported from the DEM model and then the top surface was rebuilt using MATLAB. Five cross-sectional curves in each direction (x and y) were extracted to get the wettability-related parameter roughness factor, which reflects the difference in particle distribution.

2.3. Contact angle measurement

To evaluate the wettability of the above LPBF-ed mono- and bi-layers, an automatic contact angle meter (DM-501Hi, KYOWR, Japan) was used to measure the contact angle. The sessile drop method was adopted, and the contact angle was measured 2000 ms after a 0.5 μL water drop impacted the surface. The specific schematic diagram shows in Fig. 3, and water drops on specimens will show different shapes driven by the hydrophilic (contact angle less than 90°) or hydrophobic (contact angle greater than 90°) nature.

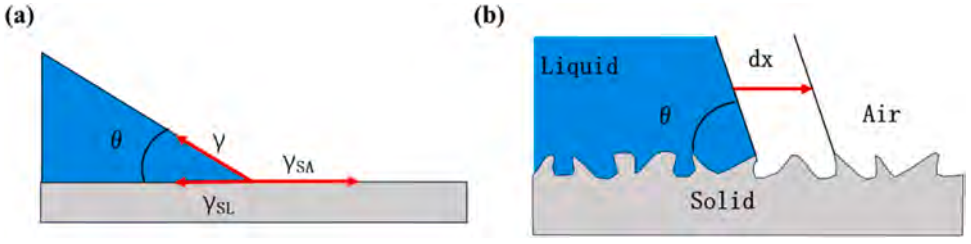

Fig. 4. Illustration of the contact angle of different surface: (a) ideal wettability, (b) Wenzel model.

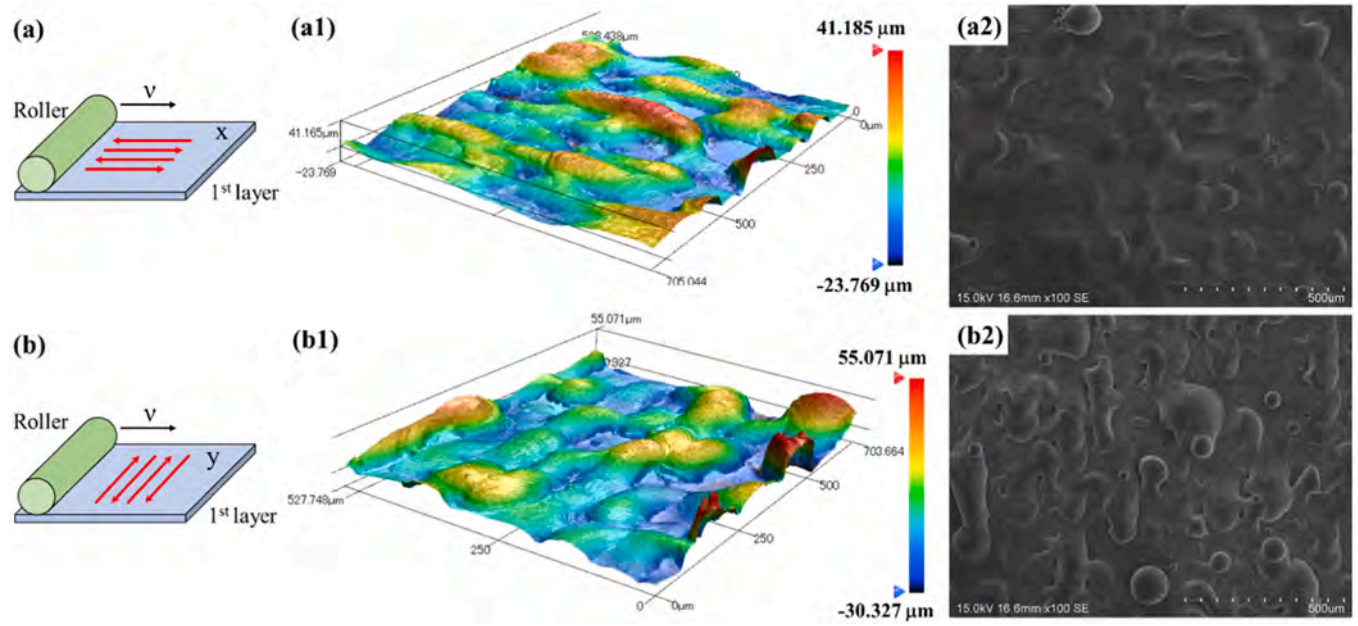

Fig. 5. LPBF-ed monolayer surfaces: (a)~(a2) the x-scanned surface; (b)~(b2) the y-scanned surface.

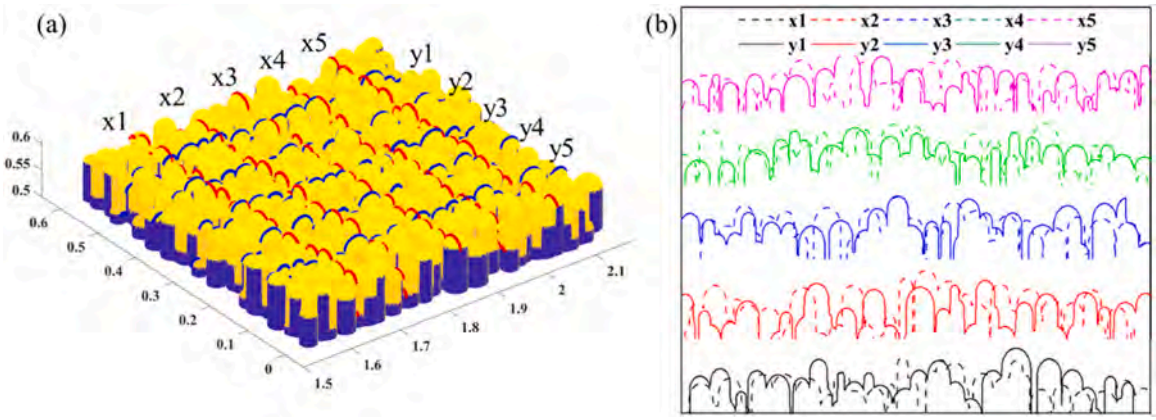

Fig. 6. Contours of a powder bed in the x and y directions, (a) the surface morphology of the powder bed and the location of the contours, (b) Two-dimensional curves of the contours.

2.4. Wettability theory

The difference in surface energy acting on the contact line of different material phases provides the equilibrium condition of a droplet. The contact angle (CA) is thus fixed and expressed as Eq. (1).

$$\cos\theta = \frac{\gamma_{SG} - \gamma_{SL}}{\gamma_{LG}} \tag{1}$$

Where γ_{SG}, γ_{SL}, and γ_{LG} are surface energies of solid-gas, liquid-gas and solid-liquid interfaces, respectively [27]. For a rough surface, the drop spread on it until an equilibrium point is reached, as sketched in Fig. 4 (b). The liquid/gas interface is replaced by solid/liquid interface when the contact line extends on the rough surface. Based on a geometrical argument factor r introduced by Wenzel [27], the surface energy variation dE arising from an apparent displaces dx of the line (per unit length of the contact line) can be written as Eq. (2).

$$dE = r * (\gamma_{SL} - \gamma_{SG})dx + \gamma_{LG} * dx * \cos\theta^* \tag{2}$$

Where the roughness factor r is the ratio between the actual surface area and the apparent surface area of a rough surface. The minimum of E (dE=0) yields Eq. (1) if the solid is flat (r=1); if not, the contact angle obeys Eq. (3).

$$\cos\theta^* = r * \cos\theta \tag{3}$$

Where θ is the chemical angle given by Eq. (1). Eq. (3) predicts that roughness enhances wettability. Further, the wicking phenomenon is involved once the material is not fully filled. The droplet gently deposited spreads and stops when it is surrounded by primarily non-wetting defects.

2.5. Surface characterization

The surface topography was measured using a shape analysis laser microscope (Keyence VK_X1100) with a resolution of 0.5 × 1 nm (height × width). Thus, the digital data were collected, which could then be used for quantitatively assessing the surface parameters. An SEM system (SU1510) was further used to obtain the high-resolution images to supplement the surface morphology.

3. Results and discussions

As mentioned above, different LPBF-ed layers were prepared and

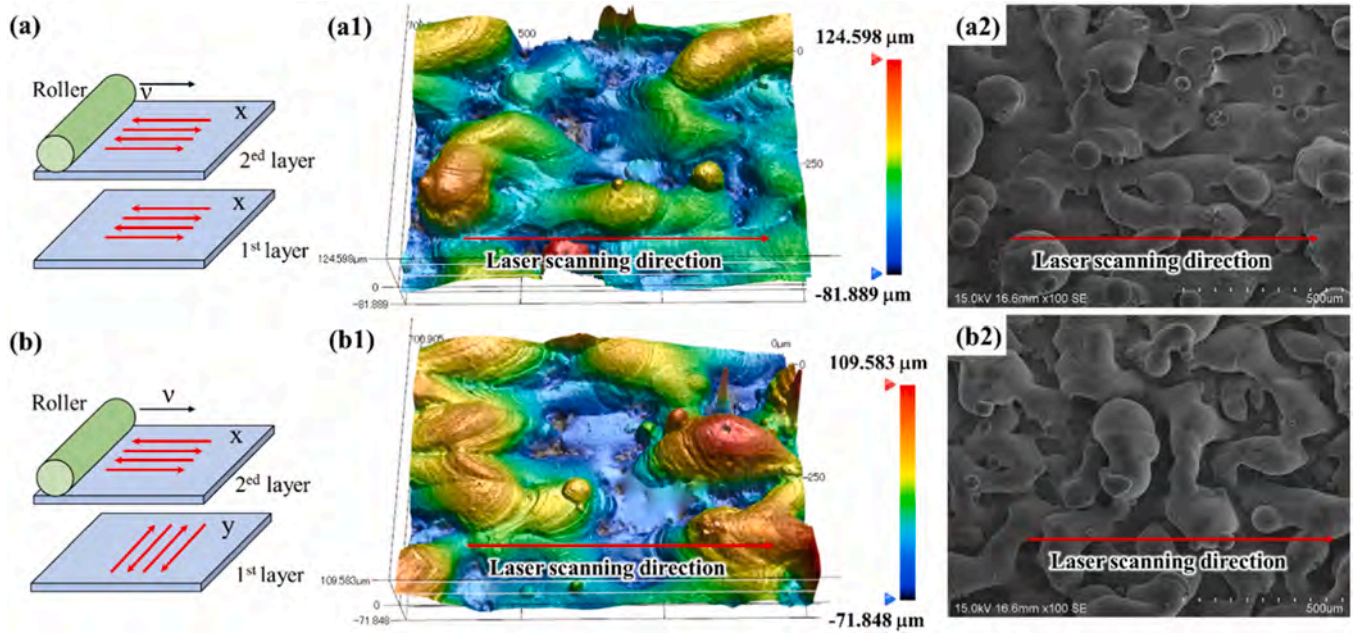

Fig. 7. LPBF-ed bilayer surfaces: (a)~(a2) the xx surface; (b)~(b2) the yx surface.

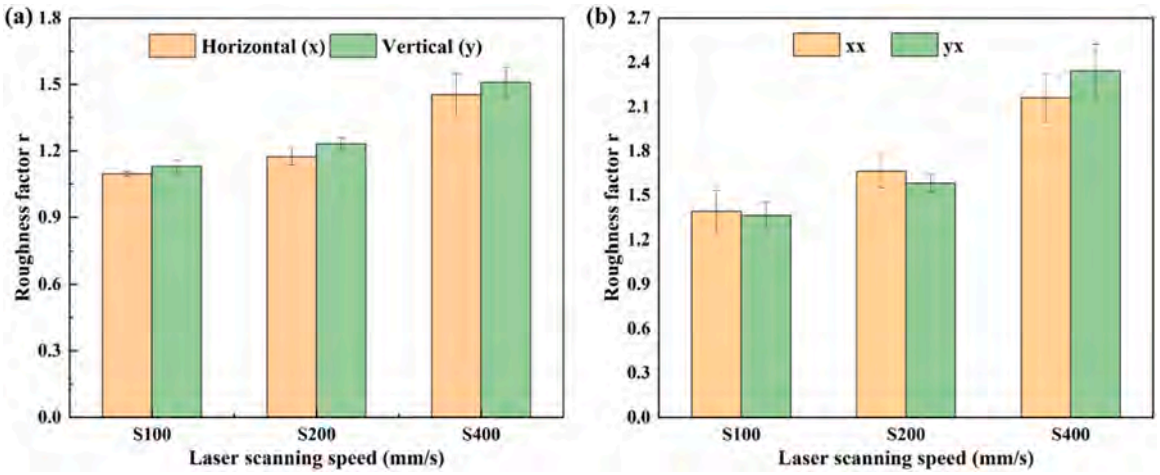

Fig. 8. Roughness factor r_{surf} of LPBF-ed (a) x- and y- scanned monolayer surfaces; (b) bilayer surfaces xx and yx.

characterized to study the effects of laser scanning direction and the laser scans (remelting) on the microstructure and performance of LPBF-ed materials.

3.1. Laser scanning directions

Fig. 5 shows x- and y- scanned LPBF-ed monolayer surfaces, where Fig. 5(a)~(a2) show details of the monolayer x, and Fig. 5(b)~(b2) show details of the monolayer y. Both surfaces were obtained at laser scanning speeds (LSS) of 200 mm/s, laser power of 50 W and laser hatching spacing of 80 μm. Obvious boundaries between adjacent tracks appeared on both monolayer surfaces, but more unmelted powders were kept on the monolayer y compared to the monolayer x. Considering the generally two steps of the LPBF process: spreading powders on a base plate and then sinter the powder layer using a laser. The laser parameters used here were the same, therefore, the differences in surface morphology most likely originate from the powder spreading process. Further referring to the work reported by other scholars on the effect of powder spreading process [28,29], the quality of a single powder spreading layer was considered to find out the reasons for the difference in x- and y- scanned monolayers. Fig. 6 shows the contours of a powder layer extracted from EDEM simulation results. Similarly, the direction x here refers to the direction in which the roller moves, whereas y is vertical to x. All these contours consisted of many arcs, which were boundaries of spherical particles.

The morphologies of bilayers xx and yx were compared in Fig. 7. Surfaces xx and yx were typical as-built LPBF surfaces [14,22], but with different pore distributions due to the different laser scanning directions of their 1st layers. The material in surface xx (Fig. 7(a2)) was connected and extended in direction x, whereas materials in surface yx (Fig. 7(b2)) were even able to extend in the direction y, which can be attributed to the error remapping of the surface morphology of the 1st layer. Further, the 1st layer become the substrate of the 2nd layer, and thus, the powder spreading process of the 2nd layer has become spreading powders on a rough surface (as Fig. 5 (a2) and (b2) shown). The powder-spreading process of the 2nd layer was significantly different from that of the 1st layer therefore. Xiang et al. [30] have proved that the substrate surface significantly affected the packing density of powders, and a substrate with a rough surface resulted in the deposition of more powder particles, and even more, the difference in packing density was also confirmed when rotated the texture orientation. Same with Fig. 5 (a2) and (b2), the 1st layers of the bilayers xx and yx differed not only in surface roughness but also in texture orientation, leading to different packing density of the 2nd powder layer. On one hand, powders with different packing density results in changes in laser absorption and heat conduction, and then, affects the sintering quality of the 2nd layer. On the other hand, the rough monolayer surfaces confirmed in Fig. 5 will affect the flow of molton materials in the 2nd layer. Further controlled by the surface tension of molten Ti6Al4V, the LPBF-ed xx and yx surfaces with different surface morphologies and inner pores were generated.

The above-mentioned LPBF-ed layers were verified to have different surface morphologies, and further quantitative comparison was done to reveal its relationship with wettability. As introduced in Section 2.4, the roughness factor r plays a vital role in determining contact angle (CA). r of a rough surface r_{surf} is calculated according to Eq. (4), and r of a rough contour r_{cont} is defined as Eq. (5).

$$r_{surf} = \frac{S_{surf}}{S_{proj}} \tag{4}$$

$$r_{cont} = \frac{L_{cont}}{L_{proj}} \tag{5}$$

Where S_{surf} is the total area of the surface and S_{proj} is the area of its projection, L_{cont} is the total length of the curve and L_{proj} is its projected length. Fig. 8(a) and (b) show the results of roughness factor r_{surf} of mono- and bi- layers, respectively. The error bars here were obtained from 5 measurements. Overall, r_{surf} increases as laser scanning speed (LSS) increases. Ishibashi et al. [31] observed that the top surface of LPBF-ed samples become rougher as LSS increases, which was well agreed with the increasing trend of r_{surf} here. Compared with monolayer x fabricated under the same laser parameters, monolayer y always has a higher r_{surf}, which coincides well with surface morphology shown in Fig. 5. Surface roughness factor r_{cont} of curves in Fig. 6 was calculated to figure out the possible cause of the phenomenon. r_{cont} of the x-profile line of a particle layer was 16.155 μm, whereas r_{cont} of its y-profile line was 17.221 μm. The surface roughness factor of the powder layer was much higher than that of an LPBF-ed surface, but they all followed the rule that r in the y direction is larger than that in the x direction. Powder particles were melted and then flowed to nearby lower areas due to gravity, leading to a flatter surface compared to the original particle surface [32]. Thus, the roughness factor r of an LPBF-ed surface (less than 3 μm) is much smaller than that of a particle layer surface (more than 15 μm). Simultaneously, the greater inhomogeneity of the particle distribution in the y direction caused the LPBF-ed monolayer surface y to be rougher than the surface x, i.e., r_{surf} of y is larger than that of x. Particles spread along the direction y were due to the roller rolling on the bed substrate whereas particles spread along the direction x were due to the roller having a certain length, leading to differences in non-uniformity of particle distribution in directions x and y.

However, the change in the roughness factor of the bilayer surface is inconsistent with that of LPBF-ed monolayers. As described in Fig. 7, surfaces xx and yx were greatly dominated by the morphology of the 1st

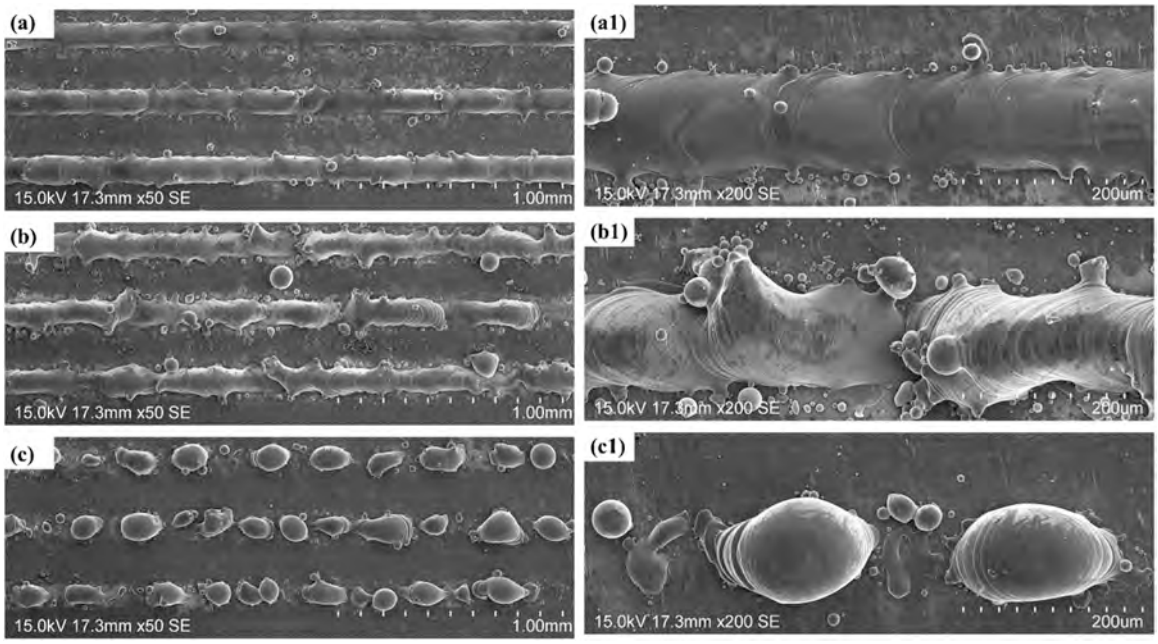

Fig. 9. SEM images of single tracks at increasing laser scanning speeds of (a) 100 mm/s, (b) 200 mm/s, and (c) 400 mm/s, and (a1) ~(c1) are their enlarged images, respectively.

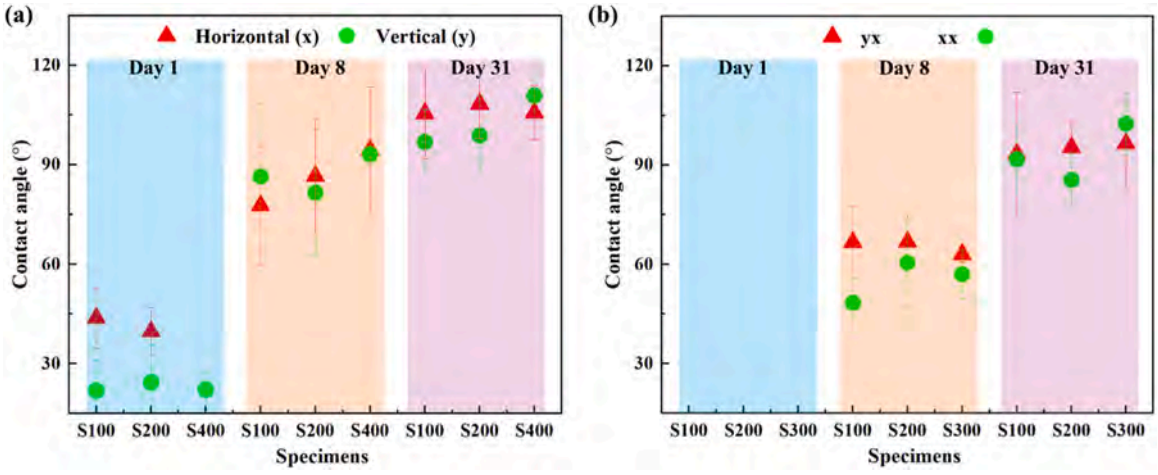

Fig. 10. Results of CA on different days: day 1, day 8 and day 31. (a) x- and y- scanned monolayer; (b) bilayer surfaces yx and xx.

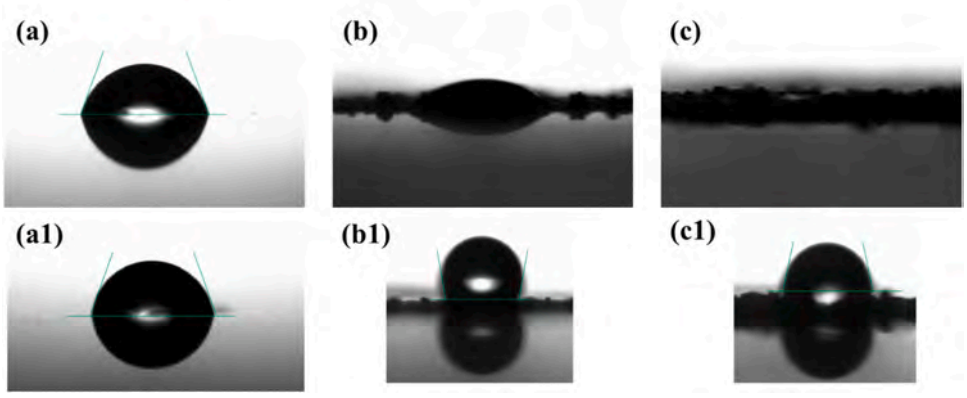

Fig. 11. Wettability of: (a) wrought bulk Ti6Al4V, (b) monolayer, and (c) bilayer on day 1, and (a1) ~(c1) are their corresponding results on day 31, respectively.

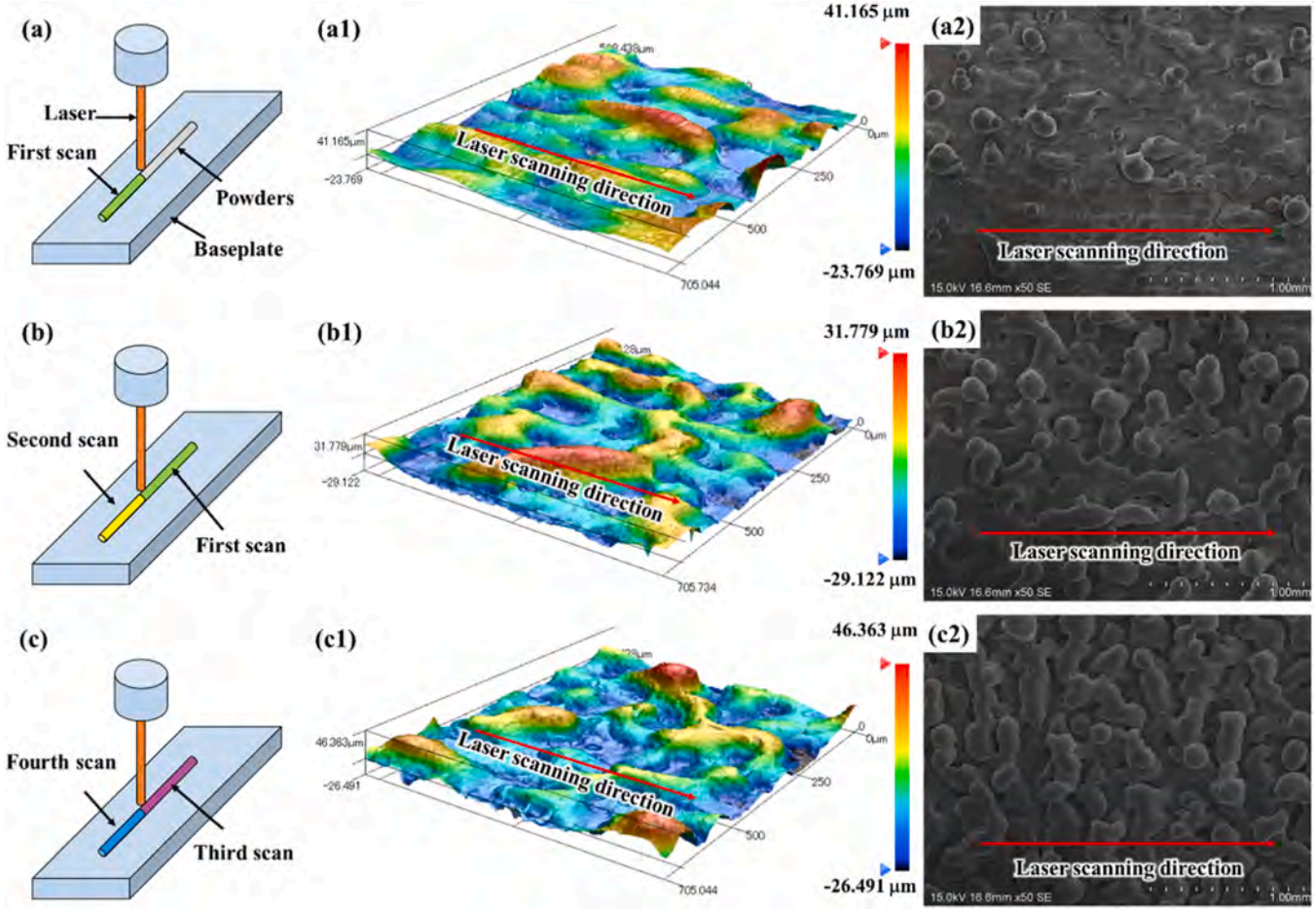

Fig. 12. LPBF-ed monolayer under different laser scans: (a)~(a2) one scan; (b)~(b2) two scans, and (c)~(c2) four scans.

sintered layer. As for bilayer surfaces S100 and S200, r_{surf} of yx is lower than that of xx. The fully overlapping 2nd laser scan trajectories of the surface xx allowed for in situ material stacking because the rapid condensation of molten material limited its ability to fill the pores generated in the 1st layer, especially boundary pores. The 2nd laser scan trajectories of surface yx avoided completely aligning high-energy laser area, resulting in a more uniform surface. Meanwhile, boundary pores formed in the 1st LPBF-ed layer were easier filled, forming samples with less pores. As for the bilayer surface yx, the elimination of boundary pores significantly reduced the maximum height difference and resulted in a lower r_{surf}. However, the bilayer surface S400 didn't obey the rule. To better explain the abnormality, single tracks under changing laser scanning speeds (LSS) were supplemented. Fig. 9 shows the surface morphology of single tracks under different LSS, and it reveals an significant difference at a speed of 400 mm/s. Materials on the track S400 were unable to continuously connect with each other, generating separate metal balls on the scanning track. At the case, the fraction of track pores (pores appeared on the laser scan trajectory) exceeded that of boundary pores (pores appeared between two adjacent laser scans), and become the dominant in forming the LPBF-ed bilayer surface. When a same laser scan was irradiated on it, more molten material filled these track pores, leading to a relative small surface roughness factor r_{surf}. In a sum, the layer stacking process is too complicated to summarize into one trend under changing laser parameters, but the roughness factor of bilayer was higher than that of the monolayer under same laser scanning speed, indicating that the surface quality deteriorates with increasing number of layers. The rough surface will facilitate the formation of inner pores in LPBF-ed samples.

Fig. 10 summarizes the contact angle of above-mentioned mono- and bi- layers. As time goes by, the hydrophobicity of LPBF-ed samples gradually improved, which can be seen from the increasing contact angles (CA). A similar surface wettability trend was reported by Zhang et al. [16] in their study on laser-induced plasma micromachined Ti6Al4V surfaces. CA of the monolayer was larger than that of the bilayer on the same day. Even more, droplets on the bilayer surface were absorbed quickly on day 1 (the same as Fig. 11(c)), and no CA was obtained. Note that all LPBF-ed layers were still sintered on the wrought Ti6Al4V base plate, which could be regarded as a total dense Ti6Al4V material, whose CAs were also measured (as shown in Fig. 11 (a) and (a1)). The combination of LPBF-ed layers and base plate was therefore regarded as a graded material. Fig. 11 (b), (c), (b1), and (c1) show CAs of these graded materials. The CAs on both day 1 and day 31 demonstrate that the bilayer surface is more hydrophilic compared to the monolayer surface, indicating the stacking thinkness has vital affect on wettability. Further, LPBF-ed layers indeed promotes the hydrophilicity compared to the dense Ti6Al4V.

Specificly, a larger θ^* corresponds a smaller surface factor r when the constant θ is smaller than 90° according to Eq. (3). As shown in Fig. 8 (a), the x-scanned monolayer was with a larger CA, but a smaller r compared with the y-scanned monolayer, which agrees well with Eq. (3). But as time goes by, there is no obvious difference between x- and y-scanned monolayers. As for bilayers, the CA of bilayer yx was larger than that of xx on day 8, but no significant difference on day 31. The findings indicate that surface morphology dominates the wettability of these tested surfaces initially, but the material properties will take over the control of wettability as time goes by.

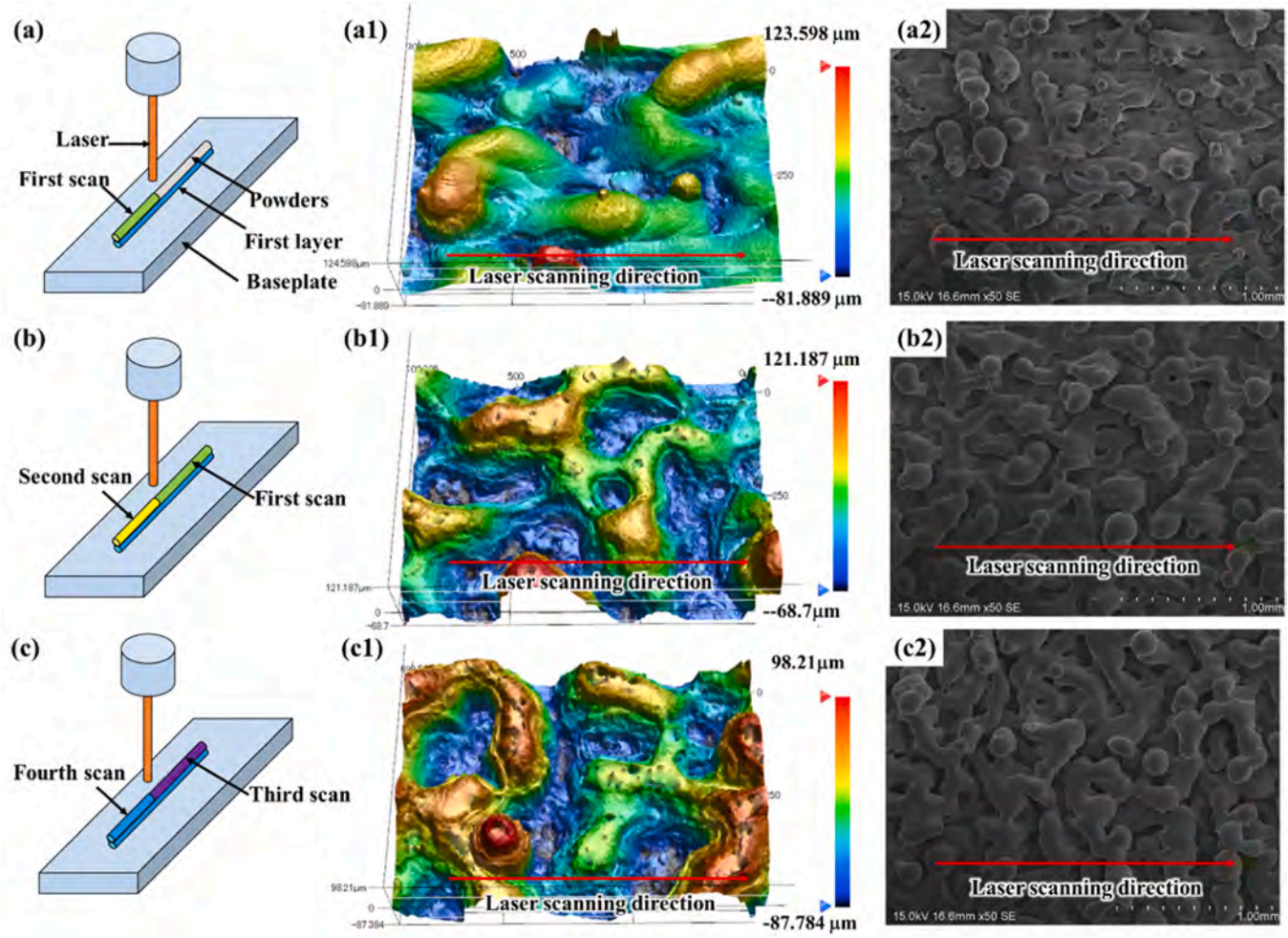

Fig. 13. LPBF-ed bilayer surfaces under different laser scans: (a)~(a2) one scan; (b)~(b2) two scans, and (c)~(c2) four scans.

3.2. Number of laser scans

Fig. 12 shows LPBF-ed surface under different number of laser scans. Both optical and SEM images illustrated significant changes in surface morphology. Lv et al. [33] verified that the in-situ re-melting could eliminate previous pores or introduce new pores by controlling laser parameters, which indicates that the re-melting is effective in rearranging pores of LPBF-ed samples. Pores of the monolayer scanned once (Fig. 12 (a1) and (a2)) were mainly concentrated on the track boundaries and obvious track-to-track boundaries could be observed. Even unmelted powders were observed on the 1-scanned surface. However, as another in-situ laser scan irradiated on the monolayer, unmelted powders were dismissed and separate metal balls were enlarged. The 2nd laser scan allowed sufficient material melting and further equilibrium between surface tension [34] and gravity. The cross-section of a single LPBF-ed track is generally close to a semicircle. Additional laser scans

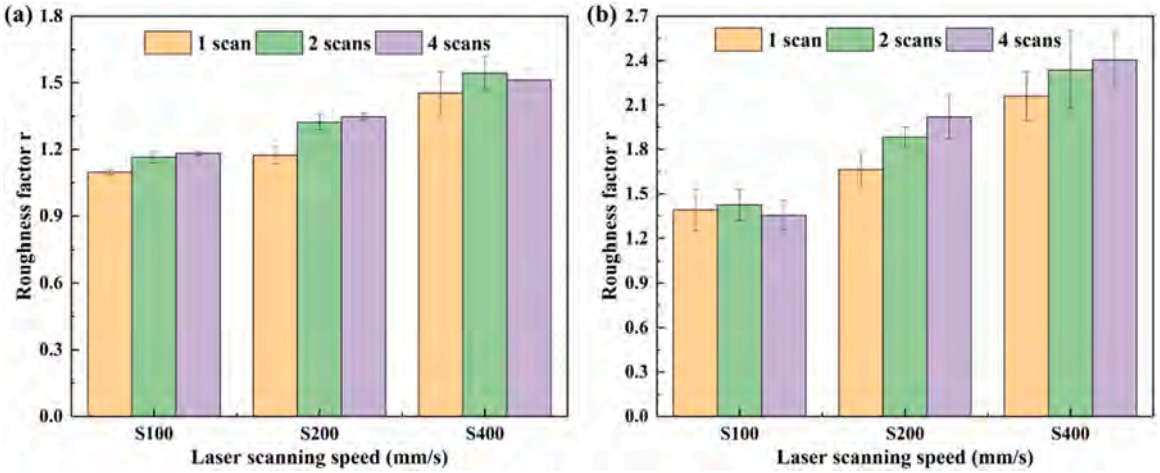

Fig. 14. Roughness factor r_{surf} of LPBF-ed: (a) monolayers and (b) bilayers under different laser scans.

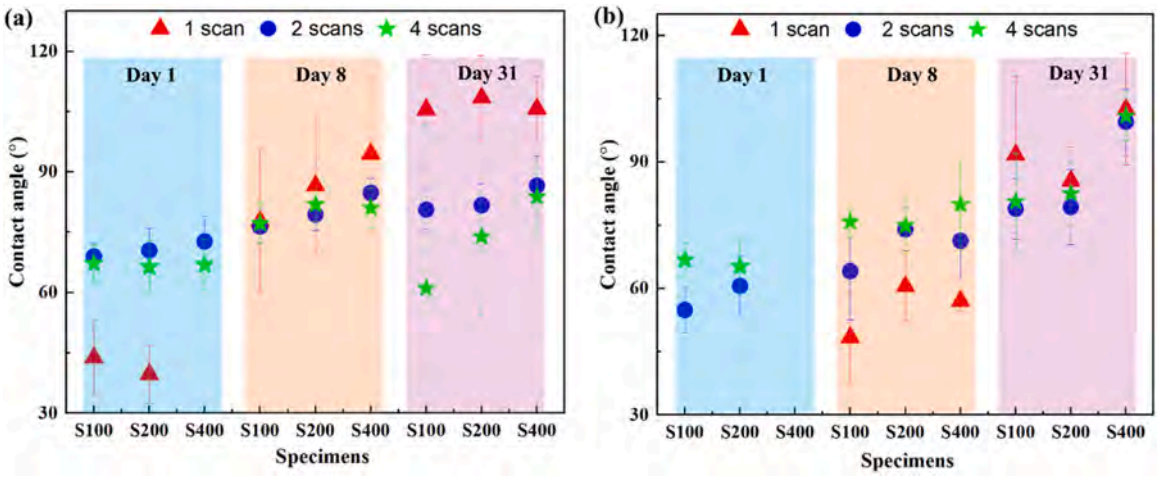

Fig. 15. Contact angle of (a) LPBF-ed monolayers and (b) LPBF-ed bilayers on day 1, day 8 and day 31.

allowed materials flow from the top of a semicircle to sides, forming the vertically extended part. Herein, materials on the 2nd scanned surface appeared to extend vertically as the remelted materials flowed to fill boundary pores, which led to a slight decrease in the height gap of Fig. 12(b1) compared with Fig. 12(a1). At the same time, part of the track boundaries remained and the remelting promoted the elimination of the traces of previous metal flow due to further action surface tension. Fig. 12 (c1) and (c2) show LPBF-ed monolayer irradiated by four laser scans. The 4th scanned surface allowed surface tension of the vertically distributed portion to fully act, resulting in the increase in the height gap in Fig. 12(c1).

Similar phenomena were observed in LPBF-ed bilayer surfaces, as shown in Fig. 13. Bilayer surfaces were with larger height differences compared to corresponding monolayer surfaces. Similar to the 1st layer, the material in the 2nd layer was reshaped by increasing the number of laser scans. However, affected by the 1st layer, the materials in the 2nd layer were molten and flowed to fill pores of both 1st and 2nd layers. As Fig. 13(b1) shown, powders were melted and sintered after the 1st laser scan, but materials condensed before adequate flow, thus the effect of pores of the 1st layer was not so obvious. As the number of laser scans increases, the molten material even could fill into the pores of the 1st layer, which will affect the morphology of the 2nd layer thereby. The bilayer surface in Fig. 13(c2) was dominated by both vertically (similar to Fig. 12(c2)) and horizontally (to fill pores in Fig. 12(c2)) connected materials. Overall, pores play a significant role in guiding the flow of the remelted materials, especially for multi-remelted materials.

To better understand the effect of multiple laser scans, the quantitative surface parameter roughness factor r_{surf} of LPBF-ed surfaces was calculated and shown in Fig. 14, where the error bars are derived from 5 measurements. r_{surf} increases as the laser scanning speed increases no matter how many time the laser is irradiated on the material. Furthermore, r_{surf} increased significantly when the number of laser scan was changed from 1 scan to 2 scans. The 2nd laser scan allowed further surface expansion of the molten material due to surface tension. But limited by the nature of the material itself, the surface expansion will stop once it was sufficiently melted. Thus, r_{surf} of some LPBF-ed samples still increased after being irradiated by 4 laser scans. However, the expanded material flowed and connected with nearby materials, driven by gravity, and some pores vanished thereby, leading to the decrease of r_{surf}. The decreased r_{surf} of monolayer surface S400 and bilayer surface S100 after 4 scans indicated that the pore vanishing dominated the change of surface roughness factor r_{surf}.

The wettability of surfaces under different laser scans was studied and summarized in Fig. 15. Fig. 15(a) shows the contact angle (CA) of monolayer surfaces. On the 1st day, CAs of 1 scan surfaces were smaller than that of 2 scans and 4 scans surfaces, which coincided well with a lower roughness factor according to Eq. (3). However, the CAs of 1 scan went up quickly as time went up, whereas that of other two groups (2 scans and 4 scans) increased slightly. Thus, on the 8th day, CAs of LPBF-ed monolayers under varying laser scans was almost the same. But on the 31st day, CAs of 1 scan become much larger than those of other two groups. Fig. 15(b) shows CAs of LPBF-ed bilayers under varying laser scans of 1 scan, 2 scans and 4 scans. Droplets on bilayer surfaces of 1 scan were absorbed quickly on the 1st day, whereas CAs of 2 scans and 4 scans were around 60° . Similarly, CAs of 1 scan surfaces increased significantly as time went up compared to the slight increase in CAs of 2 scans and 4 scans surfaces. Noted that CAs on 1st and 8th days obeyed the order of 1 scan, 2 scans and 4 scans in ascending order, partially agreed with the changes in r_{surf}. However, CAs of 1 scan went beyond others on the 31st day. In a sum, CAs of LPBF-ed surfaces were greatly affected by the surface roughness factor at the initial stage. Further, the increasing number of laser scans allowed LPBF-ed samples to reach the steady state, told by a small range of CAs as time went up.

4. Conclusion

In the study, the surface morphology of LPBF-ed mono- and bi- layers were analyzed and characterized as the surface roughness factor r_{surf}. Obviously, both the laser scanning directions and the number of laser scans affected the morphologies of these LPBF-ed layers, but their CAs did not changed a lot. However, the CAs of LPBF-ed monolayes were higher than that of bilayers. The detailed conclusions were summarized as follows:

(1) The y-scanned LPBF-ed monolayer was rougher than the x-scanned one, agrees well with the rougher particle distribution in the direction y obtained from a numerical work on the powder spreading process. The powder spreading quality affected the sintered quality of LPBF-ed layers by affecting the laser absorption.
(2) The LPBF-ed bilayer xx was rougher than yx at high laser energy but less rough at a low laser energy. More boundary pores on the 1st layer were covered by the melting of the 2nd layer, leading to a better surface of yx. However, the material of the sample S400 (corresponds to a low laser energy) cannot be continuously connected even in a single laser track and many pores appeared on the laser tracks, causing its abnormality compared to S100 and S200.
(3) The CAs of LPBF-ed mono- and bi- layers decreased as time went by, and no obvious difference between x- and y- scanned monolayers, and bilayers yx and xx. But the CAs of monolayer surfaces were larger than those of bilayer surfaces on the same day,

indicating that increasing LPBF-ed layers can promote the hydrophilicity.

(4) The number of laser scans significantly affected the morphology of LPBF samples, especially the pore distribution. Adding another laser scan allowed materials to be sufficiently melted and expand in the height due to the surface tension, resulting in a larger surface roughness factor r_{surf}. It also allowed materials connection, which was beneficial in forming a better surface. r_{surf} reflects an balance results.

(5) As time went by from day 1 to day 31, the decrease in CAs of 1 scan surfaces larger than that of 2 and 4 scans surfaces, indicating that the increasing laser scan accelerated surface stabilization, which is meaningful in biomedical application. The final CAs of LPBF-ed monolayers can be ordered as 1 scan, 2 scans, and 4 scans from large to small, but the CAs of bilayers at 4 scans were slightly larger than that of 2 scans, indicating a complicated wettability mechanism for LPBF-ed multilayers.

CRediT authorship contribution statement

Masayoshi Mizutani: Supervision, Funding acquisition. **Zhenjun Li:** Writing – review & editing, Writing – original draft, Visualization, Validation, Methodology, Investigation, Formal analysis, Data curation, Conceptualization.

Declaration of Competing Interest

The authors declare that they have no known competing financial interests or personal relationships that could have appeared to influence the work reported in this paper.

Data availability

Data will be made available on request.

Acknowledgements

This study was supported in part by JSPS KAKENHI [grant number 22H01827]; and the Machine Tool Engineering Foundation (RU-13 and RU-14).

References

[1] M. Fousová, D. Vojtěch, J. Kubásek, E. Jablonská, J. Fojt, Promising characteristics of gradient porosity Ti-6Al-4V alloy prepared by SLM process, J. Mech. Behav. Biomed. Mater. 69 (2017) 368–376, https://doi.org/10.1016/j.jmbbm.2017.01.043.

[2] M. Niinomi, M. Nakai, Titanium-based biomaterials for preventing stress shielding between implant devices and bone, Int J. Biomater. 2011 (2011), https://doi.org/10.1155/2011/836587.

[3] A. Ataee, Y. Li, C. Wen, A comparative study on the nanoindentation behavior, wear resistance and in vitro biocompatibility of SLM manufactured CP–Ti and EBM manufactured Ti64 gyroid scaffolds, Acta Biomater. 97 (2019) 587–596, https://doi.org/10.1016/j.actbio.2019.08.008.

[4] S. Arabnejad, B. Johnston, M. Tanzer, D. Pasini, Fully porous 3D printed titanium femoral stem to reduce stress-shielding following total hip arthroplasty, J. Orthop. Res. 35 (2017) 1774–1783, https://doi.org/10.1002/jor.23445.

[5] J.J.S. Dilip, S. Zhang, C. Teng, K. Zeng, C. Robinson, D. Pal, et al., Influence of processing parameters on the evolution of melt pool, porosity, and microstructures in Ti-6Al-4V alloy parts fabricated by selective laser melting, Prog. Addit. Manuf. 2 (2017) 157–167, https://doi.org/10.1007/s40964-017-0030-2.

[6] P.Y. Li, Y.E. Ma, W.B. Sun, X. Qian, W. Zhang, Z.H. Wang, Mechanical behaviors and failure modes of additive manufactured Ti6Al4V lattice structures under compressive load, Thin-Walled Struct. 180 (2022), https://doi.org/10.1016/j.tws.2022.109778.

[7] Molinari A., Klarin J., Johansson F., Benedetti M., Fontanari V., Magalini E., et al. Mechanical Properties of Porous Structures Produced by Selective Laser Melting of a Ti6Al4V Alloy Powder. vol. 65. n.d.

[8] A. Panesar, M. Abdi, D. Hickman, I. Ashcroft, Strategies for functionally graded lattice structures derived using topology optimisation for Additive Manufacturing, Addit. Manuf. 19 (2018) 81–94, https://doi.org/10.1016/j.addma.2017.11.008.

[9] A. Bandyopadhyay, F. Espana, V.K. Balla, S. Bose, Y. Ohgami, N.M. Davies, Influence of porosity on mechanical properties and in vivo response of Ti6Al4V implants, Acta Biomater. 6 (2010) 1640–1648, https://doi.org/10.1016/j.actbio.2009.11.011.

[10] J. Shi, J. Yang, Z. Li, L. Zhu, L. Li, X. Wang, Design and fabrication of graduated porous Ti-based alloy implants for biomedical applications, J. Alloy. Compd. 728 (2017) 1043–1048, https://doi.org/10.1016/j.jallcom.2017.08.190.

[11] L. Thijs, F. Verhaeghe, T. Craeghs, J.Van Humbeeck, J.P. Kruth, A study of the microstructural evolution during selective laser melting of Ti-6Al-4V, Acta Mater. 58 (2010) 3303–3312, https://doi.org/10.1016/j.actamat.2010.02.004.

[12] S. Zhang, Q. Wei, L. Cheng, S. Li, Y. Shi, Effects of scan line spacing on pore characteristics and mechanical properties of porous Ti6Al4V implants fabricated by selective laser melting, Mater. Des. 63 (2014) 185–193, https://doi.org/10.1016/j.matdes.2014.05.021.

[13] R. Stamp, P. Fox, W. O'Neill, E. Jones, C. Sutcliffe, The development of a scanning strategy for the manufacture of porous biomaterials by selective laser melting, J. Mater. Sci. Mater. Med 20 (2009) 1839–1848, https://doi.org/10.1007/s10856-009-3763-8.

[14] C. Qiu, C. Panwisawas, M. Ward, H.C. Basoalto, J.W. Brooks, M.M. Attallah, On the role of melt flow into the surface structure and porosity development during selective laser melting, Acta Mater. 96 (2015) 72–79, https://doi.org/10.1016/j.actamat.2015.06.004.

[15] D. Quéré, Wetting and roughness, Annu Rev. Mater. Res 38 (2008) 71–99, https://doi.org/10.1146/annurev.matsci.38.060407.132434.

[16] Z. Zhang, D. Liu, Y. Zhang, T. Xue, Y. Huang, G. Zhang, Fabrication and droplet impact performance of superhydrophobic Ti6Al4V surface by laser induced plasma micro-machining, Appl. Surf. Sci. 605 (2022), https://doi.org/10.1016/j.apsusc.2022.154661.

[17] J.W. Song, L.W. Fan, Understanding the effects of surface roughness on the temperature and pressure relevancy of water contact angles, Colloids Surf. A Physicochem Eng. Asp. 656 (2023), https://doi.org/10.1016/j.colsurfa.2022.130391.

[18] Z. Xu, Y. Zhang, Q. He, Study on anisotropic contact angle of rectangular convex structure on fluorine rubber surface, Colloids Surf. A Physicochem Eng. Asp. 655 (2022), https://doi.org/10.1016/j.colsurfa.2022.130047.

[19] S. Liu, G. Xiao, O. Lin, Y. He, S. Song, A new one-step approach for the fabrication of microgrooves on Inconel 718 surface with microporous structure and nanoparticles having ultrahigh adhesion and anisotropic wettability: Laser belt processing, Appl. Surf. Sci. 607 (2023), https://doi.org/10.1016/j.apsusc.2022.155108.

[20] C.M. Cotrut, I.C. Ionescu, E. Ungureanu, A. Berbecaru, R.I. Zamfir, A. Vladescu, et al., Evaluation of surface modification techniques on the ability of apatite formation and corrosion behavior in synthetic body fluid: An in vitro study, Surf. Interfaces 22 (2021), https://doi.org/10.1016/j.surfin.2020.100866.

[21] H.H. Huang, C.F. Liu, S. Wang, C.S. Chen, J.H. Chang, Nitrogen plasma immersion ion implantation treatment of Ti6Al7Nb alloy for bone-implant applications: Enhanced in vitro biological responses and in vivo initial bone-implant contact, Surf. Coat. Technol. 405 (2021), https://doi.org/10.1016/j.surfcoat.2020.126551.

[22] J. Stef, A. Poulon-Quintin, A. Redjaimia, J. Ghanbaja, O. Ferry, M. De Sousa, et al., Mechanism of porosity formation and influence on mechanical properties in selective laser melting of Ti-6Al-4V parts, Mater. Des. 156 (2018) 480–493, https://doi.org/10.1016/j.matdes.2018.06.049.

[23] J. Karimi, M. Antonov, L. Kollo, K.G. Prashanth, Role of laser remelting and heat treatment in mechanical and tribological properties of selective laser melted Ti6Al4V alloy, J. Alloy. Compd. 897 (2022), https://doi.org/10.1016/j.jallcom.2021.163207.

[24] B. Liu, B.Q. Li, Z. Li, Selective laser remelting of an additive layer manufacturing process on AlSi10Mg, Results Phys. 12 (2019) 982–988, https://doi.org/10.1016/j.rinp.2018.12.018.

[25] J. Vaithilingam, R.D. Goodridge, R.J.M. Hague, S.D.R. Christie, S. Edmondson, The effect of laser remelting on the surface chemistry of Ti6al4V components fabricated by selective laser melting, J. Mater. Process Technol. 232 (2016) 1–8, https://doi.org/10.1016/j.jmatprotec.2016.01.022.

[26] Z. Li, M. Mizutani, Influence of layer thickness and substrate bed on the void fraction of powder layers for laser powder bed fusion, Powder Technol. 418 (2023), https://doi.org/10.1016/j.powtec.2023.118293.

[27] T. Murono, K. Hongo, K. Nakano, R. Maezono, Ab-initio-based interface modeling and statistical analysis for estimate of the water contact angle on a metallic Cu (111) surface, Surf. Interfaces 34 (2022), https://doi.org/10.1016/j.surfin.2022.102342.

[28] A. Mussatto, R. Groarke, A. O'Neill, M.A. Obeidi, Y. Delaure, D. Brabazon, Influences of powder morphology and spreading parameters on the powder bed topography uniformity in powder bed fusion metal additive manufacturing, Addit. Manuf. 38 (2021) 101807, https://doi.org/10.1016/j.addma.2020.101807.

[29] A. Phua, P.S. Cook, C.H.J. Davies, G.W. Delaney, Powder spreading over realistic laser melted surfaces in metal additive manufacturing, Addit. Manuf. Lett. 3 (2022) 100039, https://doi.org/10.1016/j.addlet.2022.100039.

[30] Z. Xiang, M. Zhang, R. Yan, Q. Yin, K. Zhang, Powder-spreading dynamics and packing quality improvement for laser powder bed fusion additive manufacturing, Powder Technol. 389 (2021) 278–291, https://doi.org/10.1016/j.powtec.2021.05.036.

[31] S. Ishibashi, K. Shimada, H. Kanetaka, M. Tsukuda, T. Mizoi, M. Chuzenji, et al., Porosity and tensile properties of rhizoid porous structure fabricated using selective laser melting, Int. J. Autom. Technol. 14 (2020) 582–591, https://doi.org/10.20965/ijat.2020.p0582.

[32] Dal M., Mayi Y., Marchais K., Peyre P. Powder Consideration For Additive Manufacturing Simulation n.d.
[33] F. Lv, H. Liang, D. Xie, Y. Mao, C. Wang, L. Shen, et al., On the role of laser in situ re-melting into pore elimination of Ti–6Al–4V components fabricated by selective laser melting, J. Alloy. Compd. 854 (2021) 156866, https://doi.org/10.1016/j.jallcom.2020.156866.
[34] Morville S., Carin M., Muller M., Gharbi M., Peyre P., Carron D., et al. 2D axial-symmetric model for fluid flow and heat transfer in the melting and resolidification of a vertical cylinder. n.d.

Blanked Surface Characteristics of Amorphous Alloys with Local Microstructure Modification by Ultrashort Pulsed Laser

Chieko Kuji[1,a] [0000-0002-3377-178X]

[1] Tohoku University, Sendai 980-8579, Japan
[a]c-kuji@tohoku.ac.jp

Abstract. Amorphous alloys with no crystal structure, particularly Fe-based ones, exhibit excellent soft magnetic properties and are expected to be applied to motor cores because of their high magnetic flux density. However, they are difficult to machine because of their mechanical properties, such as high strength and toughness, owing to their unique structure. These mechanical properties of amorphous alloys change due to thermal microstructural changes, that is, structural relaxation and crystallization; however, the excellent magnetic properties also degrade. Therefore, this study proposes a new blanking method that improves the machinability of amorphous alloys without degrading their magnetic properties by thermally changing the microstructure of the local area where blanking is performed. This study investigated the effectiveness of ultrashort pulsed lasers, which have little thermal effect, on the local heat treatment of amorphous alloys. Furthermore, blanking tests were performed on the locally heat-treated amorphous alloys, and the blanking resistance values and characteristics of the blanked surfaces were evaluated.

Keywords: Amorphous alloy, Ultrashort pulsed laser, Local heat treatment, Blanking, Surface characteristic

1 Introduction

Amorphous alloys exhibit a unique structure without crystals, which is achieved by rapid quenching from the molten state to suppress the formation of a long-range ordered structure [1]. In particular, Fe-based amorphous alloys exhibit excellent material properties, such as high soft magnetic properties, strength, and toughness. Because of their high magnetic flux density and low iron loss, they are expected to be applied in motor cores with high energy-saving effects [2]. However, their tough mechanical properties render them difficult to machine. All of these material properties are caused by the amorphous structure.

Therefore, this study develops a new blanking method that locally transforms the amorphous microstructure, which is the cause of various material properties, and improves only the machinability [3-5]. Because amorphous alloys are metastable, they transform their structure through structural relaxation [6] and crystallization [7], in which atoms are shifted to stable positions by heat. In this study, the microstructure was gradually changed by adjusting the heat treatment temperature [3], and the mechanical properties in a few-micrometer region drastically changed depending on the microstructure [4]. Furthermore, by using ultrashort pulsed lasers, which have a low thermal effect, for heat treatment applications, it was possible to thermally transform only the machining area while suppressing thermal diffusion, and the machining resistance was successfully reduced [5].

In this paper, the effect of microstructure on blanked surface characteristics is discussed by comparing the blanked cross sections of samples heat-treated with ultrashort pulsed lasers and conventional methods.

2 Methods

Iron-based amorphous alloy foil strip $Fe_{77}B_{16}Cr_2Si_5$ (Metglas 2605S-3A, PROTERIAL, Ltd.) with approximately 20-μm thickness, whose microstructure changes due to heat treatment had been investigated in the past [3], was used for the evaluation. As the microstructure of amorphous alloys changes drastically with a difference of only a few degrees in the heating temperature [3], normal heat treatment was performed using a thermogravimetric differential thermal analyzer (TG-DTA: TG8120, Rigaku Corp.), which enables precise temperature control. Heat treatment was performed in a reducing atmosphere (0.998% H_2-Ar gas) to prevent oxidation. The samples were heated from 300 K at 20 K/min to 713 K and 873 K for structural relaxation and full crystallization, respectively. Subsequently, it was cooled to 300 K at 20 K/min without holding the samples isothermally at the highest temperature. An ultrashort pulsed laser (LPF-2, Lastec Co., Ltd.) with a laser beam diameter ($1/e^2$ width) of 65.6 μm was used for local heating. The laser irradiation conditions were an oscillation central wavelength of 1,030 nm, power of 1 W, pulse width of 260 fs, and pulse repetition frequencies of 50 kHz and 200 kHz. Laser irradiation at 50 kHz causes structural relaxation, whereas irradiation at 200 kHz causes crystallization [5]. The laser was irradiated at equal intervals with a 0.1-mm spacing after 20,000 laser pulses per spot,

and local heat treatment was performed in a dotted pattern along the contour of the tool geometry (see Fig. 1(a)). Moreover, four pinholes were created to fix the sample to the blanking machine. The as-received, normally heated, and locally heated samples were blanked under the same conditions. The machine shown in Fig. 1 (b) was used for the blanking test. The clearance between the punch and die was set to 2 μm. A rectangular punch with a 4-mm width and 12-mm length was used. To accurately blank out the heated position of the locally heated specimen, the punch was fixed to four pins installed on the blanking machine. The blanking speed was set to 20 mm/s, and the blanked fracture surface was observed using a scanning microscope (SEM, JXA-8530F, JEOL).

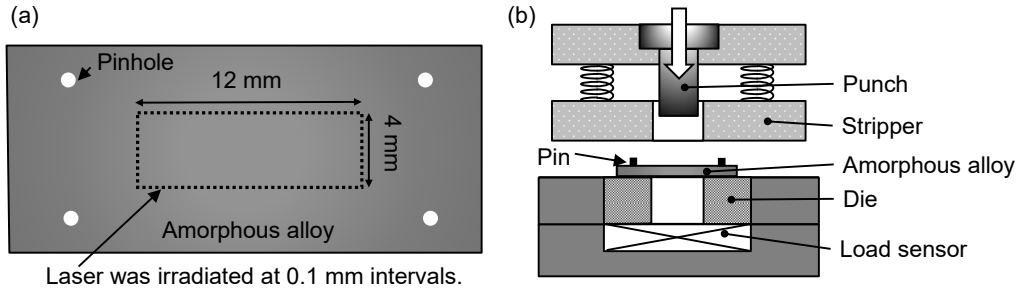

Fig. 1. Schematic diagram of (a) the laser irradiated specimen and (b) the blanking machine.

3 Results and Discussion

Fig. 2 shows the SEM images of the blanked fracture surfaces of the as-received and normally heat-treated samples. Figs. 2(a), 2(b), and 2(c) refer to the as-received sample, structurally relaxed sample heated to 713 K, and (c) fully crystallized sample heated to 873 K. In all the cases, the tool was fed from the top to the bottom of the image. Generally, the blanking surface of a metallic material consists of four elements: (i) a shear droop caused by material deformation, (ii) a sheared face created by friction between the tool and material, (iii) a broken face created by crack growth, and (iv) a burr, which is a machining defect at the bottom of the material. The as-received specimen in Fig. 2(a) has high toughness, and faces (i) and (ii) were generated by shear slip and tool friction. In Fig. 2(b), (iii) appeared all over the surface due to embrittlement, and in Fig. 2(c), (iv) was caused by the recovery of the plastic deformation ability due to crystallization. In the unobserved area, large cracks and wavy surfaces were observed in all cases, and it is difficult to conclude that the surfaces were well-machined.

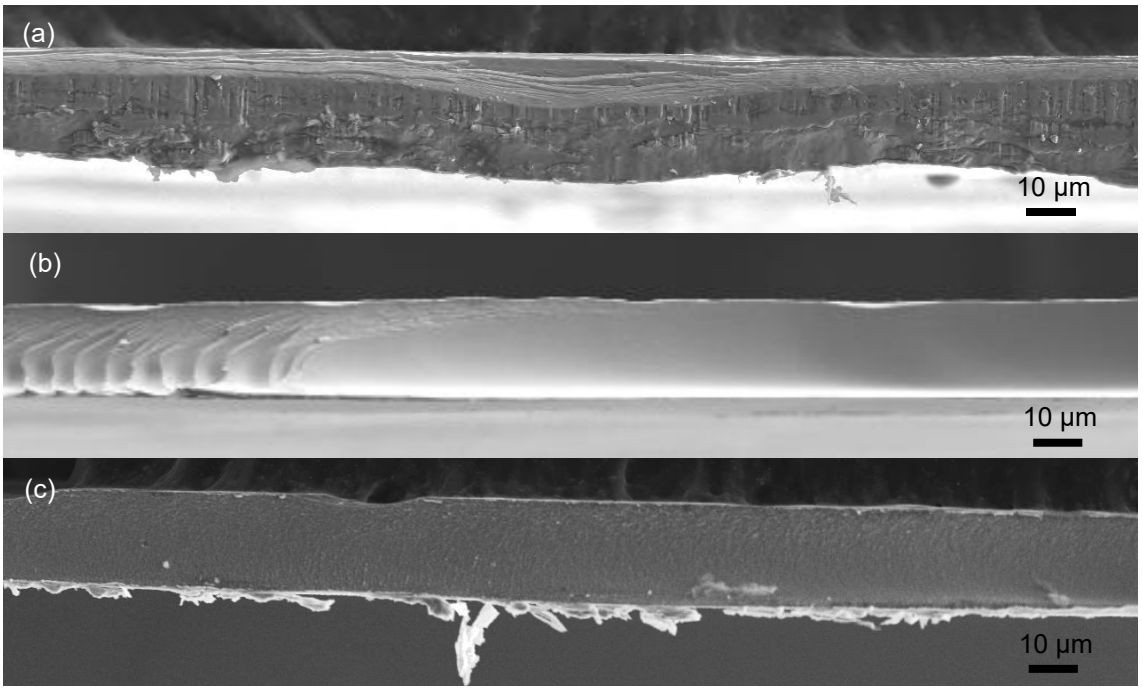

Fig. 2. Blanked surface characteristics of (a) the as-received specimen, (b) the specimen annealed up to 713 K, and (c) the specimen annealed up to 873 K, as observed by SEM.

Fig. 3 shows the SEM images of the blanked surfaces of the samples locally heated by an ultrashort

pulsed laser. Fig. 3(a) shows a sample of structural relaxation when the pulse repetition frequency is 50 kHz, and Fig. 3(b) shows a crystallized sample when the pulse repetition frequency is 200 kHz. In both cases, the laser irradiation initially causes ablation, followed by local heating due to latent heat, resulting in a hole-like cut line at the laser-irradiated point (arrow mark in Fig. 3). Fig. 3 shows that (ii) and (iii) appear above and below the fracture surface, respectively, regardless of the microstructure. Furthermore, neither (i) nor (iv), which can lead to machining defects, were observed. Even in the unshown region, an ideal machined surface without cracks or waviness was obtained. As shown in Fig. 2, the specimens with normal heating exhibited significant changes in mechanical properties [4] and fracture surface shape [8], depending on the microstructure of the specimens. This is attributed to the original undulation of the specimen, which preferentially deforms the convex part of the specimen, resulting in an unevenly blanked surface. In contrast, when ultrashort pulsed laser local heating was used, the small holes formed during the heat treatment caused a notch effect, and deformation proceeded from the stress concentration points, resulting in almost the same fracture surface shape, regardless of the microstructure.

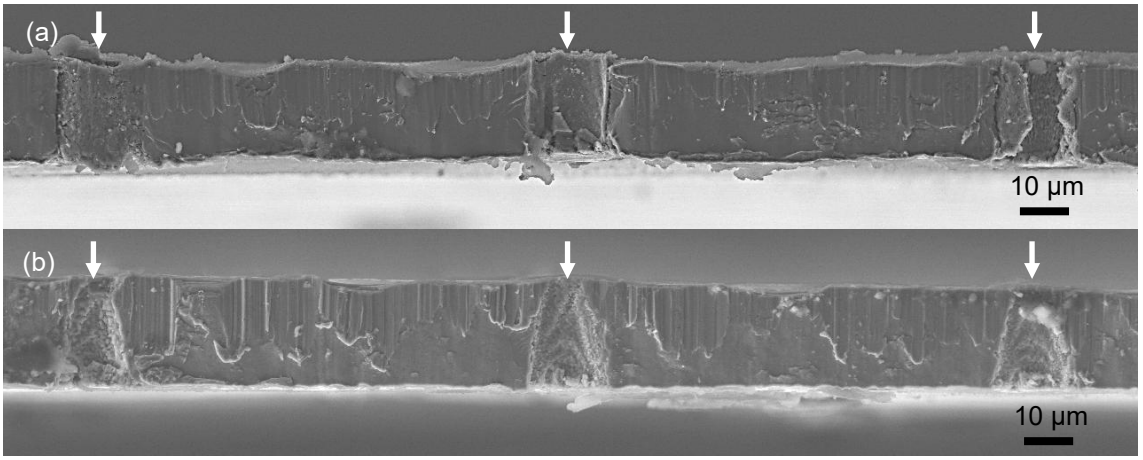

Fig. 3. Blanked surface characteristics of the locally heated specimen when the pulse repetition frequencies are (a) 50 kHz and (b) 200 kHz. Each surface was observed by SEM.

4 Conclusions

In this study, the blanked surface characteristics of Fe-based amorphous alloys subjected to different heat treatment methods were evaluated using SEM images. For the normal heat treatment method, the blanked surface characteristics significantly changed depending on the change in the microstructure, resulting in the appearance of an uneven blanked surface. However, for local heating using an ultrashort pulsed laser, the notch effect caused by the small holes formed during the heat treatment resulted in the appearance of a uniform and ideal blanked surface, even for specimens with different microstructures.

References

1. Chen, H. S., Miller, C. E.: A Rapid Quenching Technique for the Preparation of Thin Uniform Films of Amorphous Solids. Review of Scientific Instruments 41, 1237–1238 (1970).
2. Enomoto, Y.: Radial Gap Type Motor using Amorphous Metal for Iron Core. IEEJ Transactions on Industry Applications 139(6), 606–611 (2019).
3. Kuji, C., Takenaka, K., Mizutani, M., Shimada, K., Kuriyagawa, T., Konno, T. J.: Crystallization Behavior and Machining Properties of Annealed Fe–Si–B–Cr Amorphous Alloys. Journal of Materials Science 56(29), 16697–16711 (2021).
4. Kuji, C., Mizutani, M., Shimada, K., Suzuki, K., Miura, H., Kuriyagawa, T.: Evaluation of Fracture Properties of Annealed Fe–Si–B–Cr Amorphous Alloys using Micro-Tensile Tests and Blanking Machinability. Materials Science and Engineering: A 848, 143483 (2022).
5. Kuji, C., Mizutani, M., Takenaka, K., Shimada, K., Konno, T. J., Soyama, H., Kuriyagawa, T.: Effect of Local Heating by Ultrashort Pulsed Laser on Fe–Si–B–Cr Amorphous Alloys and Its Influence on Blanking Machinability. Precision Engineering 81, 135–144 (2023).
6. Antonione, C., Baricco, M., Riontino, G.: Structural Relaxation Kinetics in FeSiB Amorphous-Alloys. Journal of Materials Science 23(6), 2225–2229 (1988).
7. Zaluska, A., Matyja, H.: Crystallization Characteristics of Amorphous Fe-Si-B Alloys. Journal of Materials Science 18(7), 2163–2172 (1983).
8. Kuji, C., Mizutani, M., Takenaka, K., Shimada, K., Konno, T. J., Yokobori, A. T., Kuriyagawa, T.: Relationship between Blanking Performance and Microstructure of Annealed Fe–Si–B–Cr Amorphous Alloy Sheets. Precision Engineering 82, 33–43 (2023).

Acknowledgements

The author would like to express her deepest gratitude to Professor Emeritus Tsunemoto Kuriyagawa and his colleagues at Tohoku University, Japan for their invaluable guidance in the conduct of this research. Special thanks to the Materials Processing Technology Department of the Iwate Industrial Research Institute, Japan for the use of their scanning electron microscope.

Part of this work was supported by JSPS KAKENHI, grant number 23K13228, and The Amada Foundation, AF-2022238-C2.

Fluid/Material Coupled Numerical Simulation of a Bubble Collapse near a Wall for Laser Cavitation Peening

Yuka Iga[1,a] [0000-0003-2364-2869], Chieko Kuji[2,b][0000-0002-3377-178X], Hirotoshi Sasaki[3,c][0000-0002-5211-0979] and Hitoshi Soyama[2,d][0000-0003-4512-6718]

[1] Institute of Fluid Dynamics Tohoku University, 2-2-1 Katahira, Sendai, 980-8577, Japan
[2] Department of Finemechanics, Tohoku University, 6-6-01 Aoba-ku, Sendai, 980-8579, Japan
[3]Tokai Head Office, The Japan Atomic Power Company, 1-1 Shirakata, Tokai, 319-1198, Japan
[a]yuka.iga.b4@tohoku.ac.jp, [b]c-kuji@tohoku.ac.jp, [c]imp5.sti.ra@gmail.com,
[d]soyama@mm.mech.tohoku.ac.jp

Abstract. An impact of a bubble induced by a submerged pulsed laser is utilized for improvement of fatigue strength of metallic materials. As the bubble induced by the pulsed laser behaves like a cavitation bubble, the laser induced bubble is called as “laser cavitation”. The mechanical surface treatment using the laser cavitation impact is named as “laser cavitation peening”. At laser cavitation peening, the impact induced by laser cavitation collapse strongly depends on the bubble geometry. There are two typical mode at the bubble collapse. One mode is “microjet mode”, at which bubble develops near the target and is collapsed with generating a microjet in the bubble. The other mode is “hemispherical mode”, at which a hemispherical bubble develops on the target surface and is collapsed on the surface. As the bubble collapse of microjet mode is interesting phenomenon, a lot of researchers investigate “microjet mode”. However, impact induced by “hemispherical mode” is significantly larger than that of “microjet mode”. In the present paper, to optimize laser cavitation peening condition, a fluid/material coupled numerical simulation of a bubble collapse near a wall was carried out changing with standoff distance from wall. It was revealed that the equivalent stress induced by hemispherical mode was larger than that of microjet mode.

Keywords: Cavitation, Bubble, Numerical Simulation, Laser, Peening

1 Introduction

In the case of laser peening, which is also called as laser shock peening, there are two types. One is laser peening with water film [1]. The other is laser peening under water, i.e., submerged laser peening [2]. For both laser peening, it has been thought that peening mechanism to introduce local plastic deformation is caused by laser ablation [3]. Namely, it is thought that inertial force caused by shock wave at laser ablation is contained by water, and it produces plastic deformation into metallic materials [1, 3]. However, in the case of submerged laser peening, a bubble which behaves like a cavitation bubble is generated after the laser ablation, and the bubble impact can be utilized for peening [4] (see Fig. 1 (a)). In the present paper, the bubble is called as “laser cavitation”, and a peening method using laser cavitation impact is named as “laser cavitation peening” [5-7].

When pressure wave in water was measured by a submerged shock wave sensor, the amplitude of laser ablation was larger than that of laser cavitation collapse as shown in Fig. 1 (b) [4] . However, an impact induced of laser cavitation collapse measured by a PVDF sensor in target was larger than that of laser ablation (see Fig. 1 (c)) [4]. Namely, the laser cavitation impact is useful for the laser cavitation peening.

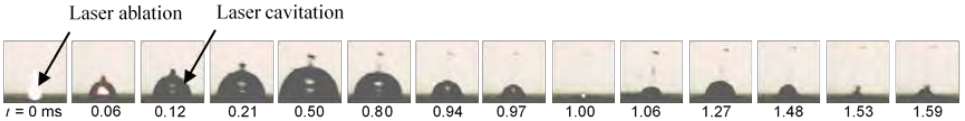

(a) Aspect of laser ablation and laser cavitation

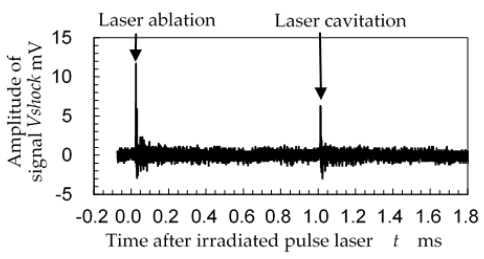

(b) Signal from a shockwave sensor in water

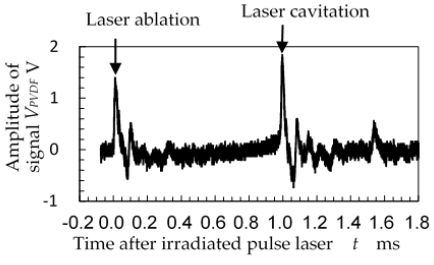

(c) Signal from a PVDF sensor in the target

Fig. 1. Calculation area and initial condition of calculation [4].

As the improvements of fatigue properties of metallic materials such as additive manufactured titanium alloy Ti6Al4V [8] and magnesium alloy AZ31 [9] by laser cavitation peening were reported, it is worthwhile to optimized and enhance peening intensity of laser cavitation peening.

In the case of research area on cavitation, i.e., bubble dynamics, a bubble collapse with a microjet, i.e., "microjet mode", was an attractive phenomenon in both experimental and numerical analysis since early 1970s [10, 11]. When peening effects such as introduction of compressive residual stress was compared experimentally, hemispherical bubble collapse, i.e., "hemispherical mode" was more aggressive comparing with "microjet mode" [7]. Iga and Sasaki demonstrated numerically by a fluid/material coupled numerical simulation that effects of bubble collapse into material surface strongly depended on the bubble shape.

In the present paper, in order to optimize laser cavitation peening, the difference between "microjet mode" and "hemispherical mode" was investigated numerically by the fluid/material coupled numerical simulation.

2 Numerical Method

In the preset paper, in house code of fluid/material coupled numerical simulation was used. The details were described in the previous papers [12, 13]. Figure 2 shows the calculation area and initial condition of calculation. Duralumin was simulated as target material. In order to investigate the collapsing mode of the bubble, γ is defined by the distance between the center of the bubble and the wall surface, L, and the maximum bubble radius R_{max} as Eq. (1).

$$\gamma = \frac{L}{R_{max}} \tag{1}$$

Here, $\gamma = 0$ and $\gamma = 1.2$ correspond to "hemispherical mode" and "microjet mode", respectively [13].

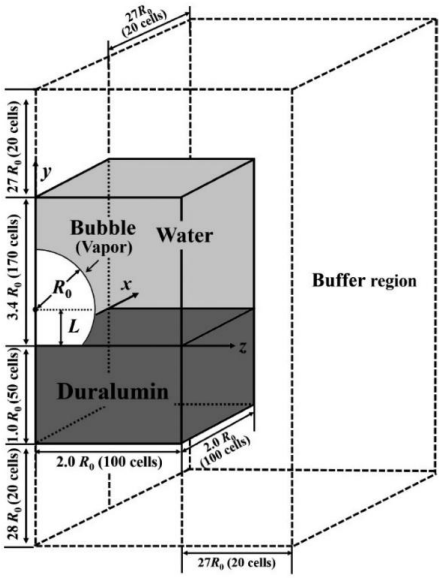

Fig. 2. Calculation area and initial condition of calculation.

3 Results

Figure 3 reveals the color contour at bubble collapse (a) hemispherical mode and (b) microjet mode. As bubble shape, pressure in water and stress in material were changing with time, the time of maximum pressure in water at each mode was chosen for Fig. 3, respectively. In Fig. 3, black lines show the bubble shape changing with time from $R = R_{max}$ to the collapse. The color contour of upper left of each figure reveals void fraction. The void fraction is almost zero at the moment in Fig. 3 because the moment of maximum pressure is final stage of the bubble collapse, although the bubble will rebound after this moment. The upper right illustrates pressure and velocity vectors in the fluid domain. The equivalent stress in the material domain was shown in lower part.

Figure 4 shows the maximum equivalent stress in material domain $(\sigma_{eq})_{max}$ during the collapse. In the case of microjet mode, the pressure in water reached about 450 MPa due to water hummer pressure of the microjet, however, $(\sigma_{eq})_{max}$ was less than 100 MPa. On the other hand, $(\sigma_{eq})_{max}$ of hemispherical mode

reached over 2.5 GPa. And also, the volume of stress influential area and the depth of stress influential area of hemispherical mode were larger than those of microjet mode [13]. These results well correspond to the experimental result, in which the introduced compressive residual stress by hemispherical mode was larger and deeper than that of microjet mode [7].

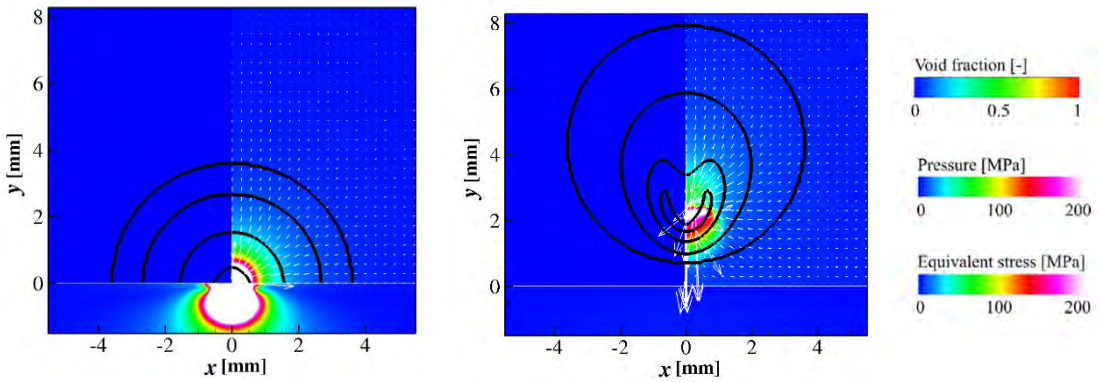

(a) Hemispherical bubble on the wall (hemispherical mode)

(b) Spherical bubble near the wall (microjet mode);

Fig. 3. Fluid/material coupled numerical simulation of collapse of a bubble near a wall

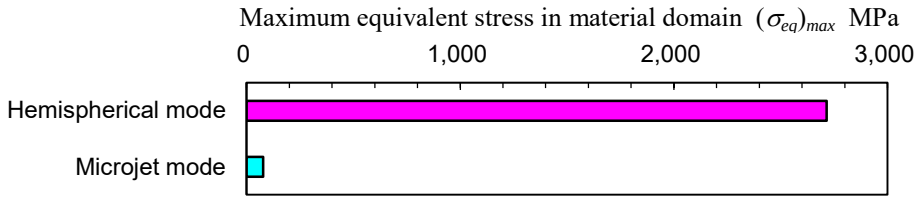

Fig. 4. Difference between hemispherical mode and microjet mode on maximum equivalent stress in material domain

4 Conclusions

In order to demonstrate the difference on peening intensity of laser cavitation peening between microjet mode and hemispherical mode, fluid/material coupled numerical simulation was carried out. It was concluded that maximum equivalent stress induced by hemispherical mode was larger than that of microjet mode.

Acknowledgements

This research was partly supported by JSPS KAKENHI grant numbers 22KK0050 and 23H01292.

References

1. Peyre, P., Fabbro, R., Merrien, P., et al.: Laser shock processing of aluminium alloys. Application to high cycle fatigue behaviour. Mater Sci Eng A 210, 102-113 (1996).
2. Sano, Y., Obata, M., Kubo, T., et al.: Retardation of crack initiation and growth in austenitic stainless steels by laser peening without protective coating. Mater Sci Eng A 417, 334-340 (2006).
3. Sano, Y., Akita, K., Sano, T.: A mechanism for inducing compressive residual stresses on a surface by laser peening without coating. Metals 10, 816 (2020).
4. Soyama, H.: Comparison between the improvements made to the fatigue strength of stainless steel by cavitation peening, water jet peening, shot peening and laser peening. J Mater Process Technol 269, 65-78 (2019).
5. Soyama, H.: Laser cavitation peening and its application for improving the fatigue strength of welded parts. Metals 11, 531 (2021).
6. Soyama, H., Korsunsky, A.M.: A critical comparative review of cavitation peening and other surface peening methods. J Mater Process Technol 305, 117586 (2022).
7. Soyama, H., Iga, Y.: Laser cavitation peening: A review. Preprint (wwwpreprintsorg) (2023).
8. Soyama, H., Kuji, C.: Improving effects of cavitation peening, using a pulsed laser or a cavitating jet, and shot peening on the fatigue properties of additively manufactured titanium alloy Ti6Al4V. Surface Coatings Technol 451, 129047 (2022).
9. Soyama, H., Kuji, C., Liao, Y.L.: Comparison of the effects of submerged laser peening, cavitation peening and shot peening on the improvement of the fatigue strength of magnesium alloy AZ31. J Magnesium and Alloys 11, in press (2023).
10. Plesset, M.S., Chapman, R.B.: Collapse of an initially spherical vapour cavity in neighbourhood of a solid boundary. J Fluid Mech 47, 283-290 (1971).
11. Lauterborn, W., Bolle, H.: Experimental investigations of cavitation-bubble collapse in neighborhood of a solid boundary. J Fluid Mech 72, 391-399 (1975).
12. Ochiai, N., Iga, Y., Nohmi, M., et al.: Numerical analysis of nonspherical bubble collapse behavior and induced

impulsive pressure during first and second collapses near the wall boundary. J Fluid Sci Technol 6, 860-874 (2011).
13. Iga, Y., Sasaki, H.: Relationship between a non-spherical collapse of a bubble and a stress state inside a wall. Phys Fluids 35, 023312 (2023).

Materials Today Communications 40 (2024) 109564

Contents lists available at ScienceDirect

Materials Today Communications

journal homepage: www.elsevier.com/locate/mtcomm

Acid resistance of hydroxyapatite dental films fabricated through powder jet deposition

Chieko Kuji [a,*], Kuniyuki Izumita [b], Keita Shimada [c], Masayoshi Mizutani [d], Keiichi Sasaki [e], Tsunemoto Kuriyagawa [f]

[a] Department of Mechanical Systems Engineering, Graduate School of Engineering, Tohoku University, Sendai 980-8579, Japan
[b] Perioperative Oral Health Management, Tohoku University Hospital, Sendai 980-8574, Japan
[c] Graduate School of Engineering, Nihon University, Koriyama 963-8642, Japan
[d] Research Center for Green X-Tech, Green Goals Initiative, Tohoku University, Sendai 980-8577, Japan
[e] Division of Advanced Prosthetic Dentistry, Graduate School of Dentistry, Tohoku University, Sendai 980-8575, Japan
[f] Center for Co-Creation Strategy, Tohoku University, Sendai 980-8577, Japan

ARTICLE INFO

Keywords:
Powder jet deposition
Dental treatment method
Hydroxyapatite
Acid resistance
Transmission electron microscope
Smoothed particle hydrodynamics

ABSTRACT

This study proposes a novel dental treatment method using powder jet deposition (PJD). PJD can be employed to fabricate hydroxyapatite (HA) films directly on human enamel by blasting fine HA particles. Acid resistance tests were performed on HA films fabricated with two blast angles ($\alpha = 60^\circ$ and 90° with two samples each) and using human enamel (with one sample) to evaluate the usefulness of the HA films in acidic intraoral environments. All samples were dissolved in acid, and their volume gradually decreased over the test time t_{acid}. Transmission electron microscopy images showed that the grain boundaries near the acid-exposed surface of the HA films were densely modified and prevented acid penetration, whereas the human enamel grains became finer owing to the acid–base reaction. Thus, the HA films lost lesser volume than the human enamel did, indicating higher acid resistance. However, one film fabricated at $\alpha = 60^\circ$ partially peeled off during $t_{acid} = 6$–9 h. Analysis of the PJD phenomenon through smoothed particle hydrodynamics indicated that the tensile residual stresses promoting crack propagation and delamination increased as α became more acute, causing HA film peeling. Therefore, particles should be blasted in multiple directions to avoid stress bias.

1. Introduction

Human teeth have hard enamel comprising small columnar structures that protect dentin composed of tubules [1]. Current widespread caries treatment practices involve removing the caries penetrating the dentin and filling the cavity with dental material [2]. However, extreme temperature and pH conditions of the intraoral environment pose challenges. Therefore, differences in material properties between dental materials and human teeth cause deformation of the dental materials, resulting in the recurrence of caries from the interface between the dental material and cavity, known as secondary caries [3]. This necessitates the use of new dental materials with mechanical properties similar to those of human teeth and new treatment methods for tightly bonding the dental materials to human teeth.

To meet these requirements, this study proposes an innovative dental treatment method using powder jet machining (PJM) (Fig. 1). PJM is a blasting method using metal or ceramic particles, as well as other materials. When particles impact a workpiece at a high velocity, either the workpiece is removed (referred to as abrasive jet machining (AJM)) [4], or the impacted particles are deposited on the workpiece (referred to as powder jet deposition (PJD)) [5]. AJM and PJD can be performed under atmospheric pressure at normal temperatures and transition depending on processing conditions, such as the size d_p, impact velocity v, and impact angle θ of the blasting particles [6]. General deposition processes, such as thermal spraying [7], cold spraying [8], and aerosol deposition [9], have environmental restrictions, e.g., they can be conducted only under a high temperature or vacuum, making the restriction-free PJD a unique method. PJM can be directly applied to the intraoral environment; caries can be removed through AJM and an artificial dental film can be created through PJD. In particular, artificial dental films prepared through PJD have high versatility and can be applied in preventive and cosmetic dentistry.

* Corresponding author.
E-mail address: c-kuji@tohoku.ac.jp (C. Kuji).

https://doi.org/10.1016/j.mtcomm.2024.109564
Received 3 April 2024; Received in revised form 1 June 2024; Accepted 12 June 2024
Available online 13 June 2024

To evaluate the usefulness of the proposed method, hydroxyapatite (HA): calcium phosphate ($Ca_{10}(PO_4)(OH)_2$), a highly biocompatible bioceramic material accounting for 97 % of human enamel and 70 % of dentin [10,11], was used as the blasting particle material, and a fundamental investigation was conducted. HA films were formed on human enamel through PJD. The Vickers hardness of the films was equivalent to that of human enamel, whereas their bonding strength to human enamel was comparable to that of a dental composite resin bonded with bonding agents [12]. Molecular dynamics showed that atomic-level bonds were formed between human enamel and the HA films owing to the instantaneous high-temperature and high-pressure environment at the impact interface caused by PJD [13]. Thermal cycling tests simulating intraoral temperatures were performed, and no changes in the Vickers hardness or adhesion strength were observed before and after the tests, demonstrating high adaptability to harsh intraoral environments [14]. However, the effects of the oral pH have not been investigated. Although the average intraoral pH is 7.4, the oral environment is prone to pH changes; acidic foods and beverages, drugs, and gastric reflux significantly reduce the pH [15]. When dental plaque is deposited on the tooth surface, the pH in the area beneath the dental plaque drops to less than 5.5 immediately after consuming a sugary food. Human enamel and dentin are demineralized when the intraoral pH drops to 5.5–5.7, causing dental caries [16]. Therefore, the acid resistance of PJD-fabricated HA films in an intraoral acidic environment must be evaluated to determine the practical usability of the films.

This study evaluated the usefulness of HA films fabricated through PJD in an intraoral acidic environment and tested the acid resistances of the films as well as human enamel. HA films are typically prepared by blasting perpendicular to the flat workpiece. However, the actual tooth surface is uneven [17] and may be blasted in an oblique direction to the affected area. Therefore, this study fabricated HA films at two different blasting angles α and investigated the effect of α on the acid resistance of the HA films. The microstructures of the HA films and human enamel were observed using scanning electron microscopy (SEM) and transmission electron microscopy (TEM), and the physical phenomena during PJD were analyzed using the smoothed particle hydrodynamics (SPH) method.

2. Materials and methods

2.1. Materials

HA was used as the particle and workpiece material for PJD. The HA particles were synthesized by a hydrothermal synthesis method, and the HA substrate was obtained as a commercial product (Kurisera, Kyushu Refractories CO., LTD.) commonly used in dental research. Fig. 2(a) shows the HA particle size distribution measured using a laser diffraction particle size analyzer (SALD-2200, Shimadzu Corp.). The density of the HA particles used in PJD was 3.109 g/cm^3, and the median diameter (Fig. 2(a)) was 2.16 μm. Fig. 2(b) shows the TEM bright-field (BF) image of the HA particles before blasting. In TEM, the transmission electrons and scattered electrons of the electron beam transmitted through the sample are used for imaging to observe the microstructure of the sample and analyze its structure. Therefore, it is necessary to use a thin film sample through which electron beams can transmit. All samples for the TEM observation in this study were fabricated into thin films using the focused ion beam (FIB) method. This method uses a Ga ion beam focused from a few to several hundred nanometers and scans the sample surface to produce a thin film using sputter etching. The HA particles were placed on a Cu grid, and a protective film was prepared by C deposition to prevent damage to the material structure during FIB processing. The HA particles were polycrystalline materials comprising approximately 0.5–1 μm-sized crystal grains (Fig. 2(b)). The selected area diffraction (SAD) patterns from the circled regions in A and B in the BF image were identified with $1\bar{1}\bar{1}$ and $10\bar{2}$ spots from the <211> incident beam and 100 and 010 spots from the <001> incident beam of hexagonal HA. Fig. 2(c) shows the X-ray diffraction (XRD) results [18] of the HA particles used in this study; the particles were confirmed to be HA after indexing based on [19]. Fig. 2(d) shows the TEM BF images of the HA substrate microstructure. All HA films, HA substrates, and human enamel observed by TEM in this study were protected by Pt deposition over the entire surface of the samples and subsequently sampled by the FIB. The PJD film and HA substrate were thinned together by the FIB. The HA substrate was 10 mm wide, 25 mm long, and 2 mm thick, with uniform material properties. This substrate had a columnar polycrystalline structure (Fig. 2(d)) similar to human tooth enamel [20]. The columnar polycrystalline structure of human enamel grows toward the tooth surface, and the short-axis cross-section of the column is exposed on the surface. Therefore, HA films were prepared on the top surface shown in Fig. 2(d) under the same conditions as those used for HA film formation on human enamel in the oral cavity. In the acid resistance test, the surface of the HA substrate was polished to measure the change in volume of the HA film over time. A smooth surface was used as the reference for the volume measurement. For comparison with HA films, the human enamel sample shown in Fig. 2(e) was prepared by cutting a human tooth embedded in resin and polishing the cut surface. The polished surface of the human enamel was slightly exposed compared to that of the resin, and the smooth surface of the resin was used as the reference. The HA substrate and human tooth enamel were both polished with a diamond slurry in the grit order of #320, #600, #1000, #1200, #2000, and #4000.

2.2. Fabrication method of HA films

Fig. 3 shows schematics of the PJD apparatus, blasting parameters, HA film formation area, and *xyz* coordinates. PJD was performed using a

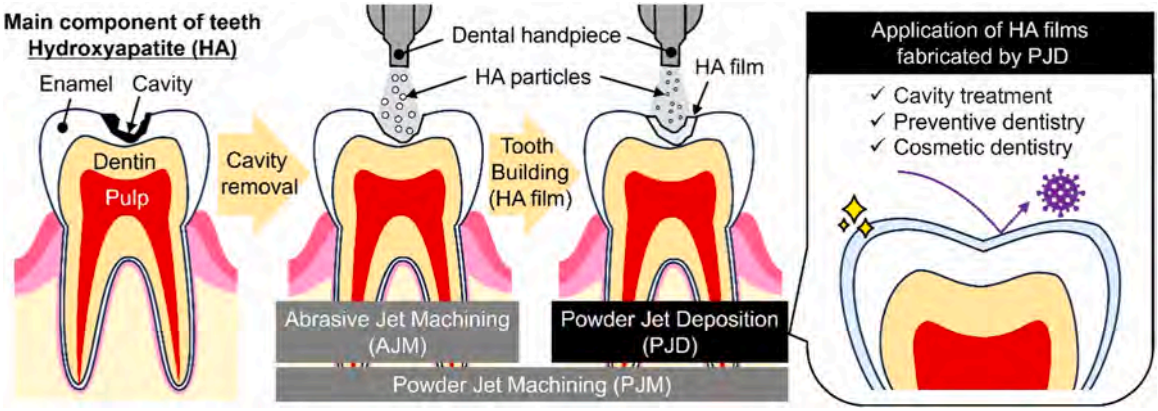

Fig. 1. Schematic of novel dental treatment method.

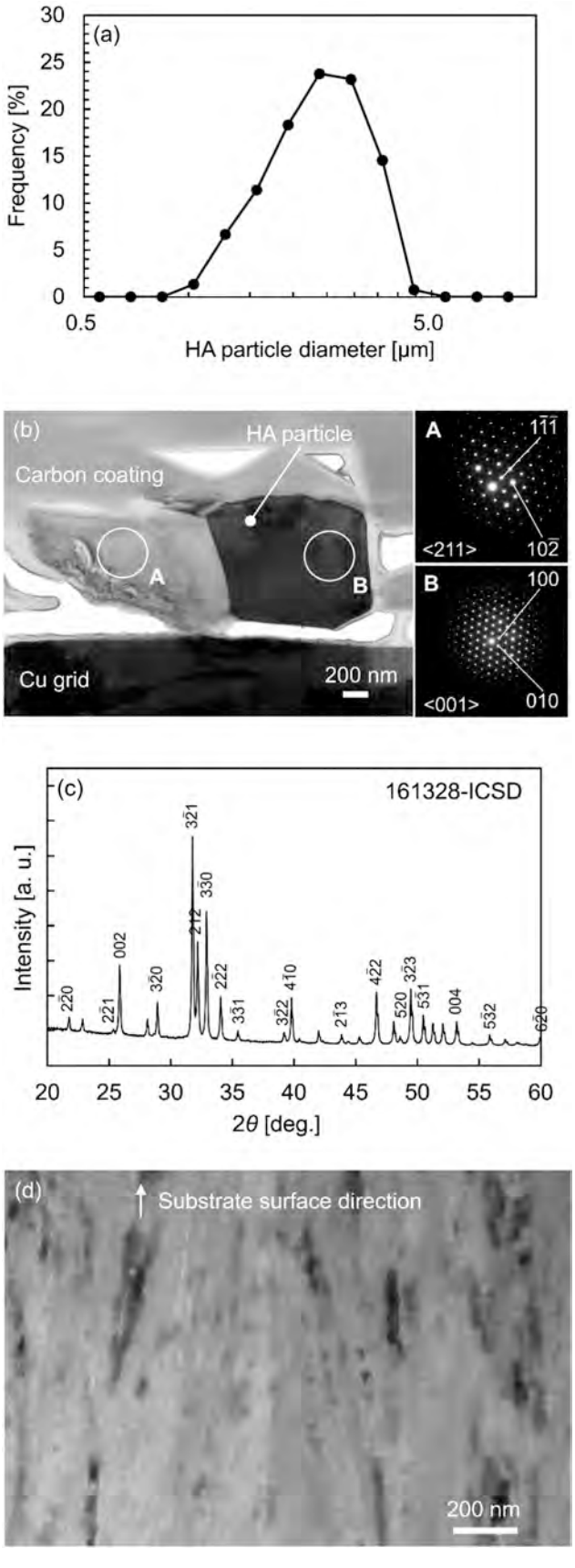

(caption on next column)

Fig. 2. Evaluation results for experimental materials. (a) Size distribution of hydroxyapatite (HA) particles. (b) Cross-sectional transmission electron microscope (TEM) bright-field (BF) images and selected area diffraction (SAD) patterns of the HA particles. The SAD pattern was acquired from the circled regions in A and B and identified $1\bar{1}\bar{1}$ and $10\bar{2}$ spots from the <211> incident beam and 100 and 010 spots from the <001> incident beam of HA. (c) X-ray diffraction (XRD) pattern of HA particles [18]. (c) BF TEM images of the HA substrate. (d) Image of human tooth enamel sample. TEM samples of (b) and (d) were prepared by focused ion beam (FIB) processing.

dental handpiece-shaped device with two internal channels: supply and acceleration (Fig. 3(a)). The HA particles in the particle tank were transported using compressed air through the supply channel to the junction of the two channels. The HA particles were then accelerated using compressed air supplied to the acceleration channel. The acceleration and supply pressures were set to 0.5 MPa. The tank was filled with 2.0 g of HA particles for every film fabrication process, and the remaining HA particles in the tank were removed and replaced with new particles each time the PJD location changed. The distance from the tip of the blasting nozzle to the substrate was defined as the standoff distance d, and the angle between the centerline of the nozzle and substrate was defined as the blasting angle α (Fig. 3(b)). The outer diameter of the blasting nozzle was 3.2 mm; thus, d was 5.0 mm to avoid contact with the substrate, even when the nozzle was tilted. The transition from PJD to AJM has been shown to occur as α becomes more acute; hence, two blasting conditions, $\alpha = 60^\circ$ and 90°, were set for fabricating the HA films [6]. Four HA films were fabricated on one HA substrate, i.e., two each at $\alpha = 60^\circ$ and 90° (Fig. 3(c)). The processing range in the y direction was approximately 4 mm under each α [6]. Therefore, PJD was performed with a spacing of at least 5 mm to avoid overlapping of the HA film fabrication area. A masking tape was used to protect the reference surface of the HA substrate to prevent processing, and the HA films were fabricated in an area approximately 1 mm wide and 3 mm long.

2.3. Acid resistance testing

Fig. 4 shows a schematic of the acid resistance test. To prevent the dissolution of the HA substrate into the acid, the substrate surfaces, except for the HA film area, were masked using a hot-melt adhesive. The prepared human enamel sample (Section 2.1) was attached to the resin part, and the prepared HA film samples (Section 2.2) were attached to the holding area in Fig. 3(c) using a string and suspended from a beaker filled with the acid solution. The acidic solution was prepared according to a protocol used to simulate the acidic environment of the human oral cavity pH 4.5 [21]. A hot plate maintained the solution temperature at 37 °C, the intraoral temperature [22], and a stirrer was used to stir the solution during the test. Thermocouples were used to measure the solution temperature. Tests were performed in 3 h cycles for up to test time $t_{acid} = 12$ h, and the dissolution area and volume of the HA films and human enamel were measured every 3 h using a three-dimensional shape-measuring instrument (NH-3 T, Mitaka Kohki Co., Ltd.). This apparatus enables highly accurate non-contact shape measurements by scanning a point-focus laser beam across the surface of the sample. SEM and TEM were performed to observe the surface and microstructure of the samples, respectively. Because HA exhibits insulating properties, a protective film was prepared by Pt vapor deposition on the SEM observation surface to prevent charging, which could cause the sample surface to be electrically charged and thereby prevent the acquisition of clear images.

2.4. Analysis of the physical phenomena in PJD through SPH

The physical phenomena in PJD were analyzed through SPH, a mesh-free analysis method in ANSYS AUTODYN 14.5. SPH treats the analysis target as a collection of randomly distributed particles. This allows for

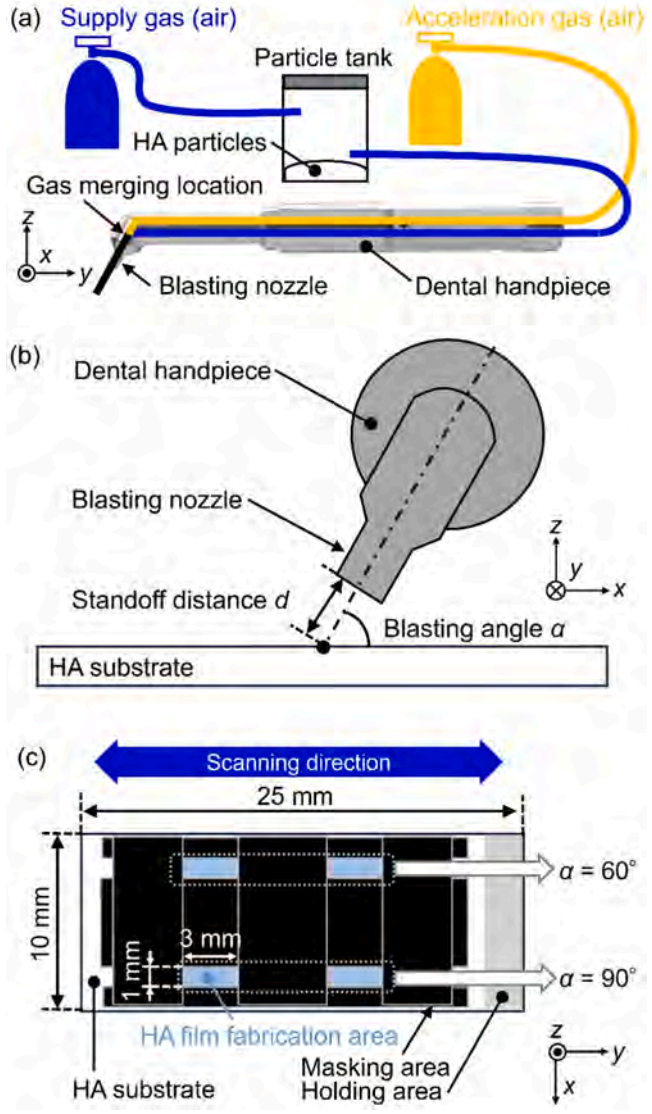

Fig. 3. Schematics of (a) powder jet deposition (PJD) apparatus, (b) blasting parameters, and (c) hydroxyapatite (HA) substrate and HA films.

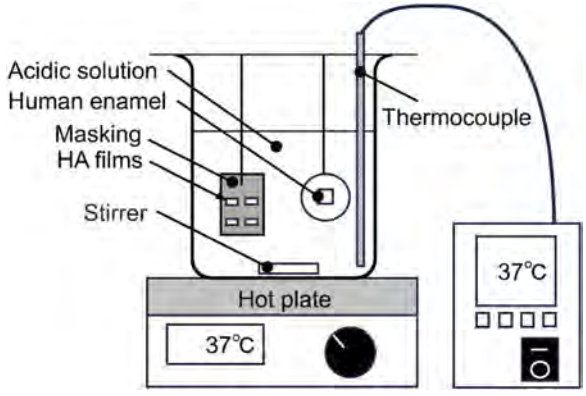

Fig. 4. Schematic of acid resistance test.

the analysis of large deformations that are otherwise difficult to analyze through the mesh method [23]. By placing complementary points that maintain the physical quantities as SPH particles and assigning each node the distribution of a given physical quantity $f(x)$ in the region, as shown in Eqs. (1)–(4), the simulation target is represented as a continuum [23].

$$f(x) \sim \int f(x')W(x-x',\quad h)dx' \tag{1}$$

$$l = |x-x'| \tag{2}$$

$$W(l;h) = \frac{1}{\pi h^3}\begin{cases} 1-\frac{3}{2}q^2+\frac{3}{4}q^3 & (0 \le t \le 1) \\ \frac{1}{4}(2-q)^3 & (1 \le q \le 2) \\ 0 & (2 \le q) \end{cases} \tag{3}$$

$$q = \frac{l}{h} \tag{4}$$

$W(l, h)$ is the kernel function, where l is the distance from the node and h is the smoothing distance (SPH particle diameter).

Fig. 5(a) and (b) show an isometric view of the simulation model and a cross-sectional view in the xz plane at $y = 0$ μm, respectively. The coordinate axes in this analysis were the same as those in Fig. 3, and the origin was set at the point where the HA particles impact the HA

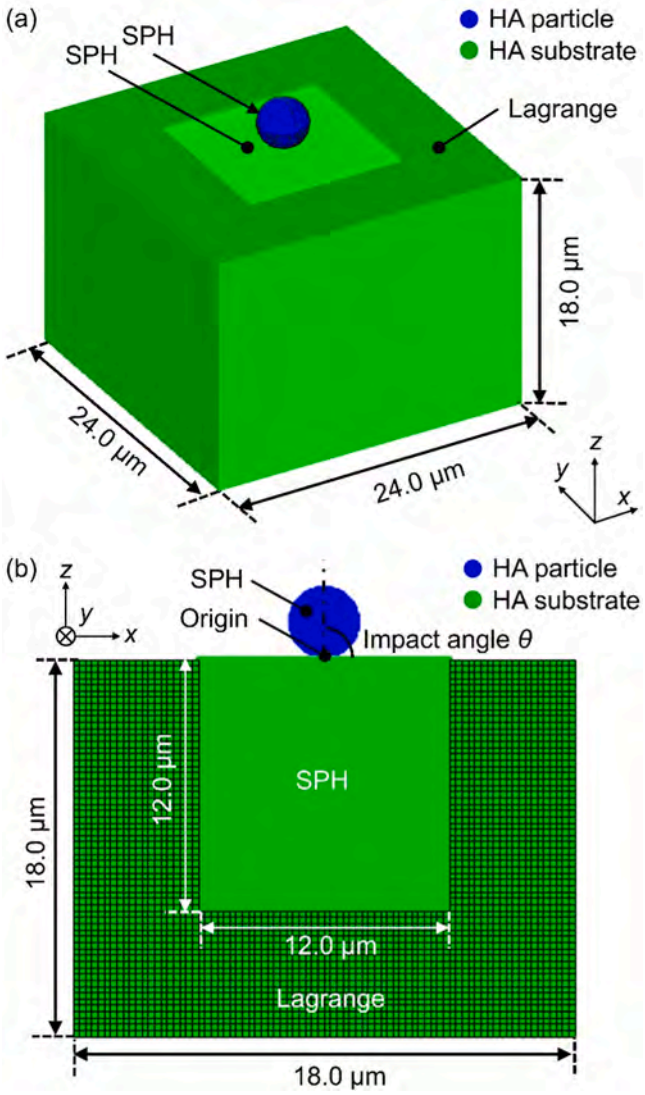

Fig. 5. (a) Isometric image and (b) cross-sectional image in the xz plane at $y = 0$ μm of the particle impact analysis model in powder jet deposition (PJD).

substrate. The physical properties of HA were applied to the particles and substrates. Even when PJD is performed at a constant α, the blasted particles reach the workpiece surface with different angular distributions θ [6]. Therefore, three θ conditions, $\theta = 30^\circ$, 60°, and 90°, were considered in this analysis. To clarify the effect of θ, the HA particles were isotopically spherical. Moreover, d_p was set to 3.2 μm, which was evaluated to be suitable for adhesion processing [13], and the SPH solver was applied. Under the conditions for PJD described in Section 2.2, the HA particles impacted the substrate at approximately v = 300 m/s [6], and the initial velocity v_i was 300 m/s. For the HA substrate geometry, a cubic SPH solver with a side of 12.0 μm was built within the HA particle impact region. A rectangular Lagrange solver with a height of 18.0 μm, width of 24.0 μm, and length of 24.0 μm was built to cover the outside of the SPH solver. All SPH particles were set to h = 0.1 μm, and the Lagrange solver used boundary conditions that allowed shock waves to penetrate (expect the xy plane) at $z = 0$ μm. The Drucker–Prager model was used for the plastic deformation behavior [24].

3. Results

3.1. Volume reduction of the HA film and human enamel after the acid resistance test

Fig. 6 shows the three-dimensional shape change of the samples every 3 h during the acid resistance test. The two samples fabricated at $\alpha = 60^\circ$ shown in Fig. 6(a) and (b) are referred to as HA60–1 and HA60–2, respectively. Those fabricated at $\alpha = 90^\circ$ shown in Fig. 6(c) and (d) are referred to as HA90–1 and HA90–2, respectively. Fig. 6(e) shows the human enamel sample. Similar to the results of the study by Kuji et al. [6], HA90–1 and HA90–2 were thicker than HA60–1 and HA60–2. In addition, HA90–1 and HA90–2 had a heterogeneous film height, and the surface properties of HA60–1 and HA60–2 were smoother than those of HA90–1 and HA90–2. All samples exhibited a gradual decrease in height over time. However, HA60–1 exhibited a sudden decrease in the film thickness during t_{acid} = 6–9 h.

Fig. 7(a) and (b) show the decrease in the sample thickness from t_{acid} = 0 h ΔT and a specific volume V_s every 3 h during the acid resistance test, respectively. The acid-exposed volumes of the HA film and human enamel samples were measured based on the smooth reference surface described in Section 2.1. The HA films were partially defective in deposition; therefore, the height of the reference surface was set to 0 μm, and the initial areas of the HA films were defined as the areas with a deposition height of 1 μm or greater at $t_{acid} = 0$ h in Fig. 6(a)–(d). For the human enamel, the initial area was defined as the acid-exposed area at $t_{acid} = 0$ h, as shown in Fig. 6(e). The reference plane, area, and volume of all samples were set and measured using a three-dimensional shape-measuring instrument's software.

Fig. 7(a) shows the ΔT over 3 h. The sample thickness was the average value calculated by dividing the acid-exposed volume by the initial area. The thicknesses of all samples, except HA60–1 and HA90–2, decreased gradually as t_{acid} progressed. The ΔT values at t_{acid} = 12 h were 3.96, 1.52, 1.56, 0.85, and 2.54 μm for HA60–1, HA60–2, HA90–1, HA90–2, and the human enamel, respectively. This indicates that all samples, except HA60–1, dissolved lesser in acid than the human enamel did. For HA60–1, ΔT was large for t_{acid} = 6–9 h but small for t_{acid} = 0–6 and 9–12 h. Fig. 6(a) also shows that a portion of the HA film was lost simultaneously during t_{acid} = 6–9 h. This indicates that dissolution into the acid occurred when ΔT was small (t_{acid} = 0–6 and 9–12 h), and film peeling occurred when ΔT was large (t_{acid} = 6–9 h). HA90–2 had a rougher surface at $t_{acid} = 0$ h than the other samples, and the accurate volume could not be measured owing to measurement errors. Therefore, V_s was obtained by normalizing the volume exposed to acid at $t_{acid} = 0$ h to 1.0, and the changes in V_s for samples other than HA90–2 were compared (Fig. 7(b)). The V_s of the human enamel continued to decrease at an almost constant rate. By contrast, the decrease in V_s over time for the HA films prepared through PJD was small, particularly at t_{acid} = 0–6 h for HA60–2 and HA-90–1, where no film peeling was observed. Even in HA60–1, where the HA film peeled off during the acid resistance test, the V_s decrease was smaller than that of the human enamel, except at t_{acid} = 6–9 h when the film peeled off.

3.2. Microstructural changes in the HA films caused by acid

Fig. 8 shows typical surface images of the HA films obtained by SEM at $t_{acid} = 0$, 12 h. Fig. 8(a) and (b) show the HA films prepared at $\alpha = 60^\circ$ and $t_{acid} = 0$ and 12 h, and Fig. 8(c) and (d) show those prepared at $\alpha = 90^\circ$ and $t_{acid} = 0$ and 12 h, respectively. Cracks were observed on the surfaces of all HA films after the acid resistance test (Fig. 8(b), (d)) compared to those without testing (Fig. 8(a), (c)). Cracks sized approximately 50–100 μm were observed on the HA films fabricated at $\alpha = 60^\circ$, whereas cracks sized approximately 5–10 μm were observed on the entire surface of the HA films fabricated at $\alpha = 90^\circ$. Although the cracks on the HA films fabricated at $\alpha = 60^\circ$ occurred less frequently than those on the HA films fabricated at $\alpha = 90^\circ$, each crack was approximately 10 times larger.

Fig. 9 shows the TEM images of a cross-sectional HA film prepared on an HA substrate at $\alpha = 90^\circ$ without acid resistance testing; Fig. 9(a) and (b) show BF and dark-field (DF) images, respectively. As shown in Fig. 2, the HA particles used in the PJD were polycrystalline, comprising crystal grains sized approximately 0.5–1 μm. By contrast, the crystals of the HA particles were refined by the impact on the substrate, and the HA film comprised polycrystals sized several tens of nanometers. An amorphous region with a thickness of several hundred nanometers was observed at the boundary between the HA film and HA substrate. The thickness of this amorphous region decreased as α decreased [25]. Fig. 9(c) shows the diffraction image obtained from the HA film in Fig. 9(a), in which the diffraction rings 002, $3\bar{2}1$, and $4\bar{1}0$, corresponding to the diffraction pattern of Fig. 2(c), appear.

Fig. 10 shows TEM images of the HA film and human enamel after acid resistance testing. Fig. 10(a) shows cross-sectional TEM BF images of HA90–1 at t_{acid} = 12 h, and Fig. 10(b) shows the SAD pattern obtained from the circled area of Fig. 10(a). The brightness of the BF image in Fig. 10(a) shows that the upper part of the sample is dense, while the lower part has grain boundaries similar to those in Fig. 9, which is the HA film without acid resistance testing. In the diffraction image obtained from the surface area after the acid resistance test (Fig. 10(b)), only the diffraction ring with the highest diffraction intensity of $3\bar{2}1$ was clearly observed; the diffraction rings of 002 and $4\bar{1}0$ that appeared in the diffraction image of the HA film without the acid resistance test (Fig. 9(c)) were not observed. This suggests that the area near the acid-exposed surface of the HA film was modified by the acid compared to the untested film. Fig. 10(c) shows a TEM BF image of a cross-section of a human enamel sample at t_{acid} = 12 h. It shows that the columnar polycrystals of human enamel exposed to acid are slightly finer than in areas not exposed to acid.

3.3. Stress distribution during HA film fabrication

Fig. 11 shows the stress distribution of an HA particle and substrate in the PJD analyzed using the SPH method. The time when the particle impacted the substrate was defined as $t = 0$ ns, and the stress distribution changed every 0.5 ns from impact to t = 0.5–2.5 ns. The black point at the collision interface illustrated at t = 0.5 ns in Fig. 11(a)–(f) is the origin of the xyz coordinate system, and all figures show the cross-sectional stress distributions in the xz plane at $y = 0$ μm. Fig. 11(a)–(b), (c)–(d), and (e)–(f) show the stress distributions at $\theta = 30^\circ$, 60°, and 90°, respectively. Fig. 11(a), (c) and (e) show the vertical stresses, and Fig. 11(b), (d) and (f) show the shear stresses. The positive direction of the z-axis indicates the direction of positive vertical stress values, and the negative direction of the x-axis indicates the direction of positive

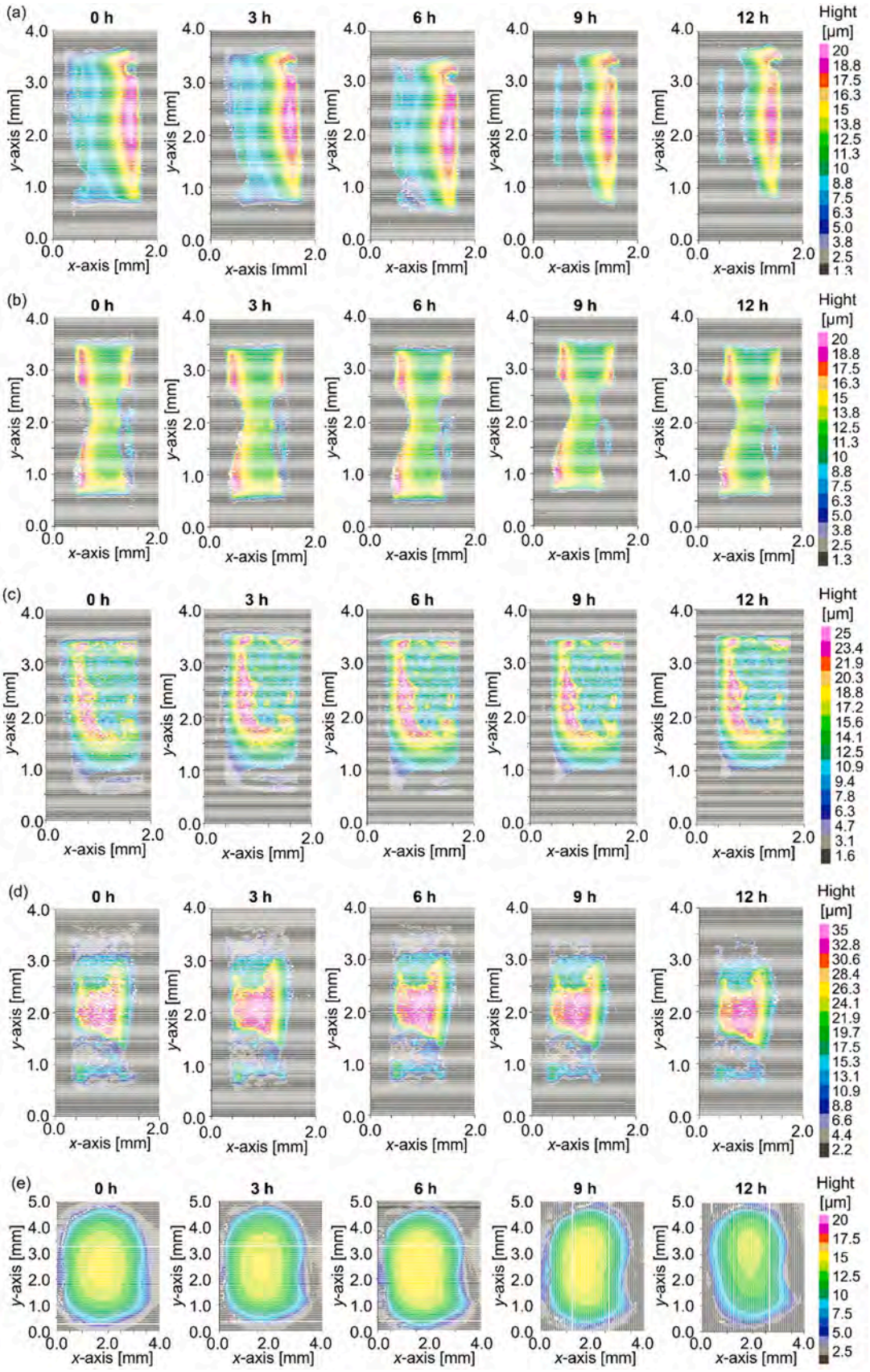

Fig. 6. Three-dimensional shapeshift of the specimens every 3 h in the acid resistance test. (a)–(d) are hydroxyapatite (HA) films fabricated by powder jet deposition (PJD); (a), (b) are HA60–1 and HA60–2 samples fabricated at $\alpha = 60^{\circ}$; (c), (d) are HA90–1 and HA90–2 samples fabricated at $\alpha = 90^{\circ}$; and (e) is a human enamel sample.

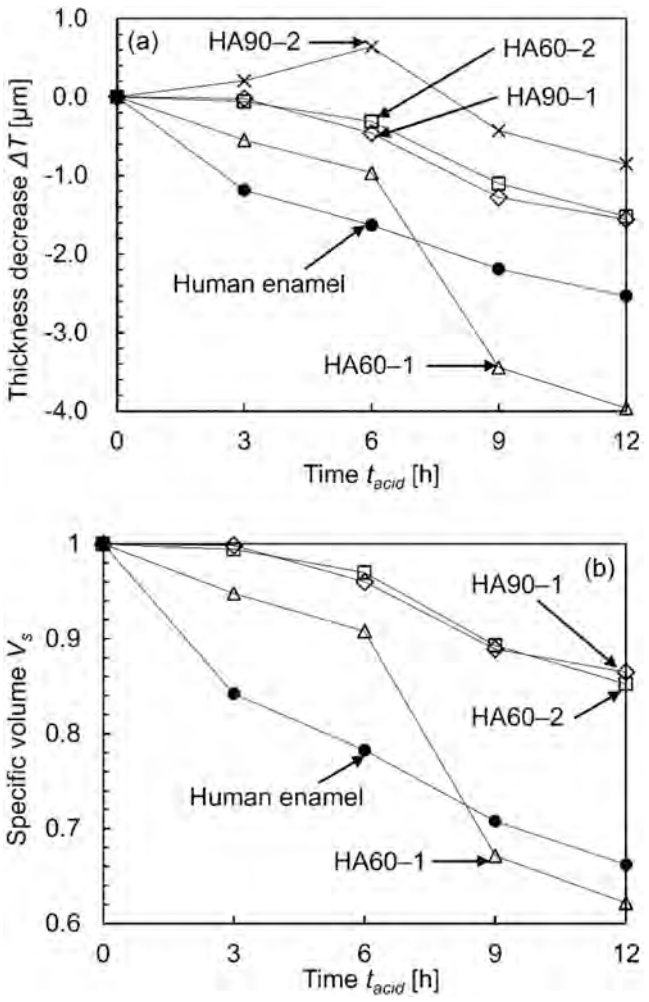

Fig. 7. (a) Thickness change ΔT and (b) specific volume V_s every 3 h for each sample in the acid resistance test.

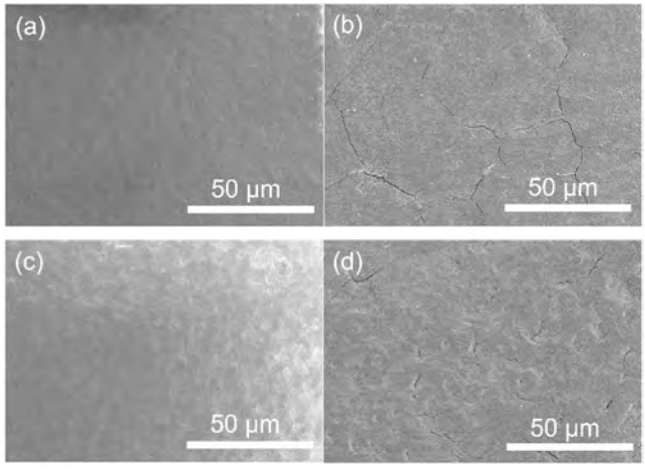

Fig. 8. Typical scanning electron microscopy (SEM) images of the hydroxyapatite (HA) film surface without (0 h) and after 12 h of the acid resistance test. HA films fabricated at (a), (b) $\alpha = 60°$ and (c), (d) $\alpha = 90°$. (a), (c) are the images obtained without testing, while (b), (d) are obtained after the acid resistance test.

shear stress values.

Inside the HA particles, the vertical and shear stresses propagated over a wider area as θ increased, and the fracture area increased. A portion of the HA particles at the collision interface, crushed by the high stress applied during the collision, stacked to form a polycrystalline film, as shown in Fig. 9 [13]. Because HA films are formed by the collision and deposition of multiple HA particles, the stress generated in the HA substrate in this analysis was repeatedly added to the fabricated HA film, and residual stress accumulated. Therefore, the stress distribution in the HA substrate, considered to significantly contribute to the residual stress in the HA film, was compared. First, for the vertical stress, the stress distribution at $x < 0$ μm became wider than that at $x > 0$ μm after $t =$ 1.0 ns for $\theta = 30°$ (Fig. 11(a)) and after $t = 1.5$ ns for $\theta = 60°$ (Fig. 12(c)). In the case of $\theta = 90°$ (Fig. 11(e)), the stress distribution was symmetrical about the *yz*-plane at $x = 0$ μm. These biases in the stress distribution within the HA substrate were more evident for the shear stresses. In the case of $\theta = 30°$ (Fig. 11(b)), the positive shear stress was concentrated at $x < 0$ μm at $t = 0.5$ ns, followed by an expansion of the stress distribution at $x < 0$ μm along with a slight negative stress at $x >$ 0 μm at $t = 1.0$–1.5 ns. After $t = 2.0$ ns, only a positive shear stress occurred. At $\theta = 60°$ in Fig. 11(d), a negative shear stress occurred at $x <$ 0 μm at $t = 0.5$–2.0 ns; however, the positive shear stress at $x > 0$ μm was larger in value and wider in range over all t. After $t = 2.5$ ns, only a positive shear stress occurred. For $\theta = 90°$ (Fig. 11(f)), the shear stress was symmetrically distributed about the *yz*-plane at $x = 0$ μm. That is, the more acute the θ, the more the shear stress applied for a prolonged time, biased toward the direction of the particle impact.

4. Discussion

Acid resistance tests were performed on the HA films prepared through PJD and using human enamel. The HA films exhibited lesser dissolution in acid than the human enamel, and the microstructure of the acid-exposed areas of the HA films exhibited a denser polycrystalline structure compared with that of the human enamel. Thus, the artificial dentinal films fabricated through PJD had a higher acid resistance in the oral cavity than the human enamel. However, HA60–1 peeled off during the acid resistance test, suggesting that α influences the fragility of the HA films. Therefore, the reasons for the difference in acid resistance between the HA films and human enamel are discussed in terms of the microstructure, and HA film peeling is discussed in terms of stress.

4.1. Influence of the microstructure of the HA film and human enamel on the acid resistance

As shown in Figs. 6 and 7, the thicknesses of the HA films and human enamel decrease gradually with t_{acid}. In terms of ΔT, the decrease is greater for the human enamel unless the HA film peeled off. This was attributed to the microstructural differences and chemical reactions between the HA film and human enamel.

First, the acid dissolution rate is discussed. HA films and human enamel are polycrystalline, and display grain boundaries at $t_{acid} = 0$ h. In the oral cavity, acid can penetrate HA films and human enamel through these grain boundaries, and HA is believed to dissolve in the acid. HA crystals have a hexagonal columnar structure, and their dissolution rate in acids has been reported to vary depending on the crystal orientation [26,27]. Human enamel with a columnar polycrystalline structure facing a single direction exhibits the dissolution of HA crystals in the [001] and [011] directions, where the dissolution rate is high, and gaps are created at the grain boundaries to promote acid penetration. By contrast, HA films fabricated through PJD are polycrystalline films with various orientations, unlike the columnar polycrystalline structures of human enamel; therefore, the dissolution rate is relatively low.

Subsequently, the microstructures of the samples at $t_{acid} = 12$ h were compared using TEM images. The HA film prepared through PJD was densely packed to a depth of several micrometers from the acid-exposed

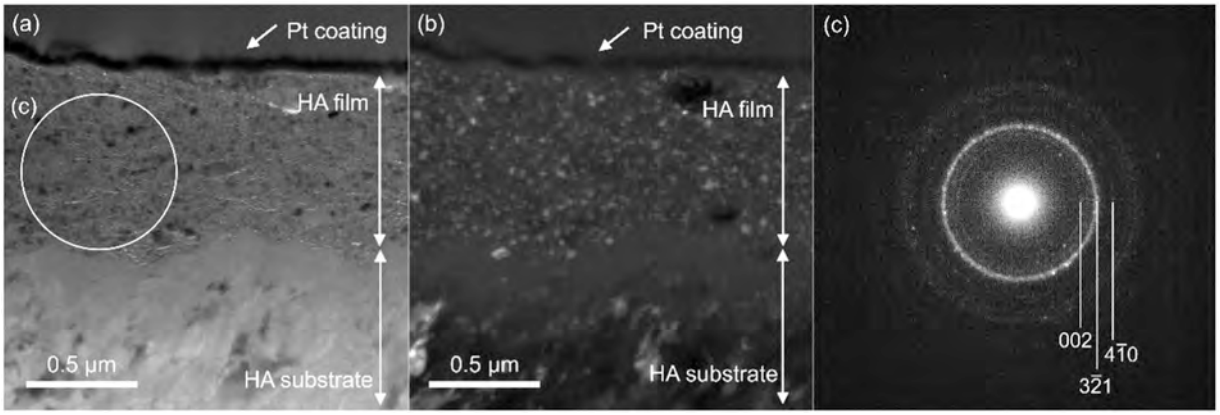

Fig. 9. Transmission electron microscopy (TEM) images of the microstructure of a typical hydroxyapatite (HA) film fabricated at $\alpha = 90^{\circ}$ without acid resistance testing: (a) bright-field image, and (b) dark-field image. (c) Selected area diffraction (SAD) patterns of HA film acquired from the circled regions of (a). The observed sample was processed by an FIB from an area with a sufficiently small thickness of the HA film.

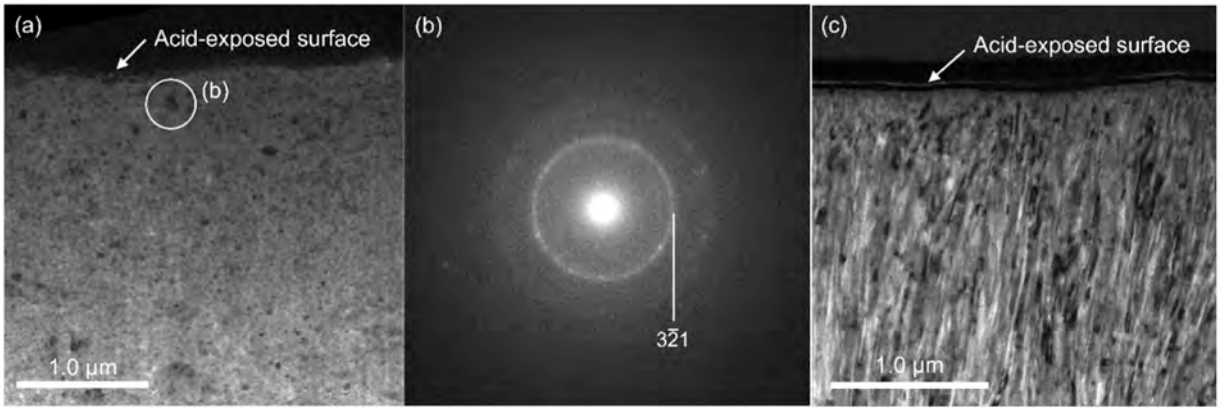

Fig. 10. Transmission electron microscopy (TEM) images of the microstructure of the hydroxyapatite (HA) film fabricated at $\alpha = 90^{\circ}$ and human enamel after 12 h of acid resistance testing. (a) Bright-field images of the acid-exposed surface of the HA film, and (b) diffraction image obtained from the white-circled area in (a). (c) Bright-field image of the acid-exposed surface of the human enamel sample.

surface (Fig. 10(a)), though the human enamel exhibited grain refinement near the acid-exposed surface (Fig. 10(c)). This indicates that densification of the microstructure did not occur in the human enamel as in the HA films. The test solution used in this experiment was an acidic mixture of lactic acid ($CH_3CH(OH)COOH$), calcium chloride ($CaCl_2$), and potassium dihydrogen phosphate (KH_2PO_4), with the hydrogen ion index maintained at pH = 4.5 [21]. HA is a basic calcium phosphate with the chemical formula $Ca_{10}(PO_4)_6(OH)_2$ and excellent ion exchange properties [28]. Therefore, the OH group of HA and the H group of the acidic solution underwent an acid–base reaction, as shown in Eq. (5).

$$Ca_{10}(PO_4)_6(OH)_2 + 8H^{+} \Rightarrow 10Ca^{2+} + 6(HPO_4)^{2-} + 2H_2O \quad (5)$$

The HA films fabricated through PJD were densified because of the chemical reaction in Eq. (5), causing shrinkage. The small volume loss of the HA films fabricated up to t_{acid} =6 h is attributed to the densification of the HA films, which prevented acid penetration. After $t_{acid} = 6$ h, the volume loss rate was similar to that of the human enamel, which can be attributed to acid penetration through the cracks, as shown in Fig. 8. By contrast, human enamel contains HA and other inorganic and organic substances. Thus, effects other than the chemical reaction between HA and the acid may have prevented densification. Nevertheless, in the human enamel, the crystal grains exposed to the acid became finer. This indicates that the dissolution of HA into the acid occurred gradually, decomposing the crystal structure into finer grains.

4.2. *Effect of stress on the acid fragility of the HA film*

After the acid resistance test, many cracks appeared on the surfaces of the HA films (Fig. 8). The cracks in the HA film fabricated at $\alpha = 60^{\circ}$ occurred less frequently but were larger than those in the HA film fabricated at $\alpha = 90^{\circ}$. The cracks in the HA film fabricated at $\alpha = 90^{\circ}$ were more frequent, but each crack was approximately 1/10 the size of those in the HA film fabricated at $\alpha = 60^{\circ}$.

The generation of these cracks is attributed to the chemical reaction occurring when HA is dissolved in an acid. As described in Section 4.1, HA undergoes an acid–base reaction described by Eq. (5), resulting in the densification of the HA film due to dissolution and shrinkage. This shrinkage inevitably causes cracks on the HA film surface.

The propagation of cracks generated by chemical reactions is considered to be strongly related to the residual stresses generated during the fabrication of HA films through PJD. In general, the tensile residual stress inside a material promotes crack propagation during fatigue and stress corrosion cracking, whereas the compressive residual stress suppresses crack propagation [29]. As shown in Fig. 11, the vertical stress along the *z*-axis and shear stress along the *x*-axis simultaneously occur in the HA film owing to PJD. The vertical stress along the *z*-axis is considered to be a compressive residual stress inhibiting crack propagation, whereas the shear stress along the *x*-axis is a tensile residual stress promoting crack propagation. Comparing Fig. 11(a), (c), and (e), the compressive stress values in the substrate were larger and spread over a wider area as θ increases. Peng et al. [30] showed that

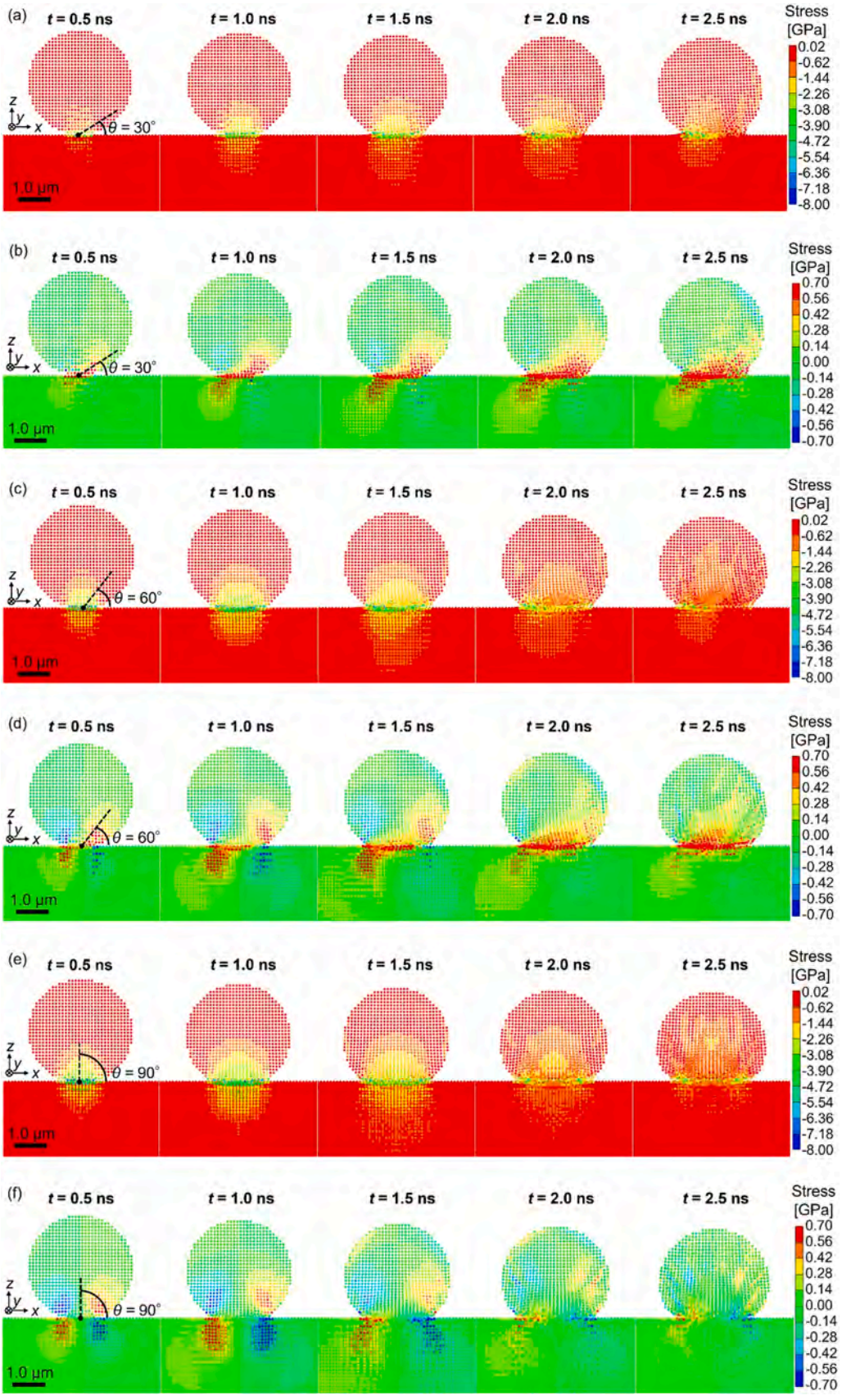

Fig. 11. Stress distributions in the *xz* plane at $y = 0$ μm for a hydroxyapatite (HA) particle and substrate in powder jet deposition (PJD) analyzed through the smoothed particle hydrodynamics (SPH) method. Stress distributions at (a) and (b) $\theta = 30°$; (c) and (d) $\theta = 60°$; (e) and (f) $\theta = 90°$. (a), (c), and (e) show vertical stresses, while (b), (d), and (f) show shear stresses.

stress loading due to mastication causes the fragmentation of the columnar crystal structure of HA in the human tooth surface layer, resulting in surface hardening. In addition, grain refinement is a strengthening technique in metallic materials that had been shown to increase the hardness even in HA [31]. These facts imply that a compressive residual stress, which suppresses crack propagation, is most likely to occur when $\theta = 90^\circ$, and that the HA film is mechanically strengthened. Subsequently, the shear stress, which affects the tensile residual stress, was examined. At $\theta = 90^\circ$, the shear stress was symmetrically distributed from the particle impact area (Fig. 11(f)). The shear stresses canceled each other out in the shear direction, and the compressive residual stresses in the vertical direction were primarily generated in the film. Conversely, as θ became more acute, the shear stress distribution became more biased toward the direction of particle impact. In addition, the value and range of shear stress in the negative direction, significant for canceling the residual stress, decreased, and the time of occurrence became shorter. Thus, the HA films fabricated at a smaller θ had higher tensile residual stresses, promoting crack propagation. Because more HA particles collide with a smaller θ for a smaller α, the HA films fabricated at $\alpha = 60^\circ$ were subjected to higher tensile residual stresses, which may have resulted in crack propagation and peeling of the HA films. By contrast, the HA films fabricated at $\alpha = 90^\circ$ exhibited higher stress during fabrication. Fig. 6(c) and (d) show that the surface roughness of the films has increased, with the observation of deposition defects. Therefore, α should be reduced to some extent to fabricate smoother HA films.

In summary, HA films fabricated through PJD were chemically transformed into a dense and strong crystalline structure through the chemical reaction with the acid in the oral cavity and exhibited improved acid resistance compared with that of human enamel. However, as α decreased, the stress distribution became biased, resulting in tensile residuals that caused the HA films to peel off more easily. Conversely, for $\alpha = 90^\circ$, the surface properties were degraded owing to the higher applied stresses. Therefore, when fabricating HA films through PJD, the particles should be blasted in multiple directions to avoid stress bias.

5. Conclusions

The acid resistance of HA films prepared through PJD in the oral cavity was investigated to evaluate the usefulness of a novel dental treatment method. HA films were fabricated through PJD at two different blasting angles, $\alpha = 60^\circ$ and 90°, and their acid resistance was compared with that of human enamel. The acid resistance was tested using an acidic solution simulating the human oral cavity environment. The following conclusions were drawn:

(i) Part of the HA film fabricated at $\alpha = 60^\circ$ peeled off during the acid resistance test. However, the decrease in thickness of the HA film fabricated at any α was smaller than that of the human enamel unless the film peeled off, indicating that the HA film was highly acid-resistant.

(ii) The crystal grains near the acid-exposed surfaces of the human enamel became finer. This indicates that the human enamel gradually dissolved into the acid, while its crystal structure decomposed finely.

(iii) TEM revealed that the microstructure near the acid-exposed surface of the HA film shrank owing to the chemical reaction and became densely modified. By contrast, the human enamel did not show the same microstructural densification as that of the HA film owing to the influence of components other than HA.

(iv) The densification of the HA film resulted in cracking, and the cracks appearing on the surface of the HA film fabricated at $\alpha = 60^\circ$ after the acid resistance test were approximately 10 times larger than those fabricated at $\alpha = 90^\circ$.

(v) SPH analysis suggested that the smaller the HA particle impact angle θ, the greater the tensile residual stress affecting crack growth and HA film peeling.

The development of HA films with superior acid resistance may lead to more resilient dental restorations and coatings. This may reduce the need for frequent replacements due to degradation over time and enhance the overall quality and durability of dental treatments.

Funding

This study did not receive any specific grants from funding agencies in the public, commercial, or non-profit sectors.

CRediT authorship contribution statement

Keiichi Sasaki: Writing – review & editing, Conceptualization. **Masayoshi Mizutani:** Writing – review & editing, Methodology, Conceptualization. **Keita Shimada:** Writing – review & editing. **Kuniyuki Izumita:** Writing – review & editing, Investigation. **Chieko Kuji:** Writing – original draft, Visualization, Software, Methodology, Investigation, Conceptualization. **Tsunemoto Kuriyagawa:** Writing – review & editing, Methodology, Conceptualization.

Declaration of Competing Interest

The authors declare that they have no known competing financial interests or personal relationships that could have appeared to influence the work reported in this paper.

Data Availability

Data will be made available on request.

Acknowledgements

This work was partially supported by Nanotechnology Platform Project, MEXT, Japan (project number A-16-TU-0032).

References

[1] Y. Ueda, Structure of tooth and treatment of caries, J. Jpn. Foundry Eng. Soc. 70 (1998) 219–222, https://doi.org/10.11279/jfes.70.219.
[2] J.W.V. van Dijken, Direct resin composite inlays/onlays: an 11 year follow-up, J. Dent. 28 (2000) 299–306, https://doi.org/10.1016/S0300-5712(00)00010-5.
[3] A. Haitham, K. Joachim, G. Gerd, S. Falk, Secondary caries risk of different adhesive strategies and restorative materials in permanent teeth: Systematic review and network meta-analysis, https://doi.org/103541. J. Dent. 104 (2021) 103541 https://doi.org/10.1016/j.jdent.2020.103541.
[4] R. Melentiev, F.Z. Fang, Recent advances and challenges of abrasive jet machining, CIRP J. Manuf. Sci. Technol. 22 (2018) 1–20, https://doi.org/10.1016/j.cirpj.2018.06.001.
[5] C. Nishikawa, K. Mizutani, T.F. Zhou, J.W. Yan, T. Kuriyagawa, Investigation of particle impact phenomena in powder jet deposition process, Key Eng. Mater. 523–524 (2012) 184–189, https://doi.org/10.4028/www.scientific.net/KEM.523-524.184.
[6] C. Kuji, K. Izumita, K. Shimada, M. Mizutani, K. Sasaki, T. Kuriyagawa, Influence of the impact angle on machining in powder jet processing, Int. J. Autom. Technol. 17 (2023) 5–13, https://doi.org/10.20965/ijat.2023.p0005.
[7] L. Pawlowski, Suspension and solution thermal spray coatings, Surf. Coat. Technol. 203 (2009) 2807–2829, https://doi.org/10.1016/j.surfcoat.2009.03.005.
[8] N. Bala, H. Singh, J. Karthikeyan, S. Prakash, Cold spray coating process for corrosion protection: a review, Surf. Eng. 30 (2014) 414–421, https://doi.org/10.1179/1743294413y.0000000148.
[9] M. Schubert, D. Hanft, T. Nazarenus, J. Exner, M. Schubert, P. Nieke, P. Glosse, N. Leupold, J. Kita, R. Moos, Powder aerosol deposition method - novel applications in the field of sensing and energy technology, Funct. Mater. Lett. 12 (2019) 1930005, https://doi.org/10.1142/s1793604719300056.
[10] H. Aoki, Marvelous biomaterial, apatite, Ishiyaku Publishers Inc, Tokyo, 1999.
[11] L.L. Hench, Bioceramics, J. Am. Ceram. Soc. 81 (1998) 1705–1728, https://doi.org/10.1111/j.1151-2916.1998.tb02540.x.
[12] R. Akatsuka, K. Sasaki, M.S.S. Zahmaty, M. Noji, T. Anada, O. Suzuki, T. Kuriyagawa, Characteristics of hydroxyapatite film formed on human enamel

with the powder jet deposition technique, J. Biomed. Mater. Res. Part B-Appl. Biomater. 98B (2011) 210–216, https://doi.org/10.1002/jbm.b.31781.
[13] M. Mizutani, C. Kuji, H. Ohisa, S. Nishimura, K. Mizutani, R. Akatsuka, K. Sasaki, S. Xu, K. Shimada, T. Kuriyagawa, Particle fracture behavior and deposition mechanism in powder jet deposition (PJD), J. Jpn. Soc. Abras. Technol. 61 (2017) 28–33, https://doi.org/10.11420/jsat.61.28.
[14] R. Akatsuka, K. Matsumura, M. Noji, C. Nishikawa, K. Sato, T. Hagiwara, T. Anada, O. Suzuki, T. Kuriyagawa, K. Sasaki, Evaluation of hydroxyapatite film by powder jet deposition after artificial aging, Key Eng. Mater. 529–530 (2013) 229–232, https://doi.org/10.4028/www.scientific.net/KEM.529-530.229.
[15] C. Loke, J. Lee, S. Sander, L. Mei, M. Farella, Factors affecting intra-oral pH – a review, J. Oral. Rehabil. 43 (2016) 778–785, https://doi.org/10.1111/joor.12429.
[16] A. Lussi, N. Schlueter, E. Rakhmatullina, C. Ganss, Dental erosion - an overview with emphasis on chemical and histopathological aspects, Caries Res. 45 (2011) 2–12, https://doi.org/10.1159/000325915.
[17] Y.N. Umalkar, N. Mankar, R. Rajnekar, S. Sathe, Pit and fissure sealants, J. Res. Med. Dent. Sci. 10 (2022) 52–56.
[18] A. Tomie, C. Kuji, H. Ohisa, K. Shimada, M. Mizutani, K. Sasaki, T. Kuriyagawa, Fabrication of hydroxyapatite film by powder jet deposition, https://doi.org/10.1299/transjsme.15-00189, Trans. JSME 81 (2015) 15–00189, https://doi.org/10.1039/B804140G.
[19] G. Renaudin, P. Laquerrière, Y. Filinchuk, E. Jallotd, J.M. Nedelec, Structural characterization of sol–gel derived Sr-substituted calcium phosphates with anti-osteoporotic and anti-inflammatory properties, J. Mater. Chem. 18 (2008) 3593–3600.
[20] E.R. Dumont, Mammalian enamel prism patterns and enamel deposition rates, Scanning Microsc. 9 (1995) 429–442.
[21] M. Sugai, Y. Matsuda, M. Nagayama, M. Kaga, Y. Yawaka, Comparison of enamel demineralization between deciduous and permanent teeth uusing the automatic pH-cyclingsystem, Jpn. J. Pediatr. Dent. 48 (2010) 48–55, https://doi.org/10.11411/jspd.48.1_48.
[22] Y. Nakamura. Basic physiology for dental students, 4th ed, Ishiyaku Publishers Inc, Tokyo, 2003.
[23] G. Yagawa, Y. Kanto, H. Okuda, Computational mechanics, Iwanami Shoten, Tokyo, 2005.
[24] T. Tanabe, T. Higai, H. Umehara, J. Niwa, Concrete structure, Asakura Shoten Co. Ltd, Tokyo, 1992.
[25] Anon.
[26] K.Y. Kwon, E. Wang, N. Chang, S.W. Lee, Characterization of the dominant molecular step orientations on hydroxyapatite (100) surfaces, Langmuir 25 (2009) 7205–7208, https://doi.org/10.1021/la900824n.
[27] S.V. Dorozhkin, Dissolution mechanism of calcium apatites in acids: a review of literature, World J. Methodol. 2 (2012) 1–17, https://doi.org/10.5662/wjm.v2.i1.1.
[28] S. Sugiyama, T. Ichii, H. Matsumoto, H. Hayashi, Effect of calcination and sieving of calcium hydroxyapatite on ion-exchangeability with lead cation in the presence and absence of HCl, Adv. Environ. Res. 6 (2002) 285–289, https://doi.org/10.1016/s1093-0191(01)00059-4.
[29] J. Vaara, A. Kunnari, T. Frondelius, Literature review of fatigue assessment methods in residual stressed state, Eng. Fail. Anal. 110 (2020) 104379, https://doi.org/10.1016/j.engfailanal.2020.104379.
[30] J.P. Peng, H. Xiao, D. Yang, L. Lei, J. Zheng, Z.R. Zhou, Surface hardening behavior of enamel by masticatory loading: occurrence mechanism and antiwear effect, ACS Biomater. Sci. Eng. 6 (2020) 4454–4461, https://doi.org/10.1021/acsbiomaterials.0c00740.
[31] H. Zeng, X. Jin, Y. Xiong, Enhanced hardness of transparent HAp ceramic by microstructure refinement, J. Wuhan. Univ. Technol. Mater. Sci. Ed. 34 (2019) 254–258, https://doi.org/10.1007/s11595-019-2043-9.

Materials & Design 249 (2025) 113566

Contents lists available at ScienceDirect

Materials & Design

journal homepage: www.elsevier.com/locate/matdes

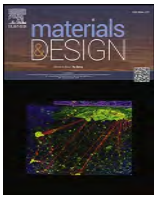

Clarification of shear deformation behavior in Fe–Si amorphous alloys by molecular dynamics

Chieko Kuji [a,*], Narumasa Miyazaki [b,1], Masayoshi Mizutani [c], Keita Shimada [d], Nobuki Ozawa [b,e], Momoji Kubo [b,e], Tsunemoto Kuriyagawa [f]

[a] Department of Mechanical Systems Engineering, Graduate School of Engineering, Tohoku University, Sendai 980-8579, Japan
[b] Institute for Materials Research, Tohoku University, Sendai 980-8577, Japan
[c] Research Center for Green X-Tech, Green Goals Initiative, Tohoku University, Sendai 980-8577, Japan
[d] Department of Mechanical Engineering, Nihon University, Koriyama 963-8642, Japan
[e] New Industry Creation Hatchery Center, Tohoku University, Sendai 980-8579, Japan
[f] Center for Co-Creation Strategy, Tohoku University, Sendai 980-8577, Japan

ARTICLE INFO

Keywords:
Amorphous alloy
Structural relaxation
Molecular dynamics
Tensile test
Shear band

ABSTRACT

Two $Fe_{85}Si_{15}$ amorphous alloy models were created based on molecular dynamics with different cooling rates of 10^{10} K/s (slower model) and 10^{12} K/s (faster model) and examined the effects of atomic structure on the mechanical properties and shear band (SB) propagation behavior, which determines the shear processing quality. Voronoi analysis of the short-range ordered structures (SRO) revealed that the slower model has more full icosahedral SROs than the faster model, and Young's modulus and tensile strength were 11 % and 14 % higher than those of the faster model, respectively. Indentation calculations presuming crack propagation during shear processing were then performed on both models. Only in the case of the slower model, the icosahedral SRO in the SB changed to intermediate structures, increasing the distorted body-centered cubic (BCC) structure. The SB in the faster model spread out isotropically from the indenter, whereas that in the slower model propagated in the indent direction. These results indicate that intermediate and distorted BCC structures in the SB provide directionality to the SB propagation and suggest that the slower model, in which cracks propagate toward the shear direction of the material and break it in a straight line, may produce a higher-quality surface in shear processing.

1. Introduction

Metals that become supercooled liquids by rapid cooling do not form crystalline structures but, rather, become metastable solids below the glass transition temperature while maintaining random structures [1,2]. This type of metallic material, which solidifies without translational symmetry, is called an amorphous alloy and was discovered by Duwez in 1960 [3]. Amorphous alloys exhibit various properties owing of their unique structures [4]. In particular, Fe-based amorphous alloys exhibit excellent performance in terms of high strength [5], high corrosion resistance [6], and high soft-magnetic properties [7]. For example, the iron loss of Fe–Si–B amorphous alloy, a typical Fe-based amorphous alloy, is approximately 0.05 W kg^{-1} (50 Hz, 1 T), which is 1/10 that of a non-oriented electromagnetic steel sheet [8]. Because of this low iron loss, it is being considered for application as a soft magnetic material in motor cores and other devices [9–11].

Single-roll liquid quenching is widely used for the mass production of amorphous alloys [12], which are generally made available today as thin strip alloys with thicknesses of approximately 20–30 μm. Such thin sheet materials are typically processed via shear processing by pressing, which is widely used because of its high productivity [13]. Fig. 1 shows a schematic of shear processing. As shown in Fig. 1(a), shear processing utilizes shear deformation caused by compressive forces from a pair of tools called a punch and die. When the punch bites beyond a certain level, cracks are generated and subsequently propagate and fracture (Fig. 1(b)) [14]. The cut surface is composed of four elements: (i) a shear droop generated by material draw-in, (ii) a sheared face created by punch bite, (iii) a broken face generated by crack growth, and (iv) burrs

* Corresponding author.
E-mail addresses: c-kuji@tohoku.ac.jp (C. Kuji), miyazaki.narumasa@kobelco.com (N. Miyazaki), masayoshi.mizutani.b6@tohoku.ac.jp (M. Mizutani), shimada.keita@nihon-u.ac.jp (K. Shimada), nobuki.ozawa.c8@tohoku.ac.jp (N. Ozawa), momoji@tohoku.ac.jp (M. Kubo), tkuri@tohoku.ac.jp (T. Kuriyagawa).
[1] Kobe Corporate Research Laboratories, Kobe Steel, 651-2271, Japan (current address of N. Miyazaki).

https://doi.org/10.1016/j.matdes.2024.113566
Received 30 October 2024; Received in revised form 12 December 2024; Accepted 23 December 2024
Available online 25 December 2024

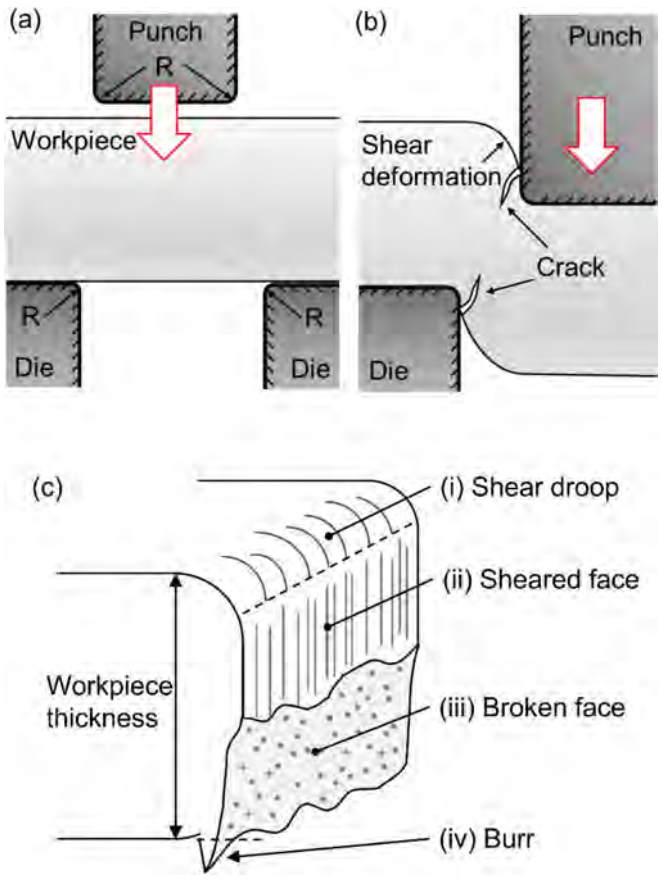

Fig. 1. Schematic of shear processing. (a) Closs-sectional view of shear processing, (b) magnified view of deformation area of (a), and (c) schematic diagram of machined cross section, which is divided into four parts: (i) shear droop, (ii) sheared face, (iii) broken face, and (iv) burrs.

on the bottom surface of the material (Fig. 1(c)). Among these elements, the growth of cracks generated from the punch-cut edge, which corresponds to (iii), plays an important role in shear processing [15]. If the direction of crack growth can be controlled, a favorable machined surface can be obtained [14]. This is especially true for high-speed shear processing, which produces a smooth fracture surface over the entire cut surface; the deformation zone of the material is narrowed, resulting in a good fracture surface with little shear droop and high squareness [16]. However, the shear processing of amorphous alloys is problematic because of the extremely low plate thickness and high tool wear caused by their high material strength [17]. Typical machining defects include the generation of burrs larger than the plate thickness, lack of edges due to shear failure, and cracks in the machining area [17].

To improve the machinability of amorphous alloys, the shear processing method known as blanking and its use in conjunction with the structural changes caused by heat treatment were investigated [18–21]. When metastable amorphous alloys are heated, the atoms move to energetically stable positions and then crystallize [18,22–24]. The very slight structural changes that occur before crystallization to stabilize the energy of the system are referred to as “structural relaxation,” which changes the mechanical properties while maintaining the amorphous structure of the alloy [18,24–27]. Because each property of an amorphous alloy is derived from its amorphous structure, the product performance is determined by the degree to which the amorphous structure can be maintained. Therefore, heat treatment to improve machinability should ideally be limited to a state of structural relaxation without crystallization. Our micro-tensile and machining tests have shown that structural relaxation significantly reduces the tensile strength and toughness of amorphous alloys [19], allowing for reduced machining resistance and improved machining quality [20]. Furthermore, it has been shown that the improved machinability via structural relaxation can be restricted to the few-micrometer region involved in the machining [21]. However, unlike clear structural changes, such as crystal precipitation, structural relaxation is caused by small movements of atoms, making it difficult to identify the structural changes using direct observation techniques.

Molecular dynamics (MD) have been used to analyze the structures and elucidate the mechanical properties of amorphous alloys, which otherwise cannot be realized by direct observation [28]. For example, Lashgari et al. clarified the effect of crystallization due to heat treatment on the material properties of amorphous alloys using MD in conjunction with nanoindentation experiments [29–33], whereas Nakatani et al. investigated brittle fracture behaviors and mechanical properties during crack propagation in a monogenic amorphous model [34–37]. Matsumoto et al. investigated the influence of size and volume fractions of nanocrystals in amorphous alloys on mechanical properties [38,39]. However, we have not found any research studies that investigated the deformation behaviors of commercially used amorphous alloy systems consisting of metal–semimetal atoms, while focusing on slight differences in the energy state or atomic structure, such as structural relaxation.

Therefore, herein, we performed an MD study with two objectives. The first objective was to investigate the effects of small differences in the energy state and atomic structures of amorphous alloys on their mechanical properties, such as Young’s modulus and tensile strength. The second was to clarify the effect of such differences in atomic structure on shear band (SB) propagation and to provide new insights into shear processing as an industrially applied process. In the experiments, the ability to form amorphous alloys depended on the atomic species and composition ratio. Fe-based binary amorphous alloys exhibit amorphous formation abilities at compositions with 10 at% to 20 at% half-metals [40] and are particularly prone to amorphization with Si and B half-metals [12]. Among these, the relationship between Fe and Si has been of interest to researchers. Si has been reported to play an important role in promoting crystallization from structural relaxation in multisystem Fe-based amorphous alloys [18]. In this study, a model for a binary system composed of transition metal Fe and 15 at% semimetal Si was investigated. To produce slight differences in the energy state and atomic structure, the amorphous alloy models were constructed using two different cooling rates. For the first objective, the created amorphous alloy models were evaluated based on their potential energies and atomic packing factors (APFs), and the mechanical properties were assessed using uniaxial tensile calculations. For the second objective, indentation calculations were performed for each cooling rate amorphous alloy model assuming a compressive load from the punch tip, such that the compressive force generates an SB. The short-range ordered structures (SROs) of the pre-indentation and post-indentation SBs were obtained via Voronoi analysis, and finally, the differences in SB propagation behavior between the models created with different cooling rates were discussed.

2. Calculation methods

In this study, the simulations were performed using the LAMMPS software program (version 29 Oct 2020 https://lammps.sandia.gov) [41]. The second nearest-neighbor modified embedded atom method (2NN-MEAM) proposed by Jelinek et al. for the Al–Si–Mg–Cu–Fe system was employed for the interatomic potentials [42]. In 2NN-MEAM, the angle-dependent terms of the atoms are taken into account, and the potential energy, lattice constant, elastic modulus, single-crystal structures such as those of Fe and Si, and B2 crystal structures such as that of FeSi are well reproduced [41]. The 2NN-MEAM model has also been reported to be able to qualitatively reproduce the work softening behavior of Fe-based amorphous metals [29]. Meanwhile, the calculation results were visualized using OVITO (version 3.3.4 27 Nov 2020 htt

ps://www.ovito.org) [30].

Fig. 2 shows the typical unit cell models. First, a body-centered cubic (BCC) unit cell model (BUM) with a side length of 42.75 Å, consisting of 6750 atoms in total, was prepared (Fig. 2(a)). Atoms were randomly arranged at the lattice points of the BCC structure such that the ratio of Fe atoms to Si atoms was 85:15 (Fig. 2(b)). Periodic boundary conditions were then applied in all directions of the Fe and $Fe_{85}Si_{15}$ BUM, and the model was heated from an initial temperature of 0 K to 3000 K at a heating rate of 3.0×10^{13} K/s using an isothermal–isobaric (NPT) ensemble. To further melt the model, it was held at 5000 K for 100 ps, cooled to 3000 K at a rate of 2.0×10^{13} K/s using the canonical (NVT) ensemble, and again held at 3000 K for 100 ps using the NPT ensemble. Afterward, the fully melted $Fe_{85}Si_{15}$ BUM was quenched to 300 K at one of two different rates, i.e., 10^{10} K/s or 10^{12} K/s, using the NPT ensemble to produce a unit cell model of the amorphous alloy (AUM) for each of the two different cooling rates. Fig. 2(c) shows the $Fe_{85}Si_{15}$ AUM cooled at 10^{10} K/s. The timestep for the cooling calculation at the rate of 10^{10} K/s was set to 4 fs, while the timestep for all other calculations was set to 1 fs. The Parrinello–Rahman method was used for pressure control [43,44], and the Nosé–Hoover thermostat was used for temperature control [45,46].

Uniaxial tensile calculations were performed on the Fe BUM (Fig. 2(a)) and $Fe_{85}Si_{15}$ AUM (Fig. 2(c)) to evaluate the mechanical properties of each model. First, periodic boundary conditions were applied in all directions of the model, and 25 ps relaxation calculations were performed at 300 K in the NPT ensemble. Subsequently, a strain rate of 0.001/ps was applied in the *x*-axis direction, and tensile calculations were performed. In this case, the vertical stresses along the *y*- and *z*-axes were maintained at a constant value of 0 Pa using the NPT ensemble. The same calculations were performed in the *y*- and *z*-directions, and the average Young's modulus was obtained.

Fig. 3 shows an indentation model that assumes shear processing. In this calculation, the tip of the tool used for shear processing was assumed to be a cylindrical virtual indenter, and deformations due to compressive forces from the punch were reproduced by pushing the indenter into the amorphous alloy. The AUM was stacked $8 \times 1 \times 4$ times in the *x*-, *y*-, and *z*-directions, respectively, and the constructed piled-up amorphous model (PAM), consisting of 216,000 atoms in total, was used for subsequent calculations. As shown in Fig. 3, periodic boundary conditions were applied to the PAM in the *x*- and *y*-directions, and a bottom thickness of 5 Å was fixed in the *z*-direction. The virtual cylindrical indenter was also placed parallel to the *xy*-plane. This virtual indenter provided a repulsive force of $F(r) = -K\,(r - R)^2$ to the atoms in contact with it, where *K* is the specified force constant, *r* is the distance from the atom to the center of the indenter, *R* is the radius of the indenter, and $F(r) = 0$ for $r > R$. The specified force constant was set to 1.0, the indenter radius was set to 100 Å, and the virtual indenter was pushed in the − *z*-direction of the model at a velocity of 10 m/s.

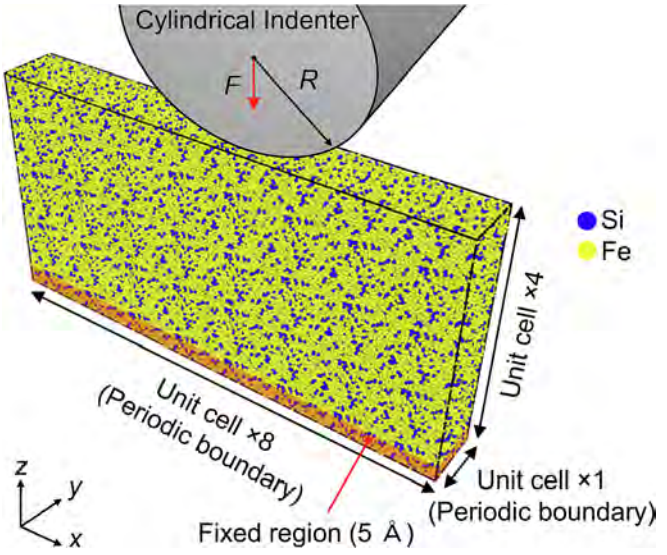

Fig. 3. Schematic of indentation model using piled-up amorphous model (PAM). PAM consisted of 216,000 atoms and was constructed by stacking the amorphous alloy unit cell model (AUM) $8 \times 1 \times 4$ times in the *x*-, *y*-, and *z*-directions. A virtual indenter with a radius of 100 Å was pushed in the − z-direction of the PAM at a velocity of 10 m/s.

3. Results and discussion

3.1. Evaluation of potential energy, volume, atomic packing factor, and mechanical properties of AUM with different cooling rates

Fig. 4 shows the change in potential energy per unit atom during the cooling of the $Fe_{85}Si_{15}$ BUM from the molten state at 3000 K to 300 K at cooling rates of 10^{10} K/s and 10^{12} K/s. It can be observed that for both cooling rates, the slope of the potential energy changed at approximately 900 K. This indicates that the $Fe_{85}Si_{15}$ AUM formed by the rapid cooling of the $Fe_{85}Si_{15}$ BUM undergoes a glass transition at a cooling temperature of approximately 900 K. Furthermore, a comparison of the potential energies of the two models shows that the model constructed using a slower cooling rate of 10^{10} K/s has a slightly lower potential energy than that of the model cooled at 10^{12} K/s. The difference in the potential energies at 300 K was evaluated to be only 0.2 %.

Table 1 shows the volumes and APFs of the $Fe_{85}Si_{15}$ AUMs prepared using different cooling rates. The atomic radii of Fe and Si used in the volume and APF calculations were 1.26 Å and 1.18 Å, respectively, and the total number of atoms in each model was 6750. It can be observed that for the same composition ratio, the model constructed using a slower cooling rate has a smaller volume and higher APF by

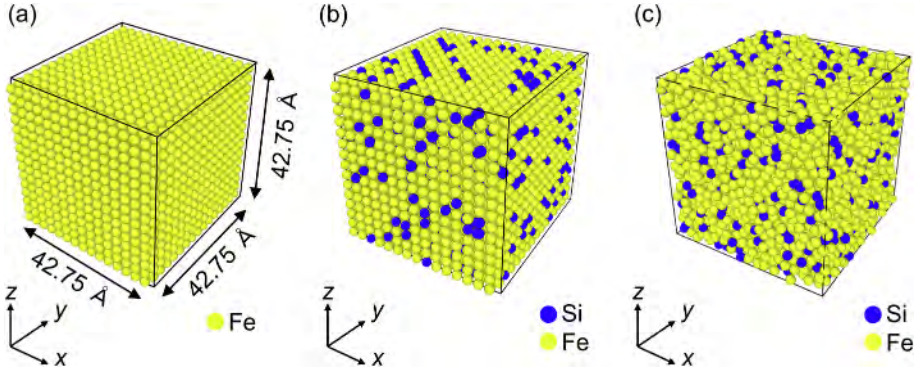

Fig. 2. Unit cell models with each side length of 42.75 Å, consisting of 6750 atoms of (a) Fe BCC structure (Fe BUM), (b) Fe_{85} Si_{15} BCC structure (Fe_{85} Si_{15} BUM), and (c) Fe_{85} Si_{15} amorphous structure (Fe_{85} Si_{15} AUM) constructed using a cooling rate of 10^{10} K/s.

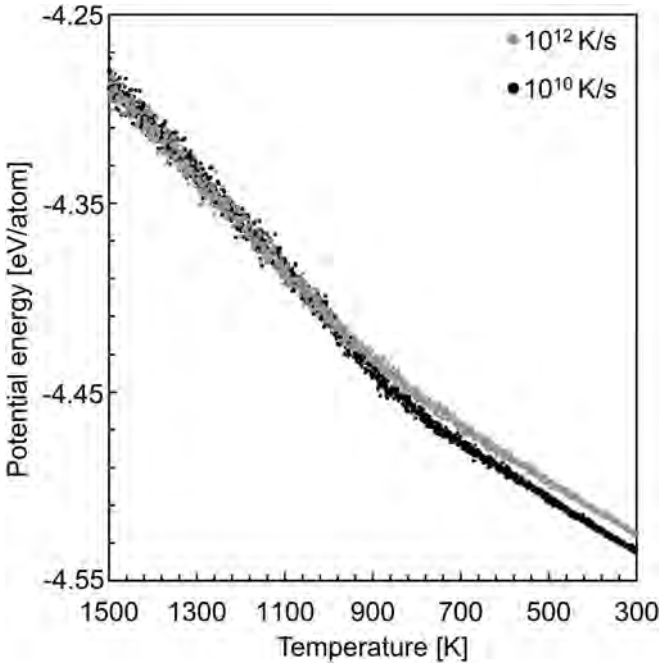

Fig. 4. Potential energy per unit atom during quenching at cooling rates of 10^{10} K/s and 10^{12} K/s for Fe_{85} Si_{15} amorphous models.

Table 1
Volumes and atomic packing factors (APF) of two Fe_{85} Si_{15} AUMs prepared using different cooling rates: 10^{10} K/s and 10^{12} K/s.

Composition	$Fe_{85}Si_{15}$	
Cooling rate [K/s]	10^{10}	10^{12}
Volume [Å^3]	79,654	79,783
Atomic packing factor [%]	69.10	68.99

approximately 0.1 %. Hence, the model built using a slower cooling rate exhibited a more closely packed structure, although only slightly, compared with those exhibited by the model cooled at a faster cooling rate. This is attributed to the longer cooling time, which allowed more time for the atoms to move to stable positions.

Fig. 5 shows the stress–strain diagrams obtained from tensile calculations in the *x*-axis direction for the Fe BUM and $Fe_{85}Si_{15}$ AUM built using different cooling rates. In Fig. 5(a), *E* and σ denote the average values of Young's modulus and tensile strength obtained from tensile calculations on the Fe BUM in the *x*-, *y*-, and *z*-axis directions. In Fig. 5 (b), E10 and σ_{10}, and E_{12} and σ_{12} denote the average values of Young's modulus and tensile strength in the *x*-, *y*-, and *z*-axis directions obtained from tensile calculations on the $Fe_{85}Si_{15}$ AUM built using cooling rates of 10^{10} K/s and 10^{12} K/s, respectively. As shown in Fig. 5(a), the Young's modulus and tensile strength of the reference Fe BUM are 103.5 GPa and 3.2 GPa, respectively. For comparison, Hitomi et al. [47] performed tensile calculations for a BCC crystal model of Fe using MD and found that the Young's modulus in the [001] direction is 108.9 GPa at 300 K, with which the Young's modulus indicated in Fig. 5(a) is in good agreement. As shown in Fig. 5(b), the strength and Young's modulus of the $Fe_{85}Si_{15}$ AUM built using the slower cooling rate of 10^{10} K/s are 4.3 GPa and 90.7 GPa, respectively, whereas those of the $Fe_{85}Si_{15}$ AUM built using the faster cooling rate of 10^{12} K/s are 3.7 GPa and 80.6 GPa, respectively. It has been reported that Young's modulus of Metglas, commercial Fe-based amorphous alloys, are approximately 80 GPa to 150 GPa [48], showing values similar to that of the AUM constructed using the present calculation. Furthermore, Jin et al. [49] indicated a similar trend to our calculation, that Fe–Si-based amorphous ribbon

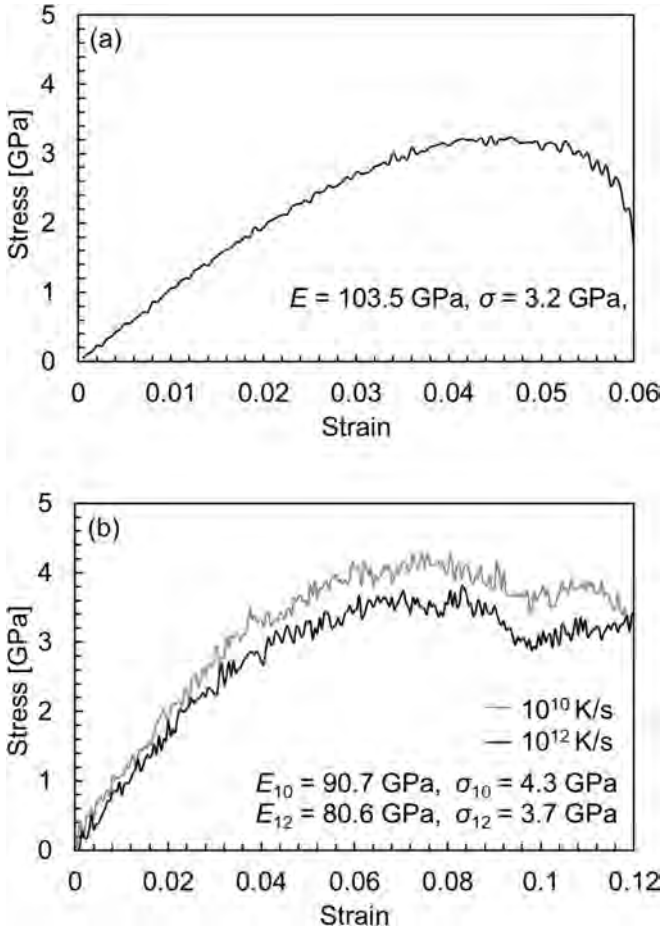

Fig. 5. Stress–strain curves of (a) Fe BCC unit cell model (BUM), (b) Fe_{85} Si_{15} amorphous unit cell models (AUMs) built using different cooling rates: 10^{10} K/s and 10^{12} K/s. The Young's modulus *E* and tensile strength σ of BUM (*E*, σ) and AUMs built at slower (E_{10} , σ_{10}) and faster (E_{12} , σ_{12}) cooling rates were (*E*, σ) = (103.5 GPa, 3.2 GPa), (E_{10} , σ_{10}) = (90.7 GPa, 4.3 GPa), (E_{12} , σ_{12}) = (80.6 GPa, 3.7 GPa).

fabricated at a slower cooling rate showed a higher Young's modulus and tensile strength than that of a faster cooling rate one by experiments. With regard to the tensile strengths of the Fe BUM and $Fe_{85}Si_{15}$ AUM, those of the AUMs for both cooling rates are higher than that of the Fe BUM, indicating that the $Fe_{85}Si_{15}$ AUM constructed in this study reproduces the high-strength properties of amorphous alloys. A decrease in potential energy and an increase in APF, thus, a decrease in free volume [50], leads to an increase in tensile strength [51]. Although there are only slight differences of 0.2 % in the potential energy and 0.1 % in the APF at 300 K between the $Fe_{85}Si_{15}$ AUMs prepared using different cooling rates, the tensile strength and Young's modulus differ by as much as 14 % and 11 %, respectively. This suggests that apart from the potential energy and APF, a specific atomic structure may have contributed to the change in mechanical strength. Therefore, we decided to investigate the SRO, a local structural feature, to clarify why the atomic structure produces large differences in mechanical properties.

3.2. Investigation on SRO of non-deformed amorphous model structure by Voronoi analysis

Although amorphous alloys do not have long-range ordered structures like those in crystalline metals, they have SROs owing to their ability to form closely packed structures [52]. In particular, the icosahedral SRO structure consisting of 13 atoms, which increases rapidly at the glass transition temperature, is a characteristic SRO of amorphous

alloys [53–55]. Such SROs can be analyzed using Voronoi analysis [56], which uses a polyhedron (Voronoi polyhedron: VP) composed of an arbitrary central atom and bisecting planes of surrounding atoms. VPs of crystalline or amorphous structures are generally formed by triangular to hexagonal faces. Therefore, the VPs are expressed using a notation method called the Voronoi index (n_i), in which the number of hexagonal faces from triangular to hexagonal is listed as $< n_3, n_4, n_5, n_6 >$, where n_i is the number of i-angular faces constituting the VP. For example, a fully icosahedral structure is expressed as $< 0,0,12,0 >$, whereas a BCC crystal structure is expressed as $< 0,6,0,8 >$. Because the sum of the Voronoi indices n_i represents the total number of atoms located adjacent to the central atom, this sum is defined as a simplified coordination number (CN).

Fig. 6 shows the results of the Voronoi analysis for the $Fe_{85}Si_{15}$ AUM, which consists of 6750 atoms in total, and lists its top 10 VPs. Fig. 6(a) and Fig. 6(b) show the Si-centered and Fe-centered VPs of the $Fe_{85}Si_{15}$ AUM fabricated using the faster cooling rate of 10^{12} K/s, and Fig. 6(c) and Fig. 6(d) show the Si-centered and Fe-centered VPs of the $Fe_{85}Si_{15}$ AUM fabricated using the slower cooling rate of 10^{10} K/s. The results show that for both cooling rates, $<0,3,6,4>$ is especially rich in Si-centered VPs and $< 0,2,8,4 >$ and $< 0,1,10,2 >$ in Fe-centered VPs, indicating that these VPs are easily formed during the rapid cooling step in the fabrication of Fe–Si binary amorphous alloys. For comparison, Pan et al. used MD to calculate how the SRO of Fe at a high-temperature liquid state transforms its atomic structure during the cooling process to form solid BCC-Fe and investigated the transformation process of SRO from liquid Fe to solid BCC-Fe using Voronoi analysis [57]. Their findings revealed that the top three VPs present in Fe in a high-temperature liquid state are $< 0,3,6,4>$, $<0,1,10,2>$, and $< 0,2,8,4>$, and that $< 0,3,6,4 >$ in particular plays an important role in the crystallization process [57]. These three VPs are abundant in our $Fe_{85}Si_{15}$ AUM, as shown in Fig. 6, indicating that the SRO of the $Fe_{85}Si_{15}$ AUM built using rapid cooling is similar to that of Fe in the high-temperature liquid state. Furthermore, the high fraction of VPs (indicated by black bars) is consistent with the occurrence of intermediate VPs during the transformation of VPs from Fe in a high-temperature liquid state to solid BCC-Fe by rapid quenching. Pan et al. showed that during crystallization by cooling from a high-temperature liquid state, VPs existing in the liquid state transform into BCC structures through various intermediate structures [57]. Because crystallization or amorphization depends on the cooling rate upon cooling from the high-temperature liquid state, it was considered in this present study that slight differences in the atomic structure due to differences in cooling rates might appear in the intermediate structures. Therefore, based on the deformation path of VPs from the high-temperature liquid state of Fe to BCC-Fe, as derived by Pan et al., the deformation path is inferred and shown in Fig. 7, for which only the VPs that appeared in the present analysis were extracted. It is known that melting occurs along with crystallization; therefore the VP deformation paths that occur during crystallization, melting, and without crystallization and melting have been identified, as indicated by black, gray dotted, and black dotted arrows, respectively [58]. The deformation paths are divided into layers from Layers 1 to 5. The characteristic structure of amorphous alloys, which is the fully icosahedral VP $< 0,1,12,0 >$ and the distorted icosahedral VPs $< 0,1,10,x>$ (x = 2, 3), $<0,2,8,x>$ (x = 2,4), are labeled as "amorphous-like structure," VPs $< 0,3,6,x>$ (x = 3–5) are labeled as "intermediate structure," and distorted BCC VP $< 0,4,4,6 >$ as a "BCC-like structure" [58]. We will use this classification to investigate SROs in the subsequent parts of the study.

Afterward, we investigated how the fractions of the VPs in the $Fe_{85}Si_{15}$ AUM, as shown in Fig. 7, for the different cooling rates vary with the central atomic species. Fig. 8 shows the fractions of the VPs in the $Fe_{85}Si_{15}$ AUM with respect to the CN for (a) 10^{12} K/s (faster cooling rate) and (b) 10^{10} K/s (slower cooling rate). The black and gray bars indicate the fractions of Si-centered and Fe-centered VPs, respectively. It

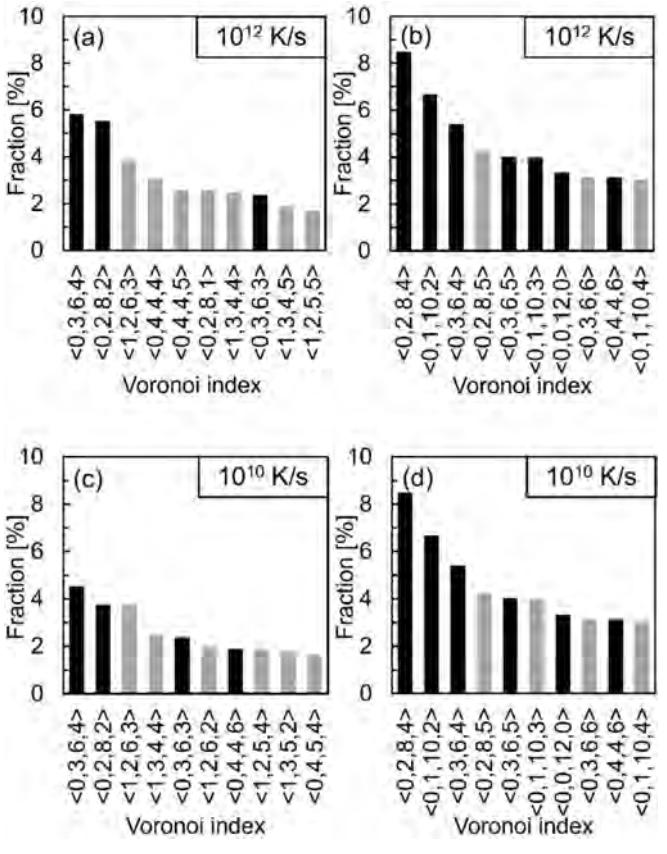

Fig. 6. Top ten Voronoi polyhedrons (VPs) of Fe_{85} Si_{15} AUMs built using different cooling rates: (a) and (b) Si-centered and Fe-centered VPs, respectively, of Fe_{85} Si_{15} AUM built using a cooling rate of 10^{12} K/s; (c) and (d) Si-centered and Fe-centered VPs, respectively, of Fe_{85} Si_{15} AUM built using a cooling rate of 10^{10} K/s. The black bar graph shows the main intermediate VPs that appear in the process of liquid Fe changing to solid BCC-Fe through rapid cooling [57].

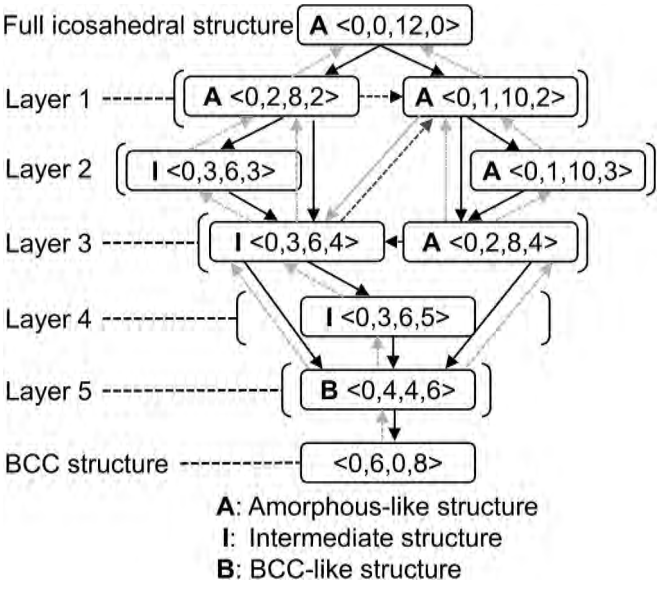

Fig. 7. Selected crystallization pathways from fully icosahedral SRO to BCC SRO, as proposed by Pan et al [57]. Black arrows indicate crystallization, dotted gray arrows denote melting, and dotted black arrows signify transformation without crystallization and melting. A, I, and B indicate amorphous-like, intermediate, and BCC-like structures, respectively [58].

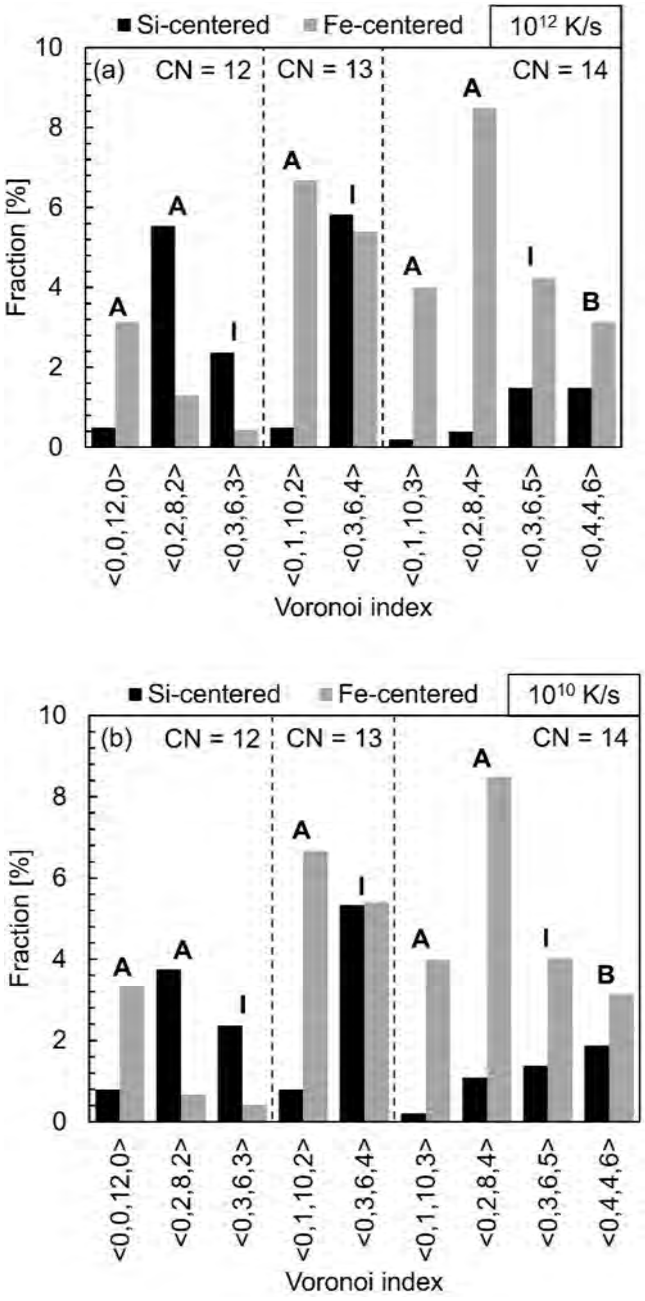

Fig. 8. Fractions of Voronoi polyhedra sorted by coordination number (CN) of initial amorphous structure for different cooling rates; (a) Fe_{85} Si_{15} AUM built using a cooling rate of 10^{12} K/s and (b) Fe_{85} Si_{15} AUM built using a cooling rate of 10^{10} K/s. **A**, **I**, and **B** indicate amorphous-like, intermediate, and BCC-like structures, respectively.

can be observed that in both models, the Si- and Fe-centered VPs are distributed on the low- and high-CN sides, respectively. From a comparison of the stable crystal structures of each atom, it can be inferred that Si tends to form covalent crystals with a diamond structure (CN = 4) and that the CN tends to be relatively small. By contrast, Fe tends to form a closely packed structure via metallic bonding, forming BCC crystals (CN = 8) and face-centered cubic (FCC) crystals (CN = 12), resulting in a relatively large CN. Even during the quenching process, each atom attempts to form an energetically stable atomic structure. The difference in the CNs owing to the difference in the central atomic species confirms that the present simulation reproduces the covalent bonding nature of Si and the metallic bonding nature of Fe. The transformation paths from Layer 1 to Layer 3 in Fig. 7 are divided into two: polyhedra < 0,2,8,2>, <0,3,6,3>, and < 0,3,6,4 > on the low-CN side and polyhedra < 0,1,10,2>, <0,1,10,3>, and < 0,2,8,4 > on the high-CN side. Fig. 8 shows that in the $Fe_{85}Si_{15}$ AUMs prepared using cooling rates of 10^{12} K/s and 10^{10} K/s, the total percentages of the VP groups on the low-CN side are 13.7 % and 11.5 %, respectively, for the Si-centered VPs and 7.1 % and 6.5 %, respectively, for the Fe-centered VPs. Similarly, the total percentages of the VP groups on the high-CN side are 1.1 % and 2.1 %, respectively, for the Si-centered VPs, and 19.2 % for both cooling rates for the Fe-centered VPs. This finding indicates that in Layers 1 through 3 shown in Fig. 7, Si-centered VPs are more dominant in the low-CN paths, whereas Fe-centered VPs are more dominant in the high-CN paths.

Based on the results shown in Fig. 8, the percentages of VPs of (i) amorphous-like structure (<0,0,12,0>, <0,2,8,*x*>, <0,1,10,*x* >), (ii) intermediate structure (<0,3,6,*x* >), and (iii) BCC-like structure (<0,4,4,6 >) in the constructed $Fe_{85}Si_{15}$ AUM model were then summed up. Aforementioned percentages of (i)–(iii) of Si-centered and Fe-centered VPs in the $Fe_{85}Si_{15}$ AUMs built using a cooling rate of 10^{12} K/s, as shown in Fig. 8(a), are (i) 6.6 %, (ii) 9.7 %, and (iii) 1.5 %, and (i) 20.4 %, (ii) 10.1 %, and (iii) 3.1 %, respectively, whereas those in the $Fe_{85}Si_{15}$ AUM built using a cooling rate of 10^{10} K/s, as shown in Fig. 8 (b), are (i) 5.8 %, (ii) 9.1 %, and (iii) 1.9 %, and (i) 19.8 %, (ii) 9.8 %, and (iii) 3.1 %, respectively. In other words, for both VPs of the central elements, the model in Fig. 8(a) built using the faster cooling rate of 10^{12} K/s has more amorphous-like and intermediate structures, whereas the model in Fig. 8(b) built using the slower cooling rate of 10^{10} K/s has more BCC-like structures. As shown in Table 2, although the fraction of total icosahedral structure is higher in the $Fe_{85}Si_{15}$ AUM created at a faster cooling rate of 10^{12} K/s than that of a slower cooling rate of 10^{10} K/s, the fraction of fully icosahedral structure is lower, with a higher fraction of distorted icosahedral structure. The same trend is observed in Fe–Si-based amorphous alloys [59] using the same interatomic potential as our research. Other reports [60] have shown that early yielding and less stiffness occur when the full icosahedral structure is few. This fraction difference between full and distorted icosahedral structures is a factor that caused the difference in Young's modulus and tensile strength in Fig. 5.

In addition, depending on the cooling rate, the change in the fraction of Si-centered VPs was larger than that of Fe-centered VPs. Therefore, it is clear that slight differences in the atomic structure owing to differences in the cooling rate are more likely to appear in Si-centered VPs than in Fe-centered VPs. Focusing on the Si-centered VPs, Fig. 8(a) shows that the fractions of < 0,2,8,2> (amorphous-like structure) and < 0,3,6,4> (intermediate structure) increase for the model built using a faster cooling rate, whereas Fig. 8(b) shows that the fractions of < 0,1,10,2 > and < 0,2,8,4> (amorphous-like structure), and < 0,4,4,6> (BCC-like structure) increase for the model built using a slower cooling rate. In particular, the characteristic fully icosahedral structure of amorphous alloys, i.e., <0,0,12,0>, and distorted icosahedral structures, i.e., <0,2,8,*x* > and < 0,1,10,*x*>, formed 7 % more in the $Fe_{85}Si_{15}$ AUM fabricated using the faster cooling rate than in the $Fe_{85}Si_{15}$ AUM constructed using the slower cooling rate. Intermediate structures, <0,3,6,*x*>, also formed 7 % more in the faster cooling rate AUM. This result indicates that the $Fe_{85}Si_{15}$ AUM built using a faster cooling rate is more likely to form amorphous-like and intermediate structures during the cooling process because of the low-CN transformation (Fig. 7, Layers 1–3, left path), in which Si-centered VPs are more abundant. Conversely, the AUM fabricated using a slower cooling rate is inferred to transform into Layer 5 through a high-CN deformation path (Fig. 7, Layers 1–3, right path), which has a large fraction of Fe-centered VPs, and thus is more likely to create a BCC-like structure. Therefore, it can be said that for both models, regardless of the cooling rate, the SROs are amorphous structures; however, those built using a slower cooling rate have more SROs that are closer to the crystalline structure.

Table 2
Fraction of icosahedral structure of two Fe_{85} Si_{15} AUMs prepared using different cooling rates; 10^{10} K/s and 10^{12} K/s.

Cooling rate [K/s]	10^{12}		10^{10}	
Type of central atom in VP	Fe	Si	Fe	Si
Total icosahedral VP fraction [%]	23.6	7.1	23.1	6.6
Full icosahedral VP fraction [%]	3.1	0.5	3.3	0.8
Distorted icosahedral VP fraction [%]	20.4	6.6	19.8	5.8

3.3. Investigation of mechanical strength by indentation calculation and SRO investigation by Voronoi analysis in deformation region

To investigate how the SROs of amorphous alloys are affected by shear deformation due to external forces, indentation calculations were performed on PAMs constructed using different cooling rates. First, the indentation calculations were performed to investigate the mechanical strengths of the PAMs under compressive deformation. Fig. 9 shows the relationship between the applied force in the indentation direction (z-axis direction) and the indentation depth d_i for the PAMs constructed using different cooling rates. It can be observed that in both models, elastic deformation occurs up to d_i = 25 Å, and plastic deformation occurs above d_i. The yield forces (F_{yield}) for the models built using the slower cooling rate of 10^{10} K/s and faster cooling rate of 10^{12} K/s were 237 GN and 213 GN, respectively. Similar to the tensile calculations in Fig. 5, the indentation calculations also revealed a higher strength for the model fabricated using a cooling rate of 10^{10} K/s, indicating that strength changes occur for both tensile and compressive deformation. Because the deformation of amorphous alloys proceeds through a series of local plastic deformations connected to generate SBs [61], differences in the structure within the SBs are thought to influence the changes in the mechanical properties. Therefore, to clarify the cause of the large strength difference despite the small differences in energy and APF, the SRO in the sheared region generated by the indentation was investigated. Note that PAM at d_i = 30 Å was used to investigate the SRO in the sheared region, because it is considered to have undergone sufficient plastic deformation. Atoms with shear strain (ε_{ss}) greater than 0.1 were used to evaluate the SRO.

Fig. 10 shows the results of classifying all VPs (Si-centered VPs + Fe-centered VPs) in the model by the layers defined in Fig. 7 for the pre-indentation structure and sheared region structure created by indentation. Fig. 10(a) and Fig. 10(b) show the Voronoi analysis results for the PAM fabricated using the faster cooling rate of 10^{12} K/s and slower cooling rate of 10^{10} K/s, respectively. The notation is as follows: L1 is an abbreviation for Layer 1; the other layers are similarly labeled. The full icosahedral structure < 0,1,12,0 > and distorted icosahedral structures < 0,1,10,x>, <0,2,8,x > are categorized as amorphous-like structures, <0,3,6,x > as intermediate structures, and < 0,4,4,6 > as BCC-like structures. The black bars show the fractions of VPs before indentation, whereas the gray bars show those of VPs in the sheared region after indentation. It can be observed that for both cooling rates, the fully icosahedral VP, <0,0,12,0>, which is characteristic of amorphous structures, decreased in the sheared region. Furthermore, along the Layers 1–3 pathway shown in Fig. 7, the fraction of Fe-centered VPs, i.e.,

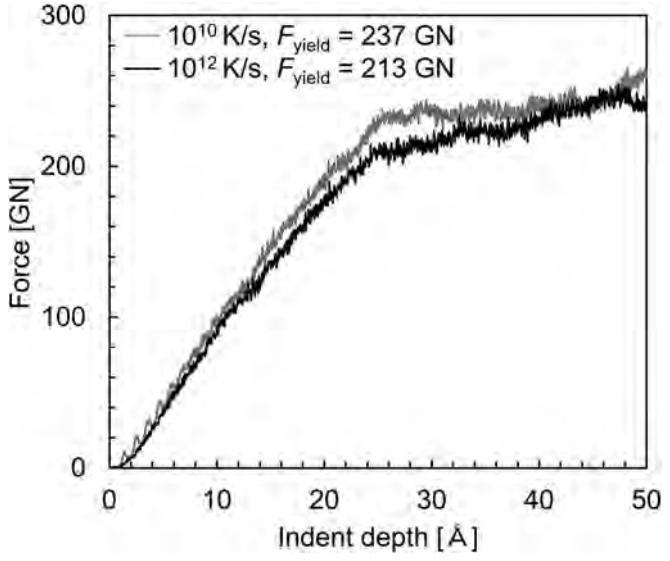

Fig. 9. Force–indentation depth curves of models with different cooling rates.

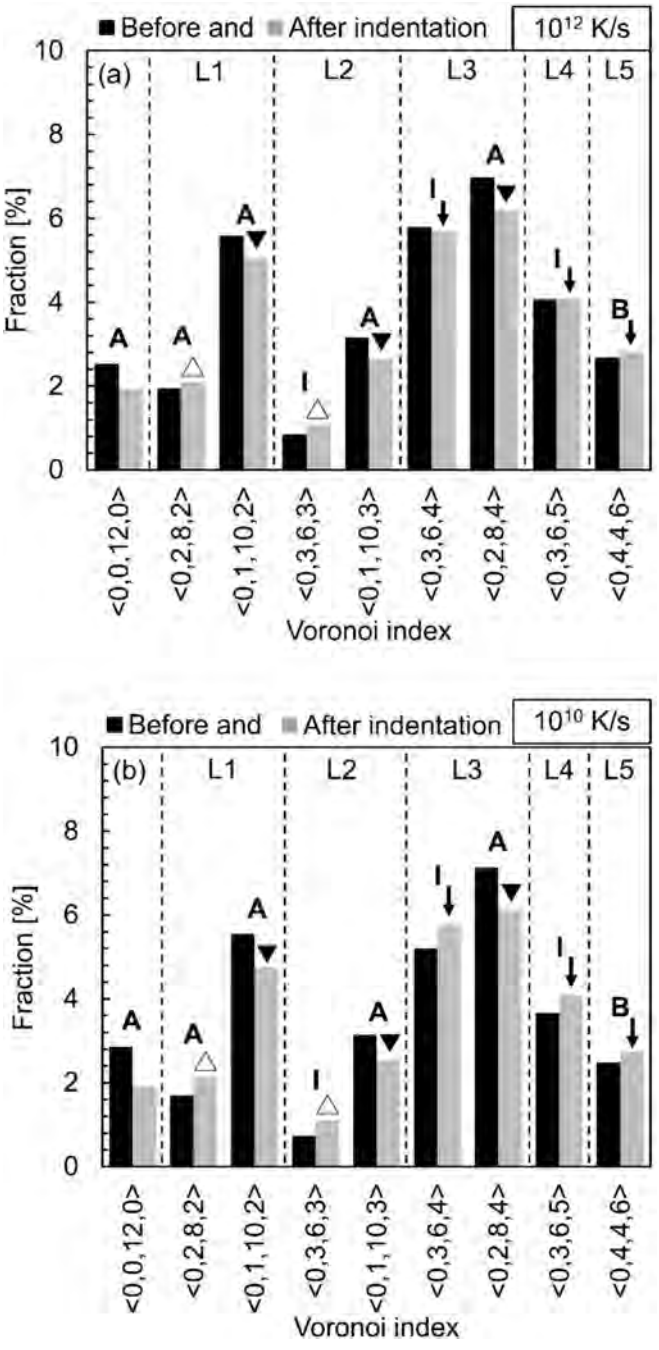

Fig. 10. Fractions of Voronoi polyhedra of Layers 1–5 for models with different cooling rates; (a) Fe_{85} Si_{15} PAM built using a cooling rate of 10^{12} K/s and (b) Fe_{85} Si_{15} PAM built using a cooling rate of 10^{10} K/s. Notation: L1 indicates Layer 1; other layers are similarly labeled, and **A**, **I**, and **B** indicate amorphous-like, intermediate, and BCC-like structures, respectively.

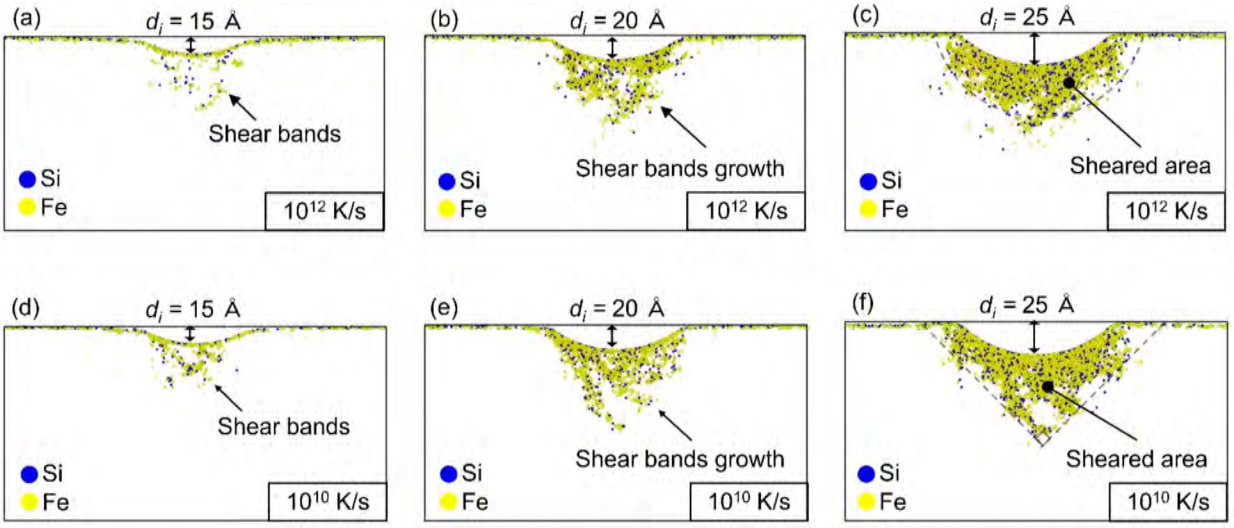

Fig. 11. Elongation behaviors of SBs in $Fe_{85}Si_{15}$ PAMs built using different cooling rates when the indent depth d_i = 15, 20, and 25 Å; (a)–(c) PAMs built using a cooling rate of 10^{12} K/s and (d)–(f) PAMs built using a cooling rate of 10^{10} K/s.

<0,1,10,2>, <0,1,10,3>, and < 0,2,8,4>, in the sheared region decreased (black-filled inverse triangles in Fig. 10), whereas the fraction of Si-centered VPs, i.e., <0,2, 8,2 > and < 0,3,6,3>, in the sheared region on the low-CN side increased (white-filled triangles in Fig. 10). This indicates that < 0,0,12,0>, which is a fully icosahedral SRO existing in the pre-indentation structure, is deformed in the shear region through the Layers 1–3 paths where the Si-centered VPs are abundant. Here, we focus on, as indicated by the arrows in the figure, <0,3,6,4 > in Layer 3, and < 0,3,6,5 > in Layer 4, which are the intermediate structures, and < 0,4,4,6 > in Layer 5, which are BCC-like structures. The model in Fig. 10 (a) built using the faster cooling rate exhibits a decrease in intermediate structures by 1 % and an increase in BCC-like structures by 6 % in the sheared region. Whereas the model in Fig. 10(b) built using the slower cooling rate exhibits an increase in intermediate structures by 11 % and an increase in BCC-like structures by 11 % in the sheared region. These results indicate that the deformation of the amorphous structure in the sheared region of the model built using the faster cooling rate is limited to the path from Layers 1 to 3, whereas in the model built using the slower cooling rate, the deformation proceeds to Layer 5, and the structure in the sheared region changes to a BCC-like structure. It is known that icosahedral structures in amorphous alloys hinder the formation of long-period regular structures such as crystals [62]. The < 0,3,6,4 > in Layer 3, which is the starting point for the change into the BCC-like structure, is formed mostly by deformation from < 0,2,8,2 > and < 0,1,10,2>, with the extra atoms entering the central atoms of the < 0,2,8,2 > or the interatomic distances of < 0,1,10,2 > decreasing [57]. Furthermore, <0,3,6,4 > changes to a BCC-like structure when extra atoms are introduced into the central atoms of the polyhedra [57]. Therefore, the Si-centered icosahedral structure (Fig. 8), which is abundant in the model constructed using the faster cooling rate, hinders the migration of atoms and suppresses their transformation into a BCC-like structure. By contrast, the slower-cooling-rate model has fewer icosahedral structures that hinder the migration of atoms, and more VPs are converted into BCC-like structures in the sheared region owing to compressive forces during indentation.

3.4. Investigation of SB elongation behavior affecting shear machining quality

This section elucidates the effects of the slight structural differences between the two models with different cooling rates, as presented in Sections 3.1 to 3.3, on the formation of the broken face due to crack propagation from the tool tip in shear processing, by visualizing the propagation behaviors of the SBs generated by the indentation. Based on the results of the indentation calculations shown in Fig. 9, the SBs generated in the elastic range of $d_i \leq 25$ Å, where the deformation is considered to have progressed linearly, were selected for investigation. The atoms with $\varepsilon_{ss} \geq 0.5$ were evaluated as SBs, assuming that the atoms under strong shear strain are the center of the SBs.

Fig. 11 (a)–(c) show atoms with $\varepsilon_{ss} \geq 0.5$ at d_i = 15 Å, 20 Å, and 25 Å for PAMs built using a cooling rate of 10^{12} K/s, whereas Fig. 11(d)–(f) show atoms with $\varepsilon_{ss} \geq 0.5$ at d_i = 15 Å, 20 Å, and 25 Å for PAMs built using a cooling rate of 10^{10} K/s. For both cooling rates, the SBs were generated at approximately 45° from the tool contact surface to the indentation direction at d_i = 15 Å (Fig. 11(a) and Fig. 11(d)). At d_i = 20 Å (Fig. 11(b) and Fig. 11(e)), the generated SBs propagated and grew into larger SBs. This is consistent with the findings of past research studies involving uniaxial uniform loading tests on amorphous alloys using MD techniques, in which the formation of multiple SBs and SBs in the direction of 40°–45° under compression have been observed [61]. The present results indicate that the SBs propagated in a direction of approximately 45°, as in past studies, even when the load was concentrated at a single point. To compare the SB propagation behaviors of models with different cooling rates, we compared the SBs at d_i = 25 Å in Fig. 11(c) and Fig. 11(f), where a wide range of shear strain was observed. As shown in Fig. 11(c), the model built using a cooling rate of 10^{12} K/s exhibited isotropic SB growth from the entire tool contact surface (within the dotted semicircle), whereas as shown in Fig. 11(f), the SB extended around an isosceles triangle (within the dotted triangle), with one side at approximately 45° with the tool contact surface as the base. The reason for the directional growth of SBs in the model fabricated using a cooling rate of 10^{10} K/s is thought to be the lower number of Si-centered SROs, which are typical of amorphous structures, in the pre-indentation structure (Fig. 8) and the easy formation of SROs with BCC-like structures, which are close to crystalline structures, in the SBs (Fig. 10). Furthermore, various scholars have studied the relationship between SRO and deformation behavior in amorphous alloys by MD simulation. Kbirou et al. [58] showed that < 0,3,6,4 > and < 0,3,6,5 > VPs are precursor structures for crystallization induced by stress. Guder et al. [63] demonstrated that < 0,3,6,4 > and < 0,4,4,6 > VPs represent nucleation of crystalline order and that crystalline-like order is caused by chemical affinity between atoms. Mishra et al. [64] indicated that < 0,2,8,2 > and < 0,3,6,4 > VPs have liquid-like properties and therefore promote collective shear deformation and plastic deformation under load. Table 3 shows the increase/decrease ratio after indentation calculated from the results in Fig. 10 for the VPs listed above. Evidently,

Table 3
Ratio of VPs increase/decrease after indentation calculations.

Cooling rate	<0,2,8,2>	<0,3,6,4>	<0,3,6,5>	<0,4,4,6>
10^{12} K/s	7 %	−2 %	0 %	6 %
10^{10} K/s	26 %	11 %	11 %	11 %

all the VP groups increased in models created at a slow cooling rate. Therefore, the VPs formed within the shear band induced by the indentation stress induced a crystalline order, causing collective plastic deformation. This collective deformation acted like the {011} slip plane of the BCC crystal, giving directionality to the shear band development. This is thought to have led to the progression of ordered deformation, similar to dislocations in crystalline metals. It has been reported that during shear processing, high-quality broken faces can be obtained by controlling the direction of initial crack propagation [14]. Therefore, the model fabricated using the slower cooling rate, as shown in Fig. 11(d–f), in which the SB propagates directionally in the cutting direction of the plate, is a more suitable structure for shear processing

The aforementioned discussion indicates that in the model built using the slower cooling rate of 10^{10} K/s, the SBs, which are the cause of cracking in the early stages of shear processing, develop toward the cutting direction. The previous sections have shown that in the model built using the slower cooling rate of 10^{10} K/s, the number of SROs in the SBs generated by compressive forces that deform into intermediate and BCC-like structures is greater than that for 10^{12} K/s. Therefore, in processing methods such as shear processing, where crack propagation is caused by compressive forces from a tool, a smooth broken face can be obtained for the model built using the slower cooling rate of 10^{10} K/s. This is because in this model, the sheared region, which is the source of cracks, propagates while forming an ordered structure resembling a crystalline structure. If these results are applied to actual experiments, it is predicted that in specimens that have been structurally relaxed by heat treatment below the crystallization temperature, crystallization-like deformation is promoted by changes in the SROs inside the SBs that occur during shear processing. This suggests that heat treatment of amorphous alloys below the crystallization temperature controls the direction of crack propagation during shear processing and contributes to improved machining quality.

4. Conclusions

In this study, two amorphous models were fabricated using different cooling rates to investigate the effects of slight differences in the energy and atomic structure on the mechanical properties and SB propagation behavior, which determines the shear processing quality. The results obtained are as follows:

(i) The $Fe_{85}Si_{15}$ amorphous model built using a cooling rate of 10^{10} K/s from 3000 K to 300 K had a potential energy 0.2 % lower and an atomic packing factor (APF) 0.1 % higher than those of the $Fe_{85}Si_{15}$ amorphous model built using a cooling rate of 10^{12} K/s from 3000 K to 300 K. The difference was only slight.

(ii) The total number of short-range ordered structures (SRO) of the icosahedral structure, which typically appears in amorphous structures, was lower in the amorphous model built using a cooling rate of 10^{10} K/s than in the model built using 10^{12} K/s. However, the fraction of fully icosahedral structures is higher, with a lower fraction of distorted icosahedral structures in the model built by a slower cooling rate.

(iii) The results of the SRO investigation on the sheared region generated by the indentation calculations show that in both the amorphous models built using cooling rates of 10^{10} K/s and 10^{12} K/s, the fully icosahedral SRO structure at 300 K is deformed to a Si-centered distorted icosahedral structure during shear deformation. However, it is only in the amorphous model built using the slower cooling rate that the deformation progresses further, and the SRO of the BCC-like structure increases by 11 % before and after the deformation.

(iv) Compared to the amorphous model built using the faster cooling rate, the amorphous model fabricated using the slower cooling rate had an 11 % higher Young's modulus and 14 % higher tensile strength owing to the significant difference in the SRO, as shown in (ii) and (iii), even though there was only a slight decrease in energy and increase in the APF.

(v) In the amorphous model built using the slower cooling rate, the SB propagation becomes directional owing to deformation while forming a BCC-like SRO in the sheared region generated by the indentation calculations. Therefore, in the amorphous model built using the slower cooling rate, the SB propagates toward the cutting direction, suggesting that high-quality surfaces can be obtained in shear processing, which uses crack propagation.

CRediT authorship contribution statement

Chieko Kuji: Writing – original draft, Visualization, Software, Methodology, Investigation, Funding acquisition, Formal analysis, Data curation, Conceptualization. **Narumasa Miyazaki:** Writing – review & editing, Validation, Software, Methodology, Investigation, Formal analysis. **Masayoshi Mizutani:** Writing – review & editing, Conceptualization. **Keita Shimada:** Writing – review & editing, Conceptualization. **Nobuki Ozawa:** Writing – review & editing, Validation, Software, Methodology, Investigation, Formal analysis. **Momoji Kubo:** Writing – review & editing, Resources, Methodology. **Tsunemoto Kuriyagawa:** Writing – review & editing, Supervision, Conceptualization.

Funding

Part of this work was supported by JSPS KAKENHI, grant number 23K13228.

Declaration of competing interest

The authors declare that they have no known competing financial interests or personal relationships that could have appeared to influence the work reported in this paper.

Data availability

Data will be made available on request.

References

[1] H. Shingu, R. Suzuki, K. Ishihara, Rapid quenching and metastable equilibria, J. Soc. Mater. Sci. Jpn. 33 (1984) 239–245.
[2] H. Shingu, K. Ishihara, Rapid solidification of metals, Tetsu-to-Hagané 69 (1983) 1087–1094.
[3] P. Duwez, Structure and properties of alloys rapidly quenched from the liquid state, Trans. Am. Soc. Met. 60 (1967) 607–633.
[4] T. Masumoto, History of amorphous metals and its significance, Mater. Jpn. 40 (2001) 925–928.
[5] T. Masumoto, H. Kimura, Tensile properties of amorphous iron-base alloy (Fe-P-C System), J. Jpn. Inst. Met. Mater. 39 (1975) 133–141.
[6] M. Naka, K. Hashimoto, T. Masumoto, Corrosion resistivity of amorphous iron alloys containing chromium, J. Jpn. Inst. Met. Mater. 38 (1974) 835–841.
[7] H. Fujimori, T. Masumoto, Y. Obi, M. Kikuchi, On the magnetization process in an iron-phosphorus-carbon amorphous ferromagnet, Jpn. J. Appl. Phys. 13 (1974) 1889–1890.
[8] Y. Yoshizawa, Development trend and outlook for soft magnetic materials, Mater. Jpn. 56 (2017) 186–189.
[9] Y. Enomoto, K. Soma, Development of the amorphous motor balancing both resource saving and energy saving, J. Soc. Mech. Eng. 117 (2014) 753–756.
[10] H. Amano, Y. Enomoto, M. Ito, H. Itabashi, S. Tanigawa, R. Masaki, Examination of applying amorphous rolled core to permanent magnet synchronous motors, IEEJ Trans. Ind. Appl. 130 (2010) 632–638.
[11] Y. Enomoto, Radial gap type motor using amorphous metal for iron core, IEEJ Trans. Ind. Appl. 139 (2019) 606–611.

[12] M. Wakamiya, Amorphous magnetic materials, J. Soc. Mater. Sci. Jpn. 42 (1993) 771–779.
[13] T. Maeda, Shear processing (outlook on pressing process), Trans. Jpn. Soc, Mech. Eng. 62 (1959) 1371–1373.
[14] M. Murakami, Shear processing techniques and their resulting sheared surfaces, Tetsu-to-Hagané 71 (1985) 27–33.
[15] E.V. Crane, What happens in shear processing metal, Machinery 30 (1927) 225.
[16] J. C. Mikkers, Paper for the meeting of the C.I.R.P. in Nottingham, September 1968.
[17] T. Nakagawa, K. Suzuki, K. Sakaue, Blanking of amorphous alloy metal foils, Seisan-Kenkyu 34 (1982) 243–246.
[18] C. Kuji, K. Takenaka, M. Mizutani, K. Shimada, T. Kuriyagawa, T.J. Konno, Crystallization behavior and machining properties of annealed Fe-Si-B-Cr amorphous alloys, J. Mater. Sci. 56 (2021) 16697–16711.
[19] C. Kuji, M. Mizutani, K. Shimada, K. Suzuki, H. Miura, T. Kuriyagawa, Evaluation of fracture properties of annealed Fe–Si–B–Cr amorphous alloys using micro-tensile tests and blanking machinability, Mater. Sci. Eng. A 848 (2022) 143483.
[20] C. Kuji, M. Mizutani, K. Takenaka, K. Shimada, T.J. Konno, A.T. Yokobori, T. Kuriyagawa, Relationship between blanking performance and microstructure of annealed Fe–Si–B–Cr amorphous alloy sheets, Precis. Eng. 82 (2023) 33–43.
[21] C. Kuji, M. Mizutani, K. Takenaka, K. Shimada, T.J. Konno, H. Soyama, T. Kuriyagawa, Effect of local heating by ultrashort pulsed laser on Fe–Si–B–Cr amorphous alloys and its influence on blanking machinability, Precis. Eng. 81 (2023) 135–144.
[22] A. Inoue, T. Masumoto, M. Kikuchi, T. Minemura, Effect of compositions on the crystallization of (Fe, Ni, Co)-Si-B amorphous alloys, Sci. Rep. Res. Inst. Tohoku Univ. Ser. A 27 (1979) 127–146.
[23] Y. Takahara, J. Tamenari, H. Matsuda, Compositional dependence of crystallization process in Fe-B-Si amorphous alloys, J. Jpn. Inst. Met. Mater. 58 (1994) 245–251.
[24] Y. Takahara, K. Hatade, H. Matsuda, Structural relaxation and crystallization of amorphous $Fe_{79}B_{16}Si_5$, J. Jpn. Inst. Met. Mater. 51 (1987) 95–101.
[25] Y. Takahara, N. Fujii, H. Matsuda, Reversible changes in electrical resistivity and Mössbauer spectroscopy in structural relaxation of amorphous Fe-B-Si alloys, J. Jpn. Inst. Met. Mater. 52 (1988) 1–7.
[26] Y. Takahara, N. Narita, Local atomic structure in an Fe-B-Si amorphous alloy and its relaxation upon annealing, J. Jpn. Inst. Met. Mater. 63 (1999) 557–560.
[27] M. Oguni, Thermal studies on structural relaxation and ordering in disordered molecular-arrangement systems, Netsu Sokutei 36 (2009) 2–9.
[28] Y.Q. Cheng, E. Ma, Atomic-level structure and structure–property relationship in metallic glasses, Prog. Mater. Sci. 56 (2011) 379–473.
[29] H.R. Lashgari, C. Tang, D. Chu, S. Li, Molecular dynamics simulation of cyclic indentation in Fe-based amorphous alloy, Comput. Mater. Sci. 143 (2018) 473–479.
[30] A. Stukowski, Visualization and analysis of atomistic simulation data with OVITO–the Open Visualization Tool, Model. Simul. Mater. Sci. Eng. 18 (2009) 015012.
[31] H.R. Lashgari, J.M. Cadogan, C. Kong, C. Tang, C. Doherty, D. Chu, S. Li, Stress-relaxation heat treatment in FeSiBNb amorphous alloy: thermal, microstructure, nanomechanical and magnetic texture measurements, J. Magn. Mag. Mater. 456 (2018) 62–70.
[32] H.R. Lashgari, J.M. Cadogan, D. Chu, S. Li, The effect of heat treatment and cyclic loading on nanoindentation behaviour of FeSiB amorphous alloy, Mater. Des. 92 (2016) 919–931.
[33] H.R. Lashgari, Z. Chen, X.Z. Liao, D. Chu, M. Ferry, S. Li, Thermal stability, dynamic mechanical analysis and nanoindentation behavior of FeSiB(Cu) amorphous alloys, Mater. Sci. Eng. A 626 (2015) 480–499.
[34] K. Nakatani, A. Nakatani, H. Kitagawa, Y. Sugiyama, Molecular dynamics simulation on crack growth in amorphous metal, J. Soc. Mater. Sci. Jpn. 49 (2000) 275–281.
[35] K. Nakatani, A. Nakatani, H. Kitagawa, Molecular dynamics study on fracture mechanism of Fe-amorphous metal (J integral near mode I crack tip), in: H. Kitagawa, T. Aihara, Y. Kawazoe (Eds.), Mesoscopic Dynamics of Fracture, Springer-Verlag, Berlin, Heidelberg, 1998, pp. 88–98.
[36] K. Nakatani, H. Kitagawa, A. Nakatani, Molecular dynamics simulation of the local structure and internal stress of single-component amorphous metal, Trans. Jpn. Soc. Mech. Eng. A 62 (1996) 847–852.
[37] K. Nakatani, H. Kitagawa, A. Nakatani, Molecular dynamics simulation on the mechanical strength of one-component amorphous metal: decreasing of elastic moduli and strength induced by change of internal structure, J. Soc. Mater. Sci. Jpn. 46 (1997) 244–249.
[38] R. Matsumoto, M. Nakagaki, Mechanical property of amorphous metal with dispersed nanocrystalline particle: molecular dynamics study on crystal volume fraction and size effects, Trans. Jpn. Soc. Mech. Eng. A 72 (2006) 32–38.
[39] R. Matsumoto, M. Nakagaki, Mechanical properties of amorphous metal with dispersed nanocrystalline particles: molecular dynamics analysis on appearance of particle size effects, Trans. Jpn. Soc. Mech. Eng. A 72 (2006) 361–368.
[40] H. Ino, Possibilities of amorphous alloys, Seisan Kenkyu 32 (1980) 453–459.
[41] S. Plimpton, Fast parallel algorithms for short-range molecular dynamics, J. Comput. Phys. 117 (1995) 1–19.
[42] B. Jelinek, S. Groh, M.F. Horstemeyer, J. Houze, S.G. Kim, G.J. Wagner, A. Moitra, M.I. Baskes, Modified embedded atom method potential for Al, Si, Mg, Cu, and Fe alloys, Phys. Rev. B 85 (2012) 245102.
[43] M. Parrinello, A. Rahman, Crystal structure and pair potentials: a molecular-dynamics study, Phys. Rev. Lett. 45 (1980) 1196.
[44] M. Parrinello, A. Rahman, Polymorphic transitions in single crystals: a new molecular dynamics method, J. Appl. Phys. 52 (1981) 7182–7190.
[45] S. Nosé, A unified formulation of the constant temperature molecular dynamics methods, J. Chem. Phys. 81 (1984) 511–519.
[46] W.G. Hoover, Canonical dynamics: equilibrium phase-space distributions, Phys. Rev. A 31 (1985) 1695–1697.
[47] T. Hitomi, N. Morita, Y. Yoshida, Y. Suwa, A study on the evaluation of polycrystal pure iron's Young's modulus: simulations of uniaxial tension tests of elastic region using molecular dynamics, J. Jpn. Soc. Precis. Eng. 65 (1999) 1594–1599.
[48] L. Lanotte, C. Luponio, F. Porreca, Relaxation of young modulus by thermal treatment in metglas ribbons, Il Nuovo Cimento D 6 (1985) 468–478.
[49] C.B. Jin, Y.Z. Wu, J.N. Wang, F. Han, M.Y. Tan, F.C. Wang, J. Xu, J. Yi, M.C. Li, Y. Zhang, J.T. Huo, J.Q. Wang, M. Gao, Nanoscale viscoelastic transition from solid-like to liquid-like enables ductile deformation in Fe-based metallic glass, J. Mater. Sci. Technol. 194 (2024) 63–74.
[50] D. Turnbull, M.H. Cohen, Free-volume model of amorphous phase–glass transition, J. Chem. Phys. 34 (1961) 120–125.
[51] C. Tang, H. Peng, Y. Chen, M. Ferry, Formation and dilatation of shear bands in a Cu-Zr metallic glass: A free volume perspective, J. Appl. Phys. 120 (2016) 235101.
[52] M. Tanaka, Theoretical analysis of short-range order in liquids and amorphous metals, Bussei Kenkyu 46 (1986) A84–A89.
[53] W.K. Luo, H.W. Sheng, F.M. Alamgir, J.M. Bai, J.H. He, E. Ma, Icosahedral short-range order in amorphous alloys, Phys. Rev. Lett. 92 (2004) 145502.
[54] H.W. Sheng, W.K. Luo, F.M. Alamgir, J.M. Bai, E. Ma, Atomic packing and short-to-medium-range order in metallic glasses, Nature 439 (2006) 419–425.
[55] H.Z. Fang, X. Hui, G.L. Chen, Z.K. Liu, Al-centered icosahedral ordering in $Cu_{46}Zr_{46}Al_8$ bulk metallic glass, Appl. Phys. Lett. 94 (2009) 091904.
[56] V.S. Stepanyuk, A. Szasz, A.A. Katsnelson, O.S. Trushin, H. Müller, H. Kirchmayr, Microstructure and its relaxation in Fe-B amorphous system simulated by molecular dynamics, J. Non-Cryst. Solids 159 (1993) 80–87.
[57] S. Pan, S. Feng, J. Qiao, W. Wang, J. Qin, Crystallization pathways of liquid-bcc transition for a model iron by fast quenching, Sci. Rep. 5 (2015) 16956.
[58] M. Kbirou, A. Atila, A. Hasnaoui, On the structure and icosahedral interconnectivity in Tantalum monatomic glass produced under pressure, Phys. Scr. 99 (2024) 085946.
[59] S. Cao, G. Liu, J. Huang, X. Yu, D. Fan, Y. Ni, Y. Luo, Atomic level simulation of amorphous/nanocrystalline transition behavior in the Fe based amorphous alloys, J. Non-Cryst. Solids 624 (2024) 122726.
[60] S. Sengul, V. Guder, Key factors of deformation mechanism of Cu-Ag alloy, J. Non-Cryst. Solids 576 (2022) 121270.
[61] M. Wakeda, Y. Shibutani, S. Ogata, Atomistic formation mechanism of multiple shear bands in amorphous metals, J. Soc. Mater. Sci. Jpn. 57 (2008) 119–125.
[62] H. Tanaka, Roles of local icosahedral chemical ordering in glass and quasicrystal formation in metallic glass formers, J. Phys. Condens. Matter 15 (2003) L491–L498.
[63] V. Guder, Concentration dependence of microstructural evolution of Zr-Pt liquid alloys: A molecular dynamics study, Chem. Phys. 575 (2023) 112067.
[64] S. Mishra, S. Pal, Tailoring structural inhomogeneities in $Al_{90}Sm_{10}$ metallic glass nanowire via torsional deformation, J. Non-Cryst. Solids 595 (2022) 121830.

小特集　「レーザーで広がる歯科治療の可能性」

ナノ秒パルスレーザーによるジルコニアインプラントの表面改質

Surface modification of zirconia implants applied nanosecond-pulsed laser

[1] 鶴見大学歯学部歯科医学教育学講座
[2] 東北大学グリーン未来創造機構グリーンクロステック研究センター
廣　田　正　嗣[1]／水　谷　正　義[2]
Masatsugu HIROTA[1] and Masayoshi MIZUTANI[2]

1　はじめに

部分安定化ジルコニア（以下，ジルコニア）は，優れた審美性を有し，セラミックスでありながら非常に高い靱性を兼ね備えていることから，近年歯科において広く臨床応用されている．アレルギーを引き起こさず，メタルフリーであるという観点からも，金属や硬組織の代替材料として期待されている．そのような状況の中，海外ではジルコニアがチタンに代わる新規インプラント体材料として市販され始めており，その動向が注目されている．ジルコニアインプラントシステムは，メタルフリー志向が強いヨーロッパを中心に販売が進んでおり，1回法インプラントが主流である．最近ではエンジニアリングプラスチックを併用することなどにより，スクリューにも金属を用いない2回法システムも臨床応用されている．また，インプラント体に対しては，各社独自の酸処理やサンドブラストなどの表面処理が行われている状況である．現在，ジルコニアインプラントの安全性や有効性，特にオッセオインテグレーションに関して様々な議論が交わされている．未だにその獲得の是非については不明な部分が多いが，適切な表面処理を施せばチタンと同等の骨接触が得られるという報告も散見される．しかしながら，ジルコニアは優れた特性を有している反面，それが機械加工などのインプラントへの表面処理を困難にしているという側面もある．図1に，サンドブラスト処理を行った純チタンおよびジルコニア表面の走査型電子顕微鏡（SEM）像を示す．ジルコニアに，純チタンと同一条件でアルミナサンドブラスト処理を行っても，同一の表面形状が得られないことが確認できる．すなわち，ジルコニアインプラントの表面に対しては，従来のチタンインプラントの表面に行ってきた表面改質法とは異なった方法を模索する必要があると考えられる．

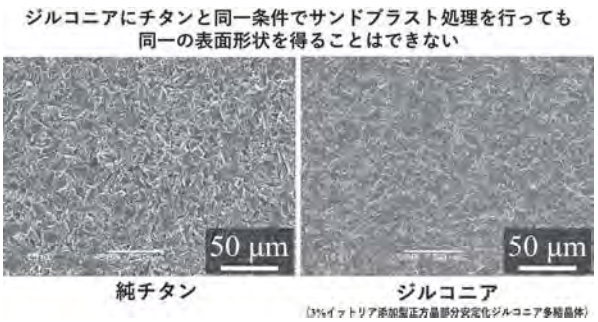

図1　50 μmAl_2O_3 によるサンドブラスト処理後のチタンおよびジルコニア表面のSEM像

そこでわれわれは，加工方法としてレーザー加工に着目し，ジルコニアインプラントの確実なオッセオインテグレーション獲得を目指したジルコニア表面へのレーザー加工処理について検討した．本総説では，その一連の医工連携による取り組みについて紹介する[1~4]．

2　ナノ秒パルスレーザーによる凹凸微細構造の作製

材料にレーザーを照射すると光熱的作用により，基材表面の形状や化学組成が変化する．われわれはジルコニアへの新しい表面改質法として，ビーム強度や焦点ずらし量を調整することにより多彩な表面加工を行うことができる，ナノ秒パルスレーザーを採用することとした．さらに，ナノ秒パルスレーザーは基材を移動させることにより，任意の場所にマイクロオーダースケールの微細かつ周期的な構造を材料表面へ付与す

ることが可能であり，これによりインプラントと骨組織のインタラクションを制御することを考えた．

現在，補綴装置としてモノリシッククラウンなどで用いられている正方晶と立方晶が共存する，いわゆる高透光性ジルコニアに対して，海外でインプラント体として市販されているジルコニアは，結晶構造が100% 正方晶である機械的強度が最も高い従来型ジルコニアである．そこでジルコニア試料として，イットリア 3 mol% 添加型（イットリア添加型）および 30 vol% アルミナ含有セリア 10 mol% 添加型（セリア添加型）の 2 種類を用意した．

1 μm 単位のプログラミングで二軸移動が可能な NC（Numerical Control，数値制御）ステージに，ナノ秒パルス Nd：YAG レーザーの発振器（Quicklaze-50trilite, NEW WAVE RESEARCH）を取り付け，光学顕微鏡下でレーザー照射を行った（図 2）．照射条件は，凹凸構造への骨芽細胞の選択的付着を狙って，幅 30 μm × 深さ 30 μm の形状付与を目標とし，30 μm × 60 μm の矩形照射領域で直線上に，パルス幅 3 ns，パルスエネルギー 150 μJ/pulse の条件でレーザーを垂直に走査した．比較対象群として，各ジルコニア試料にアルミナサンドブラスト処理後，フッ化水素酸による酸処理を行った試料（SLA 処理：Sandblasted, Large Grid, and Acid-Etched 表面を再現）を作製した．

図 2　レーザー照射システムの外観

図 3 の SEM 像に示すように，レーザー加工後の表面構造は，イットリア添加型，セリア添加型どちらもスポット径と同程度の幅 30 μm，深さ 30 μm，の規則的な凹凸構造の形成が確認できた．強拡大像を見ると，凹部には蒸散によって得られたと思われるフラクタル様の粗糙構造が認められた．イットリア添加型とセリア添加型の顆粒状物の大きさの違いは，溶融した基材が急冷により凝集した時の影響であると考えられた．これらの表面粗さおよび比表面積の増加が，骨形成に対して有利に作用するものと期待された．

3　レーザー照射によるジルコニアの化学的変化

一方，ジルコニア試料をマクロで観察すると，イットリア添加型では変色は見られなかったのに対し，セリア添加型の表面はレーザー照射により黒く変色していた（図 4）．そこで，エネルギー分散型 X 線分析（EDX），および X 線光電子分光法（XPS）による表面分析を行った．EDX からは，セリア添加型において酸素の原子欠損数がイットリア添加型と比較して，

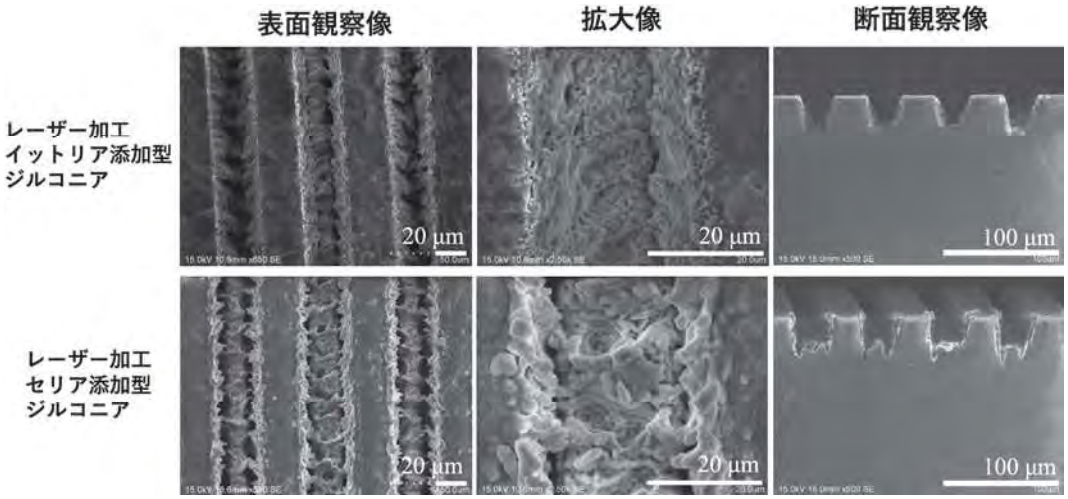

図 3　レーザー加工後のジルコニア表面および断面の SEM 観察像（文献 1 より一部改変引用）

10% 以上多いことがわかった．XPS 分析においても，EDX による分析結果と同様に酸素原子の欠損が認められ，ジルコニウムイオンの還元が観察された（$ZrO_2 \rightarrow ZrO_{2-x}+xO$）．セリア添加型の成分に含有するアルミナは，熱伝導率がジルコニアよりも 10 倍以上高いために，レーザー照射によって高温領域が拡散しやすくなり，酸素欠損が多く生じたために黒変したと考えられた．加えて，この黒変は電気炉で，1,000℃，15 分間留置後炉冷を行うことにより，白色へ色調回復できることがわかっている．

次に，X 線回折法（XRD）による結晶構造の分析を行った．その結果，対照群では結晶構造が単斜晶であるジルコニアのピークが観察されたのに対し，各レーザー加工ジルコニアでは，ほぼすべてのピークが正方晶ジルコニアであることが明らかになった（図 5）．ジルコニアに表面処理を行う際の問題点として，正方晶ジルコニアに機械加工や研磨を行うと一部の結晶構造が単斜晶へ変態するとともに，機械的性質などが低下すると懸念されている．しかしながら今回，レーザー照射前の試料の加工に由来する単斜晶に変態していたジルコニアが，ナノ秒パルスレーザーを照射することで生じる熱影響により，副次的効果として母材本来の正方晶に回復していることが明らかになった．すなわち，サンドブラスト処理などの従来の機械加工による表面改質法と比較して，母材表面の正方晶を維持し，機械的性質を担保できる点でジルコニア表面への処理として本レーザー加工が有効であることが示された．レーザー加工は，照射によって基材表面の形状のみならず，化学組成なども変化させることにより，多彩な機能的表面を創成することができる．ジルコニア表面の結晶構造を維持できるレーザー処理のベネフィットは，インプラント体材料への適用だけではなく，他の用途にも応用が期待できると考えている．

4 動物へのインプラント埋入による骨適合性評価

ラット大腿骨に作製した欠損部へのインプラント埋入を行った結果を図 6 に示す．術後 4 週目において，レーザー加工イットリア添加型ジルコニアインプラントでは対象群と比較して，より多くの新生骨形成が確認できた．さらに，解析ソフトを用いて骨形態学的計測を行った結果，有意に高い骨–インプラント間接触率（BIC）が得られ，ジルコニアへのレーザー加工処

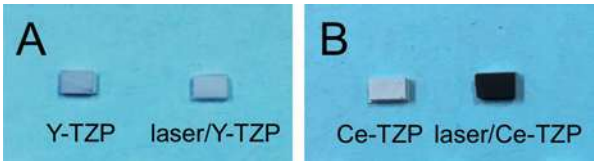

図 4　レーザー照射によるセリア添加型ジルコニアの黒化（文献 1 より引用）
（A）イットリア添加型ジルコニア（Y-TZP），（B）セリア添加型ジルコニア（Ce-TZP）．

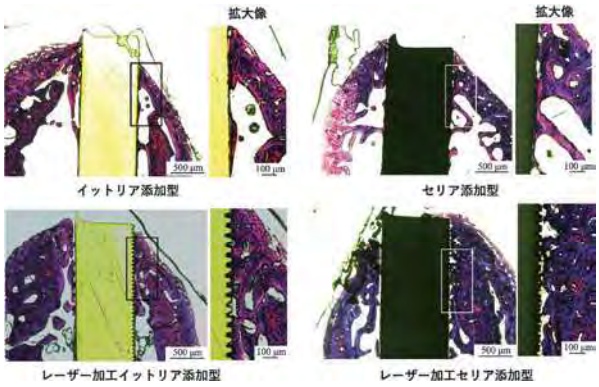

図 6　インプラント周囲の病理学的組織像（文献 1 より一部改変引用）

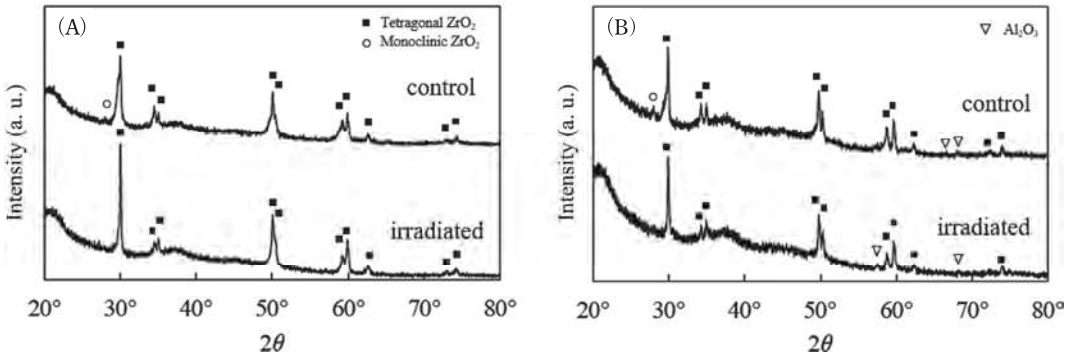

図 5　XRD による結晶構造の分析結果（文献 2 より一部改変引用）
（A）イットリア添加型ジルコニア（上：Y-TZP，下：レーザー加工 Y-TZP），（B）セリア添加型ジルコニア（上：Ce-TZP，下：レーザー加工：Ce-TZP）．

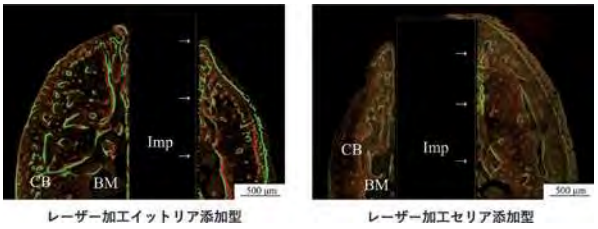

図7　インプラント周囲の CLMS 像（文献 1 より一部改変引用）
Imp：インプラント体，CB：皮質骨，BM：骨髄，矢印：レーザー照射側．

理がサンドブラストおよび酸処理よりも効果的であることがわかった．また，術後 2 週および 3 週目に施したキシリノールオレンジおよびカルセインによるラベリングを共焦点レーザー顕微鏡（CLSM）により観察すると，インプラント体の凹凸部に対して，一部の垂直方向への骨形成がみられた（図 7）．レーザー加工処理により付与された微細構造が，新生骨形成に何らかの影響を及ぼした可能性が示唆された．一方，レーザー加工セリア添加型ジルコニアインプラントでは，明瞭な骨接触はみられず，対象群と比較しても有意に低い BIC であった．イットリア添加型とセリア添加型とでレーザー照射後の加工面では大きな違いがみられなかったことから，ジルコニアインプラントの骨形成には表面形状だけではなく，レーザー照射によって生じた表面組成の変化が影響することが推察された．

5 インプラント材料としてのジルコニアの将来性

医療安全水準が高い日本では，ジルコニアはインプラント体材料としては未認可である一方，海外においては十分なエビデンスを欠いたまま，臨床が先行するかたちでインプラント体への応用が始まった．ジルコニアインプラントは，既存の方法ではチタンと同一の表面形状あるいは表面性状となるように加工処理することが難しく，ジルコニアの材料特性に見合った表面改質法を早急に検討する必要がある．本総説で紹介したナノ秒パルスレーザーによる表面加工処理は，微細構造の付与と同時に，生体活性を向上させるような表面の化学的性質などをも付与することが可能であり，ジルコニアの新規表面改質法として有効な方法であると考えている．今回の取り組みから，ジルコニアインプラントにナノ秒パルスレーザー加工で表面改質を行う際は，表面形状だけではなく，化学組成への影響にも注意する必要があることが示唆された．

近年，ジルコニアインプラントでは埋入後の歯肉の炎症が比較的軽微であるなどの軟組織との良好な親和性に関して，ジルコニアの優位性が報告されている．研磨したジルコニア表面はチタンと比較して滑沢であり，化学的にも相対的に親水性が低いことからプラークの付着性が低く，歯肉貫通部においてインプラント周囲炎を引き起こしづらいと期待される．したがって，ジルコニアに接するそれぞれの組織に対してインタラクションを活性化するような表面処理を施せば，ジルコニアは，骨および歯肉双方への良好な組織適合性が期待できる魅力的な材料である．現在，われわれは次なるステップとして，インプラント周囲炎を制御する軟組織付着を目指したジルコニアの表面改質法について検討を始めている[5]．

ジルコニアインプラントは，長期の臨床経過に関する報告が乏しく，セラミック材料の中では高靱性とはいえあくまで脆性材料であることから，チタンインプラント（金属材料）と比較すると破折が懸念され，また高剛性であることから骨組織への応力集中に対する問題が懸念される．今後，日本で安全に臨床応用するためには未だ大きな課題があり，基礎および臨床研究によるエビデンスの蓄積が急務であると考えている．

本研究で紹介した成果の一部は，JSPS 科研費 22H01827，17K17225，17K06074 および 17KK0126 の助成の援助により行われた．研究遂行にあたり鶴見大学早川　徹名誉教授にご助言を賜り深謝いたします．

もっと知りたい読者のために

1） Hirota M, et al. Cortical bone response toward nanosecond-pulsed laser-treated zirconia implant surfaces. Dent Mater J 2019；38：444-451.
2） 原井智広ほか．ナノ秒パルスレーザによるジルコニアインプラントへの生体適合性付与―微細溝の創成および熱影響の検討―．日本金属学会誌　2019；83：37-45.
3） Harai T, et al. Low-temperature degradation of yttria-stabilized zirconia treated with pulsed laser and annealing techniques. Precision Engineering 2023；80：45-56.
4） 廣田正嗣ほか．ジルコニアインプラントの表面改質．再生歯誌 2024；22：1-10.
5） Takayama H, et al. Influence of fibronectin immobilization on the orientation of collagen bundles in soft tissue around zirconia implants. J Hard Tissue Biol 2024；33：31-38.

別　刷

設計工学

公益社団法人　日本設計工学会誌

2024年　第 59 巻　第 12 号

（　P. 583 ～ P. 589　）

金属積層造形による傾斜多孔質構造体の創成
（根状多孔質構造体（RPS：Rhizoid Porous Structure）の提案とその応用）

水谷　正義

Graded Porous Structure Creatation with Metal Additive Manufacturing
(Proposal of Rhizoid Porous Structure (RPS) and Its Application)

Masayoshi MIZUTANI

公益社団法人 日本設計工学会

解説

金属積層造形による傾斜多孔質構造体の創成＊
（根状多孔質構造体（RPS：Rhizoid Porous Structure）の提案とその応用）

Graded Porous Structure Creatation with Metal Additive Manufacturing
(Proposal of Rhizoid Porous Structure (RPS) and Its Application)

水谷　正義[*1, 2]
（Masayoshi MIZUTANI）

Key Words : graded porous structure, metal additive manufacturing, rhizoid porous structure, bio-implant

1．はじめに

多孔質金属材料は「複数の空孔からなる多孔質構造を内包した金属材料」として捉えられ，1980年代後半から欧州を中心に研究開発が活発化し，今日に至るまで多くの分野で活用されている[1)]．この場合の「空孔」とは，意図せずして材料中に生じるいわゆる「欠陥」としてではなく材料に副次的な機能性を与える「機能的な構造」の一形態として捉えられる．このような特異な構造がもたらす工業的な利点としては，軽量化，高比強度，高衝撃吸収性，制振性，断熱性などがあげられる．それらの機能性は空孔の形態（形状，分布，空孔率など）の影響を顕著に受けるため，多孔質材料の作製手法においては，空孔形態の制御がとくに重要となる．本稿では，多孔質金属材料の従来手法に対して，金属積層造形（AM：Additive Manufacturing）を用いた設計概念，ならびに著者らが提案する新たな手法について概説する．

2．多孔質構造体の創成手法

多孔質構造は自然界において特殊なものではない．例えば，木材や珊瑚は機能的に最適化された多孔質構造により多くの利点を生み出している．その多孔質構造を人工的に作成するため，これまでに多くの手法が提案されてきた．まずはその一部を紹介する．

＊　原稿受付：2024年7月3日
＊1　非会員，東北大学グリーン未来創造機構グリーンクロステック研究センター
（〒980-8579　仙台市青葉区荒巻字青葉6-6-01）
＊2　非会員，東北大学大学院工学研究科機械機能創成専攻（同上）

ガスインジェクション法[2)]は，溶融金属が凝固するまでの間にガスを吹き込み，内部に気泡を生成させることで多孔質金属材料を作製する手法である．本手法では簡便かつダイレクトに空孔を形成させることができるため，他手法に比べて製造コストが低いという利点がある．一方，空孔の形態は溶融金属の粘度や重力の影響を受けるため，その制御は難しく密度が不均一になりやすいなどの問題点もある．

数mm程度の空孔を有する空孔率70%以上の多孔質金属は発泡金属と称される．代表的な材料はアルミニウムであり，エネルギ吸収部材や高比剛性構造部材への応用が期待されている．プリカーサ法[3)]では，例えばアルミニウム合金粉末にTiH_2などの発泡補助粉末を添加し，その混合粉末を固化成型して発泡プリカーサを作製する．それを合金の融点以上に加熱することで合金の一部が溶融すると共に発泡補助剤から分解発生するガスが空孔を形成する．このときプリカーサは体積膨張するため，中空部材の中で加熱発砲すれば中空部材と発泡金属の複合部材を容易に成型できる．一方，大型製品や長尺製品では均一加熱が難しいため不向きであること，他のプロセスに比べて材料コストが高価であることが現状の課題となっている．

スペーサー法（レプリカ法）[4)]は，水溶性の物質（塩化ナトリウムなど）からなるスペーサー粒子を鋳造や焼結などの手法で金属中に配置し，水洗いや加熱により取り除くことで粒子の形状に準じた空孔を材料中に残留させる手法である．このとき形成される空孔はスペーサー粒子の形態（密度・粒径・形状・分布）を転写したものであるため，高精度での空孔制御が可能となる．また，空孔同士が連結した開気

孔を導入可能な点も大きな特徴である．そのため，機械的性質に及ぼす多孔質構造の影響を調査するためのモデル材料や，流体透過性を利用したフィルタ・熱交換機への応用が提案されている．また，アルミニウムや鋼，チタンなど様々な金属が使用可能であり，その適用範囲は非常に広い．現在は射出成型技術と組み合わせることで多孔質金属部品をネットシェイプで量産する試みもなされている[5]．

3. 根状多孔質構造体（RPS）の提案

極めて高い形状設計自由度をもつAMは，内部多孔質構造が幾何学的あるいは機能的にデザインされた多孔質金属材料の作製に非常に適した手法である．AMによる多孔質構造の作製プロセスは多くの場合，**図1**のような最小単位構造の設計から始まる．この単位構造はユニットセルと呼ばれ，全体構造の特性を決定づける重要な要素である[6]．ユニットセルの最適設計にはしばしばトポロジー最適化[7]などの解析的手法が採用される．設計されたユニットセルは造形物外形状の設計空間に周期的に当てはめられることで，最終的な全体構造を得る（**図2**）．空孔の分布や形状は計算機による設計の段階で任意に操作可能であり，空孔形態の制御という点では従来手法を大きく上回る自由度を発揮する．ただし，AMの性質上，オーバーハング形状では造形不良が生じる可能性が高いため，構造中の梁の寸法や角度については慎重な検討がなされるべきである．また，空孔が互いに独立した閉気孔の形態をとる場合は，造形に使用されなかった粉末が空孔内に残留するため，それを抜き出すための貫通孔を設ける必要がある．その場合，全体構造の機械的強度は設計値よりも低下することに留意しなければならない．

こうした考え方に対して著者らは，AMによる造形物内部に形成される空孔欠陥を利用した構造を提案しており，連結空孔の特徴的な形状から根状多孔質構造（RPS：Rhizoid Porous Structure）と名付けた．RPSは**図3**に示したような数十～数百ミクロンオーダの閉気孔および開気孔を有し，その空孔率はレーザ走査速度などの造形条件によって任意に制御可能である．**図4**に，造形時のエネルギ密度と空孔率の関係を示す．ここで，エネルギ密度E_d[J/mm^3]とは造形時に単位体積当たりに投入される熱量を指し，レーザ強度p[W]，積層厚t[mm]，走査幅d[mm]，走査速度s[mm/s]を用いて以下の式で定義される．

$$E_d = \frac{p}{tds} \qquad (1)$$

現時点で，空孔率は最大で約45%の値を達成しており，エネルギ密度の増加に伴って5%付近に漸近していくという傾向が**図4**のグラフから予想されている．また，使用材料粉末の粒度分布が粉末床におけるレーザの吸収率に影響を与え，空孔形成の促進および抑制に寄与することが示唆されている．

本手法では専用の設計ソフトウェアなどを使用せずに，AMによる簡便な方法で多孔質構造を作製することが可能となる．また，ユニットセルを用いた設計手法では形状の再現が困難であるような数ミリオーダの設計対象物に対しても多孔質構造を付与することが可能である．さらに，設計領域に対して部

Fig. 1 ユニットセルの3Dモデル

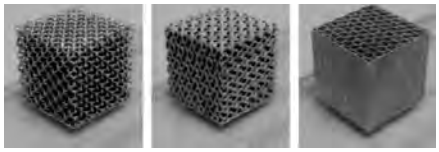

Fig. 2 AMによって作成された多孔質構造体

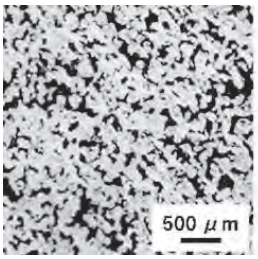

RPS材料の断面画像

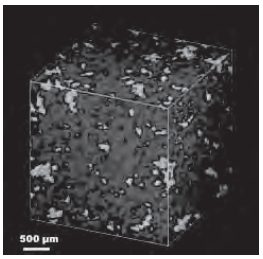

空孔可視化画像（CT画像）

Fig. 3 RPSの内部構造

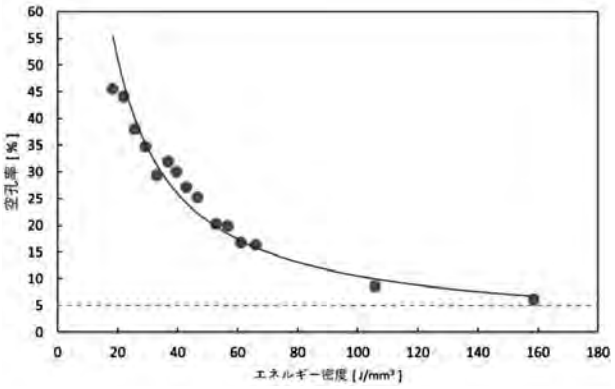

Fig. 4 エネルギ密度とRPSの空孔率の関係

分的に異なった造形条件を適用することによる空間的な空孔率分布の制御も可能であり，空孔率が傾斜的に変化する傾斜多孔質構造体の造形も可能になる．なお，空孔形成の規則性については詳細な調査を進めており，高い自由度での空孔形態制御を試みている．最終的には，力学的あるいは機能的な事前設計から適切な造形条件を導出し，所望の特性を有する多孔質金属製品をニアネットシェイプで実体化するプロセスの確立を目指している．

4. 医療分野における多孔質構造体の活用

自然界で見られる多孔質構造の典型的な例として，我々の身体を支える骨が挙げられる．人骨は，骨密度が大きい緻密な皮質骨（Cortical bone）の内側に，多数の細い梁状の骨（骨梁）が網目状に張り巡らされた海綿骨（Trabecular bone）を有する．この骨梁構造は，人体が日常的に曝される力学的環境に最適化するようにモデリングされた機能的多孔質構造である[8]．この特異な構造により，骨は軽量かつ高剛性・高強度といった優れた機械的特性を備えている．それに倣い，金属製インプラントも同様に多孔質構造を有するべきであるという考えの下で，多孔質金属材料をインプラントに活用する試みが多くなされている．図5に，AMによって作製された多孔質インプラント（ステム）を示す[9]．このようなインプラントの多孔質化は，生体的あるいは力学的な適合性を向上させるという点で非常に有用である．例えば，多孔質化によりインプラントの構造的な弾性率を低減させることでインプラント－骨界面におけるひずみの不連続性や力学的応力遮蔽の緩和が期待できる．また，空孔の伸長方向を制御することによる，骨が持つ機械的異方性の再現も試みられている[10]．さらに，骨芽細胞は100～200μm以上の径を持つ空孔内部で成長が活発化するという性質を利用し，空孔内部での骨形成を促すことでインプラント－骨界面の結合を向上させるという考え方も採用されている．以上のことから，多孔質金属材料はインプラントの課題解決や高機能化を達成するための重要な因子であるといえる．

このような背景に対して，著者らが提案しているRPSを応用した高機能性インプラントの概念を図6に示す．同図では歯科用インプラントを例としている．本インプラントの外形状は，患者個人の骨格に対して最適化される．また，緻密領域と多孔質領域の階層構造をなすことで，実用に供することができる最低限の強度と副次的な機能を両立する．つまり，

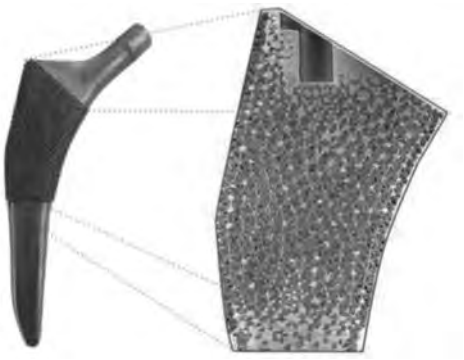

Fig. 5　AMによって作成された多孔質インプラント[9]

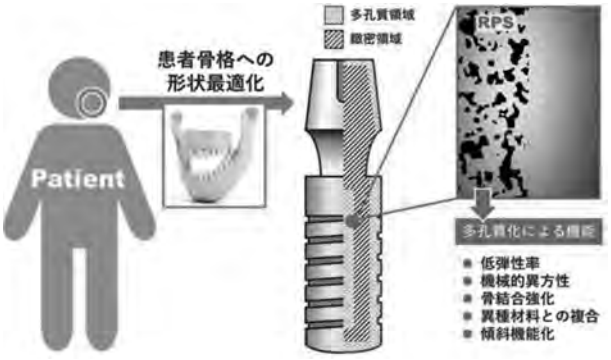

Fig. 6　RPSを応用した高機能性インプラント（コンセプト）

本インプラントはテーラーメイド性，多機能性および高強度の3要素を相乗的に備えている．著者らはRPSの空孔形態の制御自由度を拡張し，また，機械的性質を含むRPS材料の基本的特性と副次的な機能性を評価することで，高機能性インプラントの実現を目指している．

5. RPSを応用した傾斜多孔質構造体の創成

「空間的に1つの機能から他の機能へと連続的または段階的に変化する1体の材料」を傾斜機能材料（FGMs：Functionally Graded Materials）と呼ぶ[11]．このとき，機能の遷移は組成や構造の変化によってもたらされる．図7に，2種類の組成からなる傾斜機能材料の概念図を示す．それぞれが大きく異なった特性を有する2つの材料を単に接合した場合，その巨視的界面では特性が不連続的に変化し，剥離や応力集中による破壊の起点になり得る．一方，傾斜機能材料では特定の巨視的界面は存在せず，特性は緩やかに変化していく．これにより，構造全体の強度を確保しながら，複数の機能を相乗的に備えた複合材料が実現される．構造の変化によって機能を傾

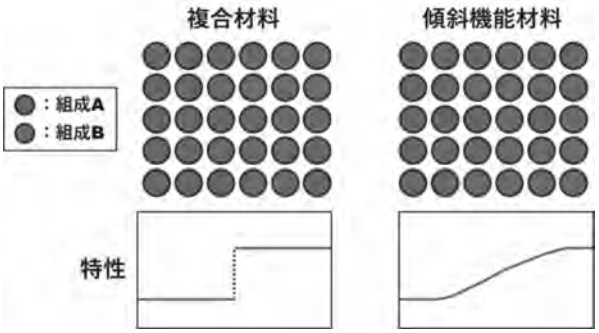

Fig. 7 傾斜機能材料の組成および特性変化

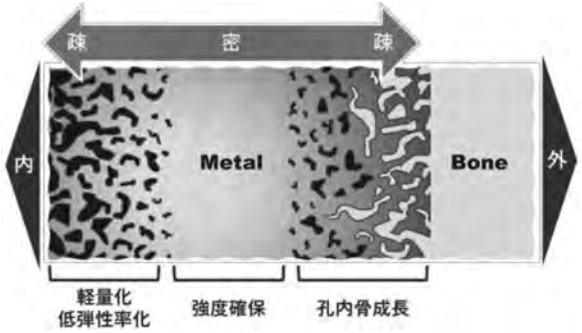

Fig. 8 RPSを応用したインプラント用構造の概念図

斜させている材料の典型が骨である．前述した通り，骨は高密度の緻密骨と無数の小さな空孔を持つ海綿骨からなる階層構造を有している．その境界領域は空孔率が緩やかに変化する傾斜構造となっており，緻密骨に負荷された外力は内部の海綿骨へとスムーズに伝達・分散される．これによって，骨は構造全体で外力を支えることが可能となり，軽量化と高強度の相反する2つの要素を両立している[12]．

本研究で提案するRPSを応用した高機能性インプラントもまた，単一のインプラント体において複数の機能を有する複合構造体として提案できる．インプラントの多孔質化によってもたらされる大きな利点の1つは弾性率の低減である．しかしこの場合，多孔質化による強度の低下は避けることができないため，設計領域全体を均一の多孔質構造で構成することは現実的ではない．したがって，特定の領域では空孔の形成を抑制し緻密化することで，最低限の構造強度を確保する必要がある．また，空孔によって得られる副次的な機能の1つに金属－骨界面における接合強度の向上が挙げられる．これは空孔によって誘起される孔内骨成長（イングロース）を利用したもので，インプラントと骨の強固な結合や界面における応力集中の緩和が期待される．したがって，インプラント表層部には特定の空孔率をもつ多孔質面を配置することが，生体適合性の点で非常に有効であると考えられる．以上の設計理念に基づいたインプラント用構造の概念を図8に示す．本構造は設計領域を部分的に多孔質化あるいは緻密化し，それぞれの領域が先述した異なる機能を担っている．各領域の空間的な遷移は空孔率の変化に付随し，かつ遷移領域は骨に見られるような傾斜構造となっている．以下，空孔率が連続的あるいは段階的に変化する構造を傾斜多孔質構造と称する．

本稿ではその第1段階として，分割した設計領域をそれぞれ異なる条件で造形することで，積層方向

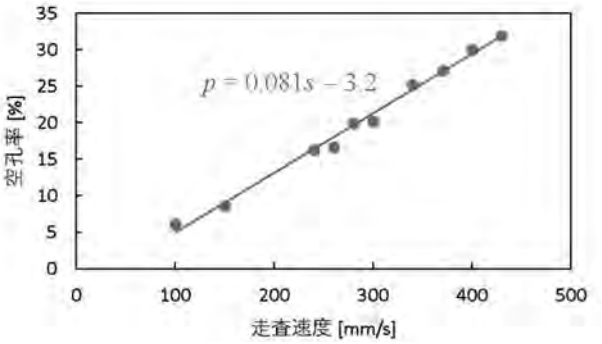

Fig. 9 レーザ走査速度と空孔率の関係

と径方向のそれぞれに沿った空孔率勾配を有する傾斜多孔質構造体の創成を試みた結果を紹介する．

5.1 積層方向への傾斜化

本実験では「特定の厚みの層を積み重ねる」というAMの特徴的な工程を利用し，積層方向に沿って空孔率が傾斜的に変化する多孔質構造の作製を試みた．著者らのこれまでの研究から得られているレーザ走査速度とRPSの空孔率の関係を図9に示す．グラフより，走査速度100-430mm/sの範囲では空孔率と走査速度は比例関係にあると仮定し，最小二乗法によって以下の実験式を得た．

$$p = 0.081s - 3. \qquad (2)$$

（p：空孔率［%］，s：走査速度［mm/s］）

試験片はϕ7mm，高さ4.5mmの円柱とした．その設計領域を高さ方向に10分割し，それぞれの領域に異なる走査速度を割り当てた．設計領域の区分を図10に示す．同図中に示した各領域の空孔率は，式(2)に走査速度の値を代入することで求めた設計値である．積層方向をz軸方向とし，試験片最低面をz＝0［mm］とした．造形時に設定したレーザ走

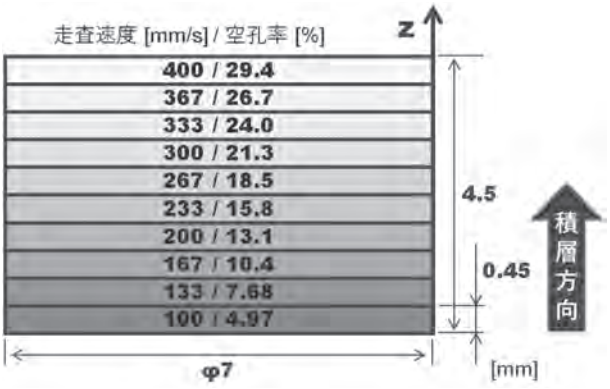

Fig. 10　試験片の設計領域区分（積層方向）

査スタイルはXY走査である．また，造形した試験片を倍率28.9，分解能8.8μm/pixelの条件でX線CTスキャンにかけ，4.53 × 4.53 × 4.50mm^{3}の直方体領域におけるCT画像を積層方向に511枚取得した．各CT画像を二値化し，1枚当たりの面空孔率を算出することで積層方向に沿った空孔率プロファイルを作成した．なお，試験片と空気層および試料台との境界付近では画像中のノイズが多く，明瞭なCT画像を得ることができなかったため，全CT画像の内，z = 0.34-4.2[mm]の範囲にあたる444枚を最終的な評価対象とした．

z = 0.34，2.3，4.2[mm]の各位置におけるz軸に垂直な断面のCT画像（二値化後）を**図11**に示す．同図より，高さの増加に伴って空孔率が顕著に増加していることが分かる．**図12(a)**に示した積層方向に平行な断面におけるCT画像（二値化後）からは，各領域の巨視的界面は確認されなかった．また，**同図(b)**に，積層方向に沿った空孔率プロファイルを示す．なお，同図中には，比較として走査速度240mm/sで造形した7mm角立方体試験片のデータも併記している．空孔率プロファイルより，試験片の空孔率は設計値と概ねよい一致を示しながら積層方向に沿って傾斜的に変化していることが確認された．これは著者らが提案する方法（概念）により，空孔率を積層方向に沿って傾斜的に変化させた多孔質構造体の作製が可能であることを示すものである．

5.2　径方向への傾斜化

前節より，積層方向に沿った空孔率傾斜は実現可能であることが明らかとなった．ただし理想とする高機能性インプラント実現のためには，積層方向に加え，径方向への空孔率傾斜が必須となる．本実験では，径方向に沿って空孔率が傾斜的に変化する多

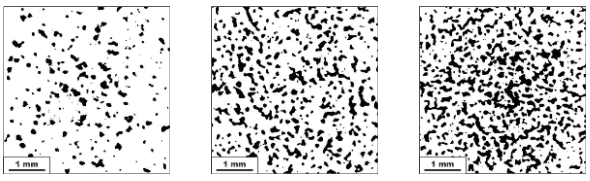

z = 0.34 [mm]　z = 2.3 [mm]　z = 4.2 [mm]

Fig. 11　各断面におけるCT画像（二値化後）

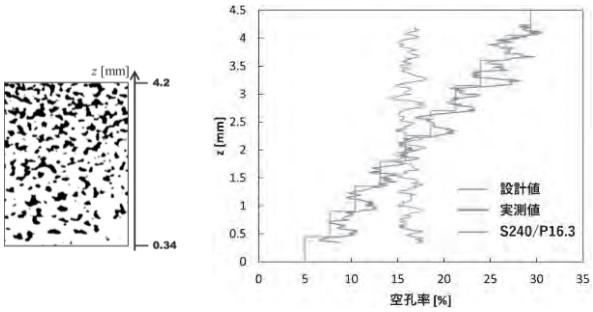

(a) CT画像（二値化後）　(b) 空孔率プロファイル

Fig. 12　積層方向への空孔率変化

孔質構造体の作製を試みた．

試験片はϕ8mm，高さ8mmの円柱とした．設計領域を幅0.5mmの円筒形領域に区分し（中心はϕ1mmの円柱となる），それぞれの領域に異なる走査速度を割り当てた．設計領域の区分を**図13**に示す．各領域は内側から順番にSection 1，2…8とした．同図中の空孔率は前節と同様に式(2)から求めた設計値である．本実験では，内側から外側にかけて空孔率が上昇する傾斜変化パターンを動径方向傾斜，その逆を内心方向傾斜とした．レーザ走査は設計領域の外周に沿って，外側から内側に向かって造形が進行するアウトライン走査を採用した（**図14**）．また，造形した試験片をダイヤモンドカッタにて中央付近で切断し，#2000まで機械研磨した断面を光学顕微鏡にて撮影した．その後，顕微鏡画像を二値化し，Sectionごとの面空孔率を算出した．

造形した試験片の断面顕微鏡画像と，Sectionごとの空孔率プロファイルをそれぞれ**図15**と**図16**に示す．顕微鏡画像からは，両パターンにおいて傾斜方向に沿って空孔率が変化する様子が確認され，Section間の巨視的界面は見受けられなかった．また，空孔率プロファイルより空孔率の傾斜的な変化が確認されたが，二値化画像から算出した空孔率の実測値は全Sectionで設計値よりも低い値を示した．この原因としては式(2)の導出に際して参照し

Fig. 13　試験片の設計領域区分（径方向）

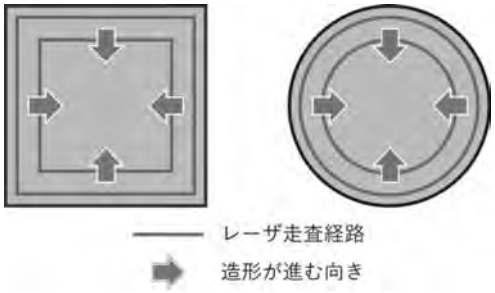

Fig. 14　アウトライン走査のイメージ

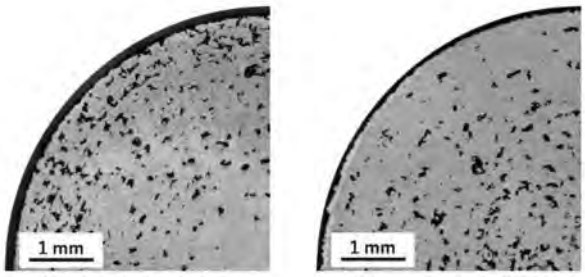

Fig. 15　断面顕微鏡画像

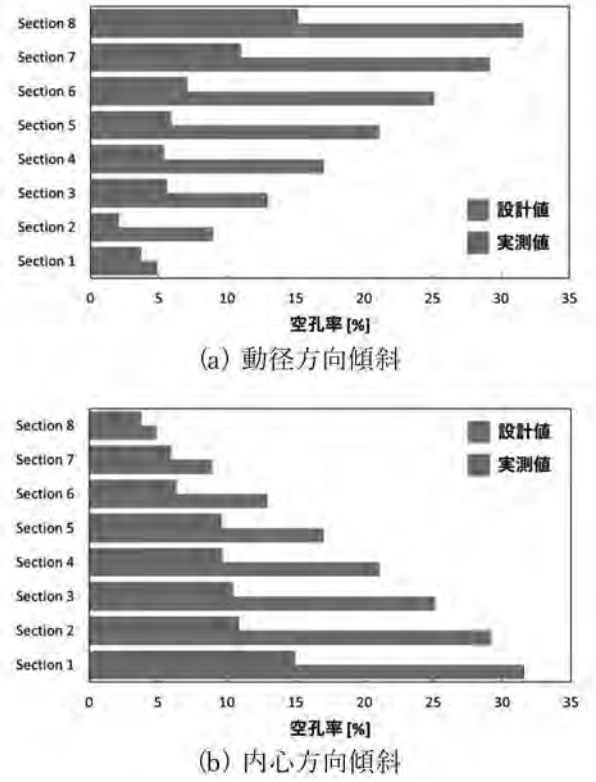

Fig. 16　空孔率プロファイル

た空孔率は7mm角立方体試料の値であり，本試験片とはレーザ走査スタイル・造形面積ともに異なっていることに起因していると考えられる．とくに各Sectionあたりの造形面積は立方体と比較して小さいため，構造体造形中の冷却過程の違いが空孔の形成現象に影響を及ぼしたと考えられる．

以上の結果から，事前設計の値に即して空孔率を遷移させることはできなかったものの，設計領域の分割によって空孔率を径方向に沿って傾斜変化可能であることが実証された．

6. おわりに

著者らは，金属積層造形（AM）によって創成される根状微細多孔質構造（RPS）を応用した高機能性インプラントの実現可能性を示すことを目的とし，RPSの空孔形態制御性および諸機能性を様々な観点から検証を行っている．その中で本稿ではRPSを応用した高機能性インプラントの内部構造を提案し，その実現に際して必須である傾斜多孔質構造体の創成に成功した事例を紹介した．具体的には，対象となる設計領域を区分し，それぞれの分割領域に異なるレーザ走査速度を割り当てる積層方向と径方向それぞれに沿って傾斜的に空孔率を変化させることに成功している．これらの知見は，例えばインプラント用構造体としてRPSを活用することで，高強度・低弾性率・機械的異方性といった力学的機能と，孔内骨成長による強固な骨結合の獲得といった副次的な機能を相乗的に備えた高機能性インプラントを実現可能であることを示すものである．

もちろん本手法の応用範囲は生体・医療分野のみならず，幅広い応用が期待できるものである．例えばRPSを異種材料（CFRP-Ti）の接合に適用した取り組み[13]も進めている．ぜひ参考にされたい．

謝辞

本稿で述べた内容は多くの学生の努力と関係者のご協力により遂行されたものであり，関係各位に心から感謝申し上げる．とくに佃将希 氏，溝井琢巳 氏，中善寺優昴 氏，石橋信治 氏，Li Zhenjun 氏，

高野直輝 氏に深く感謝する.

参考文献

1） 金武直幸，ポーラス金属の可能性と将来展望，日本機械学会機械材料・材料加工部門ニュースレター，52(2015)，1.
2） 小橋眞，ポーラスメタルの現状と展望，軽金属，55, 7(2015)329.
3） 金武直幸，超軽量クローズドセル型ポーラス金属の作成方法，マクロ及びポーラス金属の開発最前線，(2017)，7-12.
4） 袴田昌高，馬渕守，スペーサー法による微細孔ポーラス金属の創成と特性評価，軽金属，62, 8(2012)，313-321.
5） 西藪和明，松崎覚，田中茂雄，パウダースペースホルダー法により製造したマイクロポーラス金属粉末射出成形および押出成形品の寸法精度，粉体および粉末冶金，53, 9(2006)，776-781.
6） W. Tao, M. C. Leu, Design of lattice structure for additive manufacturing, ISFA2016, (2016), 326-327.
7） M.P.Bendsoe, O.Sigmund, Topology Optimization: Theory, Methods and Applications, SpringerVerlag, (2003).
8） 大塚正久，セル構造体　多孔質材料の活用のために，内田老鶴圃，(1993)，431-445.
9） S. Arabnejad, B. Johnston, M. Tanzer, D. Pasini, Fully Porous 3D Printed Titanium Femoral Stem to Reduce Stress-Shielding Following Total Hip Arthroplasty, Wiley Online Library, (2016), 3.
10） 池尾直子，3Dプリンタ活用による骨代替材料の開発，「新たなものづくり」3Dプリンタ活用最前線，(2015)，207-209.
11） 吉成正雄，インプラント材料とその表面：その1.インプラント材としてのチタン，歯科学報，103, 5(2003)，313.
12） 上村誠一，渡辺義見，傾斜機能材料の基礎と応用，コロナ社，(2014)，9-10.
13） K. Shirasu, M. Mizutani, N. Takano, H. Yoshinaga, T. Oguri, K. Ogaaw, T. Okabe, S. Obayashi, Lap-shear strength and fracture behavior of CFRP/3D-printed titanium alloy adhesive joint prepared by hot-press-aided co-bonding, International Journal of Adhesion and Adhesives, 117 (2022), 103169.

水谷　正義

2006年慶應義塾大学大学院理工学研究科博士課程修了．同年理化学研究所先端技術開発支援センター協力研究員．2007年理化学研究所大森素形材工学研究室協力研究員．2009年同基礎科学特別研究員．2011年上智大学理工学部学外共同研究員．2012年理化学研究所大森素形材工学研究室協力研究員．同年10月より東北大学大学院工学研究科准教授を経て2023年4月より同大学グリーン未来創造機構グリーンクロステック研究センター教授.

皮脂汚れに対するウルトラファインバブル (UFB)の洗浄効果の検討 ～化粧品成分に対する除去能力の検討～

東北大学　○中丸宏平　東北大学[院]　水谷正義

Examination of the cleaning effect of Ultra Fine Bubble (UFB) on sebum stains ～Examination of removal ability for cosmetic ingredients～

Kohei Nakamaru and Masayoshi Mizutani

1　緒　　言

ウルトラファインバブル(以下, UFB)とは直径 1mm 以下の微小な気泡である．UFB は非常に長寿命で，洗浄効果や殺菌効果といった様々な特徴を持つことが知られている．このことから近年，産業，環境，食品，農業，美容, 医療等の様々な分野での開発が進められている [1]．しかし，各分野で UFB を使用する際，UFB のどのような特徴がどのように発現して効果を生み出しているのか，その詳細なメカニズムについては未解明な部分が多く存在する．例えば美容の分野では，UFB を用いたシャワーヘッドなどが開発されており，その洗浄効果 [2]や保湿効果 [3]が報告されているが，その効果がどのように発現しているかは不明な点も残されている．そこで本研究では, 皮脂汚れに対する UFB の洗浄効果を明らかにし，その効果が発現するメカニズムを解明することを目的とした．本報はその第 1 段階であり，皮脂汚れの原因の 1 つでもある，ファンデーションの汚れに着目し，UFB が存在する環境中でその汚れがどのような挙動を示すかについて検討・考察した．

2　UFB の挙動の確認

2.1　UFB の生成方法

UFB 生成装置(NQ-KP-MI.5CD-200/60-R3S，ナノクス)を用いて生成した．同装置では，ポンプ内で気体と流体を混合し，加圧した高圧混合流体をミキサに送る．このミキサ内で混合気体が船団を繰り返されることで，バブルが分断され，UFB が生成される仕組みである [4]．各生成条件を **Table1** に示す．

2.2　UFB の生成の確認

ナノ粒子ブラウン運動追跡法(Nanosight　NS500)を用いて UFB の生成を確認する．UFB は 1mm 以下の気体粒子であるので，ブラウン運動をし，レーザー波長であれば散乱光を発することを利用して運動軌跡を探し出し解析できる．このとき解析に用いる関連式は，平均二乗変化量を用いて，拡散係数 D を導出する式(1)と Stokes-Einstein の式(2)の 2 つであり，これらの式から UFB の気泡径を算出できる．

本実験で用いた UFB の密度と気泡径は Table2 に示す．

$$\frac{\overline{(x、y)^2}}{4}=D \tag{1}$$

K_B：ボルツマン定数　D：拡散係数

η：粘度　T：絶対温度

$$D=\frac{TK_B}{3\pi\eta d} \tag{2}$$

Table 1　Conditions for generating UFB

Generation conditions	Air, O_2	CO_2
Gas pressure [MPa]	0.1	0.1
Pump pressure [MPa]	1	0.7
Gas flow rate [ml/min]	200	100
Operating time [min]	15	10

Table 2　Density and bubble diameter of UFB

Enclosed Body	Average Density [particles/ml]	Average Bubble Diameter [nm]
Air	6.32e+07 +/-3.24e+06	138.0 +/-1.9
O_2	5.54e+07 +/-8.43+06	137.7 +/-5.8
CO_2	9.40+06 +/-8.54+05	175.5 +/-20.4

3　ファンデーションの洗浄

3.1　実験手順

人工皮膚モデルにファンデーションを約 300mg ずつ塗り，24 時間乾燥させた．その後，人工皮膚モデルを UFB- Air を封入した UFB 水に浸漬させ，1 日静置した．このうち半数は，撹拌を行ってから浸漬させた．その後，それぞれ挙動を観察し，ファンデーションが人工皮膚モデルから剝がれる様子について確認した(Fig.1)．なお，比較対象として超純水に浸漬させたサンプルも準備し，比較を行った．

3.2　実験結果と考察

Fig.1 より，ファンデーションを塗った人工皮膚を UFB-Air 水中に浸漬すると，その接触面に目に見えるサイズの泡が集まっている様子が確認できた．とくに浸漬後 1 日経過すると，より多くの泡が集合していることが確認できた(Fig.2).

浸漬し，撹拌した場合，超純水では接触面からの剥離，変形は確認されないが，UFB-Air 水では変形が生じた(Fig.3)．さらにそれを 1 日経過させたものでは，変形に加え剥離している様子が確認できた(Fig.4)．以上をまとめると，UFB はまず，異種材料が付着する界面（段差部）に集まり，目に見えるサイズの大きさの泡になる．その後，攪拌などの外力を加えると，その泡が破泡し，材料表面では変形を促し，界面では剥離を促しているものと考えられる．とくに，Fig.4 で UFB-Air 水に浸漬されたファンデーションの表面には微細なディンプルのような形状が確認できるが，これは UFB が破泡する際に発生するマイクロジェットによるものだと考えられ，このような物理的な作用がファンデーションの変形や剥離に寄与したものと考えらえる

4　結　　言

本研究では，人工皮膚モデルに塗布したファンデーションが UFB 水および超純水中でどのような挙動を示すかについて検討を行った．その結果，超純水中ではとくに変化が生じないのに対し，UFB 水中に浸漬，あるいは攪拌したものではファンデーションの変形や剥離が確認された．これは UFB が特定の場所に集合し，サイズ大きくなるとともに，その泡が破泡する際に生じるマイクロジェットがファンデーション表面・界面に物理的に作用した結果であると考えられる．


UFB-Air　　Ultra-Pure Water

Fig.1　Artificial skin model immersion only


UFB-Air　　Ultra-Pure Water

Fig.2　After 1 day of immersion


UFB-Air　　Ultra-Pure Water

Fig.3　Immediately after immersion agitation


UFB-Air　　Ultra-Pure Water

Fig.4　After 1 day of immersion agitation

参考文献

1) 九州環境エネルギー産業推進機構，ファインバブル活用事例集, 2018; p1-p5.　(2024 年 1 月 18 日　アクセス)
2) 秦隆志，西内悠祐，田中克也，坂本正與，ファインバブルを用いた洗浄技術．表面技術 2018；69 : 10 号; p8-p12.
3) 早坂信哉，岩間優子，野々山昌生，マイクロバブルバス入浴の角層水分量・保湿への影響．日本健 康開発雑誌 2023.4.23；p3-p4.
4) 寺坂宏一,氷室昭三，安藤景太，秦隆志,ファインバブル入門(日刊工業新聞社，東京,(2016)；p187-p188.

奨励賞受賞論文

パウダージェットデポジションの付着現象ダイナミクス解明と新しい歯科治療への応用展開

久慈千栄子*

1. 緒　言

現在広く普及している歯科治療法は，う蝕（虫歯）部を除去し，う蝕の除去により生じた空洞（窩洞）を歯科材料によって充填させる手法である [1]．しかしながら，口腔内は温度や pH の変化が激しい過酷環境であり，歯科材料と人歯との材料特性の違いは歯科材料の変形を引き起こし，歯科材料と窩洞界面から齲蝕が再発してしまう [2]．そのため，人歯と機械的性質が類似した新たな歯科材料，および歯科材料と人歯を強固に密着させる新たな治療法が求められている．

著者らは，高速粒子衝突加工（Powder Jet Machining, PJM）を歯科治療へと応用する試みを進めてきた．元来 PJM は金属やセラミックス等の材料粒子を用いた噴射加工法であり，材料粒子を対象物に高速衝突させることにより対象物の除去や衝突粒子の付着が可能である．前者の除去加工は Abrasive Jet Machining（AJM）[3]，後者の付着加工は Powder Jet Deposition（PJD）[4]と定義される．どちらも常温大気圧環境下で適用可能であり，噴射粒子の粒径や衝突速度（v），衝突角度（α）等の加工条件に依存して AJM と PJD は遷移する．特に PJD は特徴的な手法であり，一般的な噴射・付着加工である溶射法 [5]やコールドスプレー法 [6]，エアロゾルデポジション法 [7]のように高温や真空などの環境的制約を受けない．そのため PJM は口腔内環境に直接適用でき，歯の主成分であり生体親和性が高い塩基性リン酸カルシウム（$Ca_{10}(PO_4)(OH)_2$）のハイドロキシアパタイト（HA）[8]を噴射粒子に用いることで，革新的な歯科治療が可能となる．本手法では，AJM によりう蝕を除去し，PJD により人工的な歯膜（HA 膜）を構築する（**図 1**）．PJD により作製した HA 膜は応用性が高く，う蝕の発生を未然に防ぐ予防歯科や，歯面表面のホワイトニング等の審美歯科への展開も検討されている [9]．

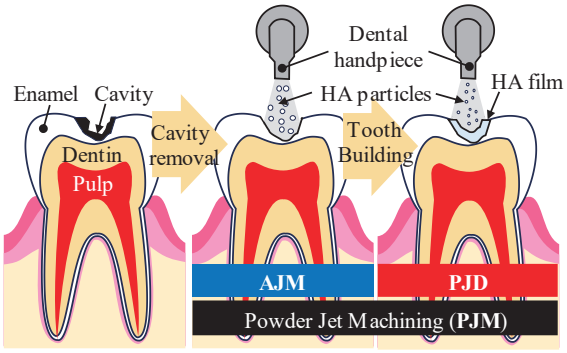

図1　PJMによる歯科治療

＊　東北大学大学院工学研究科機械機能創成専攻：〒980-8579
宮城県仙台市青葉区荒巻字青葉6-6-01
Department of Mechanical Systems Engineering,
Graduate School of Engineering, Tohoku University

本研究では，加工条件の中でも α に着目し，実験と数値流体力学（Computational Fluid Dynamics, CFD）法を組み合わせ，AJM と PJD の遷移条件を示す 3 次元プロセスマッピングを作成した [10)11)]．さらに平滑化粒子流体力学（Smoothed Particle Hydrodynamics, SPH）法によって，PJM における衝突粒子（HA 粒子）と加工対象材料（HA 基板）の破砕挙動 [10)12)]，および応力分布 [13)]を評価した．常温大気圧環境下での HA 粒子の付着ダイナミクス解明のため，PJD 後の HA 粒子および HA 膜の透過型電子顕微鏡（TEM）による観察結果と古典分子動力学（Canonical Molecular Dynamics, CMD）法，SPH 法を組み合わせ，付着加工効率の推定を行った [12)13)]．

本報では，これらの成果を概説する．

2. 実験および解析条件

2. 1　実験条件

PJM には密度 3.109 g/cm^3 の HA 粒子を使用した．HA 粒子は 1～5 μm の粒度分布があり，メディアン径は 2.16 μm であった．加工対象材料には，人歯エナメルと同等の柱状多結晶構造 [14)]を有する HA 基板を用いた．HA 基板表面は研磨し，平滑面の高さを基準高さ（0 μm）と定義して PJM を行った．

PJM には，内部に供給路と加速路の 2 本の流路を有する歯科用ハンドピース形状の装置を使用した（**図 2**(a)）．粒子タンクに充填された HA 粒子は，圧縮空気の供給ガスと共に供給路を通って 2 つの流路の合流地点まで運ばれる．その後，

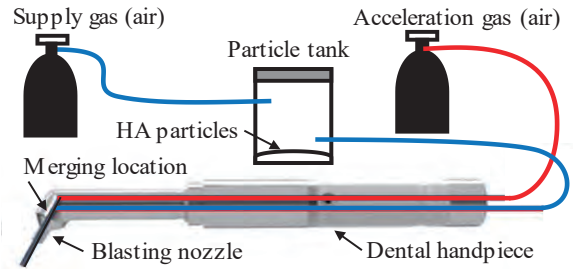

(a)　実験機構の概略図[11)]

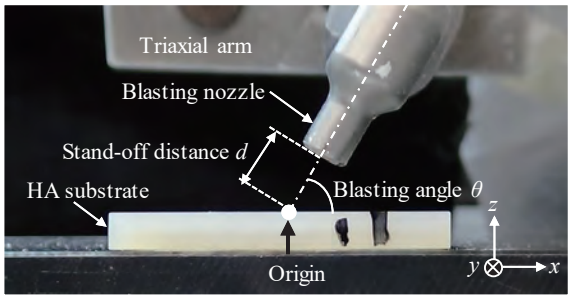

(b)　噴射パラメータの定義[11)]

図2　実験装置

加速路に供給された圧縮空気の加速ガスによりHA粒子は加速され，ノズル先端から噴射される．1 回の実験につき，粒子タンクには 2.0 g の HA 粒子を充填し，供給ガス，加速ガスはそれぞれ0.5 MPaとして定点噴射を60 s行った．付着ダイナミクスの解明のため，PJD に使用した HA 粒子は回収し，回収粒子とHA 膜は透過型電子顕微鏡（TEM）により観察した．

図2(b)は噴射パラメータの定義であり，噴射距離 d，噴射角度 θ，ノズルの中心軸と HA 基板加工面の交点を xyz 軸座標の原点と定めた．d は5.0 mm に固定し，θ を30°, 45°, 60°, 90°に変化させた．加工後の形状は 3 次元形状測定器（NH-3T，三鷹光器株式会社）を用いて測定した．

2．2 解析条件

PJM で噴射した HA 粒子の軌道や v の解析には CFD 法（Ansys FLUENT ver. 15.0）を用いた．乱流モデルには，噴流などの自由流れやきつい流線型カーブなどの解析に適し，ジェット流れにおいて広がり角度をより正確に予測できる特徴を持つ Realizable k–ε モデルを使用した[15]．**図3**(a)の通り，噴射装置の内部流路およびノズル出口から基板に衝突するまでの空間を再現し，加速路からは 0.5 MPa の圧縮空気が流入し，供給路からは 0.5 MPa の圧縮空気と直径 3.0 μm の HA 粒子が噴射されるように設定した．図 3(b)は衝突面近傍のメッシュ構造である．分割メッシュは四面体構造とし，最小サイズ 0.05 μm，最大サイズ 0.3 mm に設定した．壁面での流体の境界層を考慮するため，壁面には層状のメッシュ構造を作製した．図2(b)と同様に d，θ，原点を定義した．

PJM の粒子衝突における HA 粒子および HA 基板の破砕挙動や応力状態の解析には，SPH 法（ANSYS AUTODYN 14.5）を用いた．SPH 法は，解析対称をランダムに分布した粒子（SPH 粒子）の集合体として扱うことで，メッシュ法では解析が困難である大変形問題の解析を行うことができる[16]．図3(c)は構築したモデルの全体図と y = 0 μm における xz 平面の断面図である．HA粒子の形状は，α の変化により破壊現象が変化しないように等方性のある球状とし，PJD に適すると評価された直径 3.2 μm とした[17]．HA 基板は，HA 粒子の衝突領域に 1 辺が 12.0 μm からなる立方体の SPH ソルバーを構築し，その外側を覆うように高さ 18.0 μm，幅 24.0 μm，長さ 24.0 μm の直方体からなる Lagrange ソルバーを作製した．なお，HA 粒子，HA 基板共に SPH ソルバーの SPH 粒子の平滑化距離は 0.1 μm とし，Lagrage ソルバーは z = 0 μm における xy 平面以外に衝撃波を透過させる境界条件を使用した．HA 粒子を v = 300 m/s で HA 基板に衝突させ，Drucker-Prager モデルにより塑性変形挙動を再現した[18]．

PJD における付着メカニズム解明のため，CMD 法を用いた．原子間ポテンシャルは，アルカリ金属ハライドやアルカリ土類金属ハライドなどに代表される，イオン結合性物質の原子間ポテンシャルである Born-Mayer-Huggins（BMH）ポテンシャルを用いた．NVT アンサンブルにより，粒子数 N，体積 V，温度 T を一定とした．MD 法では時間に関する原子の速度および加速度の厳密な積分は困難なため，原子の運動を微小な時間間隔の変化によって段階的に数値積分し，原子挙動を解析する．本研究では数値積分法に精度，簡単性，安定性が高い Verlet 法を採用し，長距離力でのクーロン力は Ewald

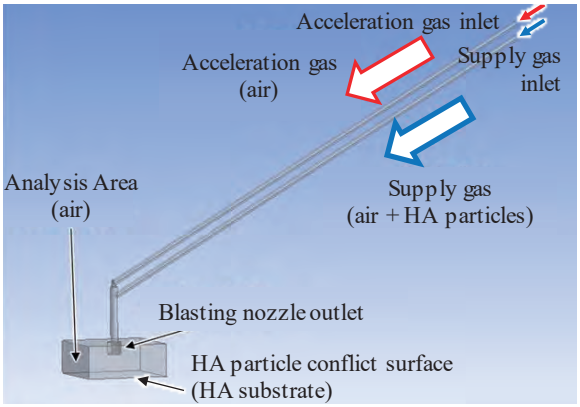

(a) CFD法での解析流路全体図[11]

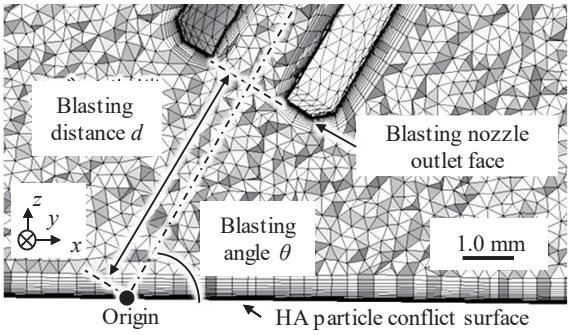

(b) CFD法での噴射パラメータの定義[11]

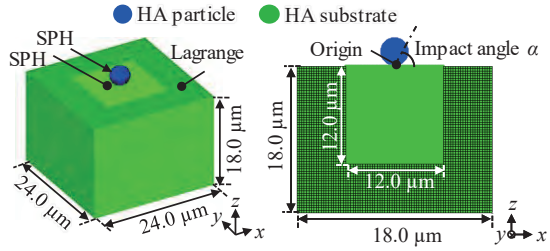

(c) SPH法での解析モデル全体図（左）と断面図（右）[13]

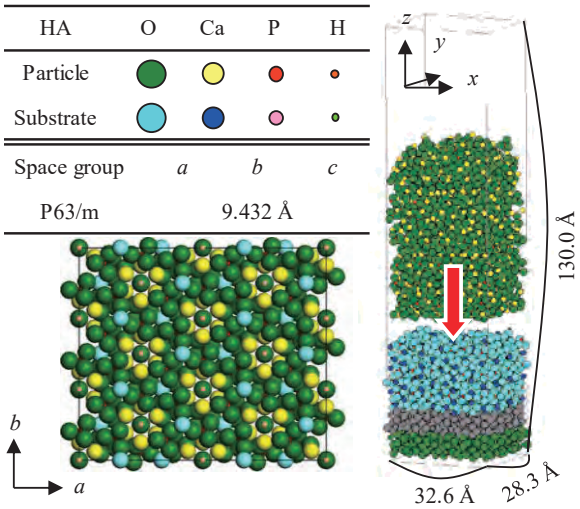

(d) CMD法の基本セル（左）と解析モデル（右）[12]

図3 数値解析モデル

法を用いた．HA の結晶データから六方晶の単位格子を持つ結晶構造を直方体格子に変換して立方体の基本セルを作成し，1 ステップあたり 0.2 fs の緩和計算を 50000 ステップ行った（図 3(d)）．この基本セルを基に原子数 3168 個の HA 粒子，原子数 2640 個の HA 基板のモデルを構築し，衝突面の結晶方位は粒子側を(001)面，基板側を(010)面とした（図 3(d)）．Verlet 法による温度，圧力制御により衝突界面の温度と圧力が緩和されないよう HA 粒子および HA 基板上層の温度制御を行わず，セルサイズは固定して基板中層のみに温度制御を行った．HA 粒子の衝突を受け止めるため，基板下層は原子を初期座標に緩やかに束縛する準固定層とした．

3. AJM–PJD 遷移条件の導出

PJM における AJM と PJD の遷移条件を調査するため，θ を変えながら加工実験を行った．**図 4** は θ = 30°, 60°, 90°で PJM を行った加工面の 3 次元プロファイルである [11]．θ = 30°では AJM が，θ = 90°では PJD が行われたが，θ = 60°では PJD と AJM が同時に行われた．そこで CFD 法により，ノズルから吐出された HA 粒子の軌道，および HA 基板（z = 0 μm の -250 μm < y < 250 μm の範囲）に衝突した HA 粒子の v を求めた．**図 5** は，最も θ の影響が大きい θ = 30°の結果である [11]．図 5(a)より，θ が一定であっても，噴射された HA 粒子は異なる角度（α）と v の分布を持って HA 基板に到達することがわった．α は x 軸の正方向から負方向に向けて鋭角となり，ノズル出口から HA 基板に向かって放射状に広がった．x 軸の負方向および正方向の最端部に衝突した HA 粒子の α をそれぞれ α_1, α_2 と定義すると，θ = 30°の条件では α_1 と α_2 の間で約 12°の差が生じた．図 5(b)より，x 軸方向の衝突位置に依存して v が大きく変化し，x 軸方向の両端の v は急激に低下した．実際の x 軸方向の加工幅は CFD によって求めた HA 粒子の衝突幅よりも狭いことから，x 軸方向の両端において v が低下した HA 粒子は PJM に寄与しないことが推察された．

以上の結果より，PJM における加工現象は，HA 粒子 1 つ 1 つの α と v に依存して遷移すると考えられた．そこで，加工高さ，v, α の 3 次元プロセスマッピングを以下の手順で作成した．まず全ての θ に対し，図 4 の 3 次元測定結果の最大もしくは最小の加工高さを通る xz 断面の二次元プロファイルを作成し，x 軸方向の加工幅 0.1 mm ごとに加工高さの平均値を算出した．同様に，x 軸方向の加工幅 0.1 mm ごとに図 5(b)の v の平均値を算出した．最後に，図 5(a)の α が x 軸方向の位置に依存して線形に変化すると仮定し，x 軸方向の加工幅 0.1 mm ごとの HA 粒子の α を求めた．**図 6** に得られた 3 次元プロセスマッピングを示す [11]．図中の赤色の線が PJD，青色の線が AJM を表している．図 6 から PJD の条件は限定されており，α > 60°の場合に加工高さ 10 μm 以上の加工が行われたことがわかる．v においては約 240 m/s～310 m/s の条件下で PJD が行われ，α の制約はあるものの，v は比較的広い範囲で付着加工が可能であることが明らかとなった．対照的に，α < 60°の条件において除去加工である AJM が行われた．つまり，PJD および AJM の遷移角度はおおよそ α = 60°であることが明らかとなった．特に，低角度の α < 35°かつ v > 310 m/s の条件で加工高さが 20 μm 以上となっていることから，除去加工量を増加させたい場合は，より低い α かつより高い v で PJM を行うのが望ましいといえる．

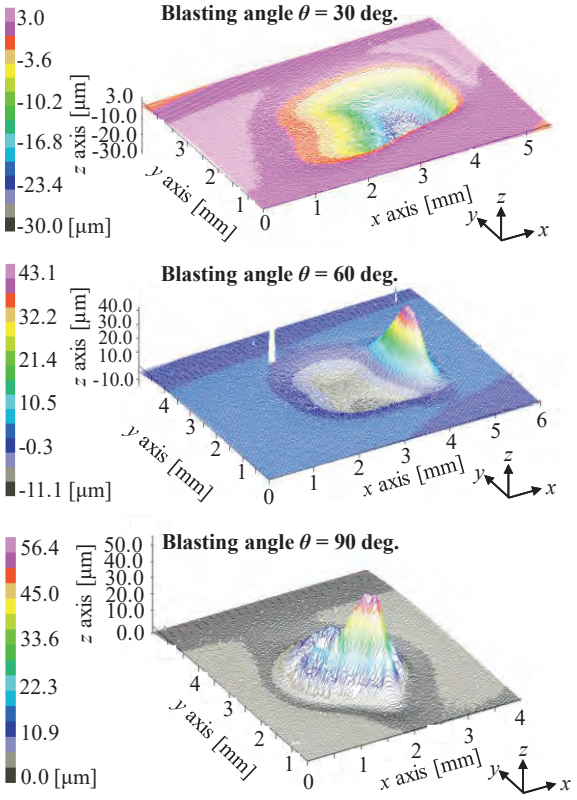

図4　PJMの加工面3次元プロファイル[11]

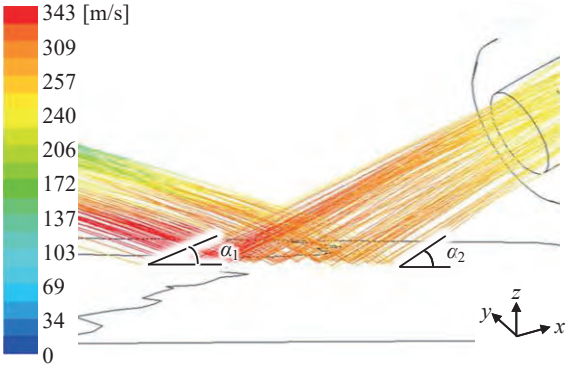

(a) PJMにおけるHA粒子の軌道[11]

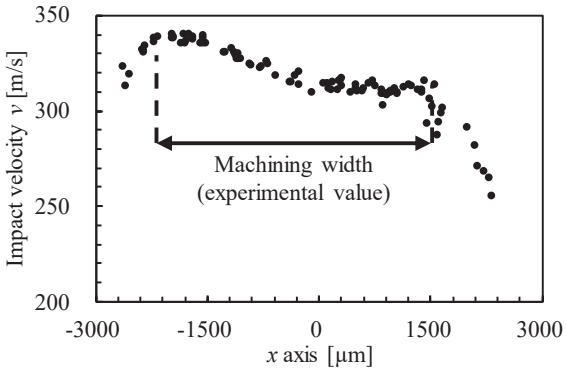

(b) HA粒子の衝突位置ごとの衝突速度[11]

図5　θ = 30°のCFD解析結果

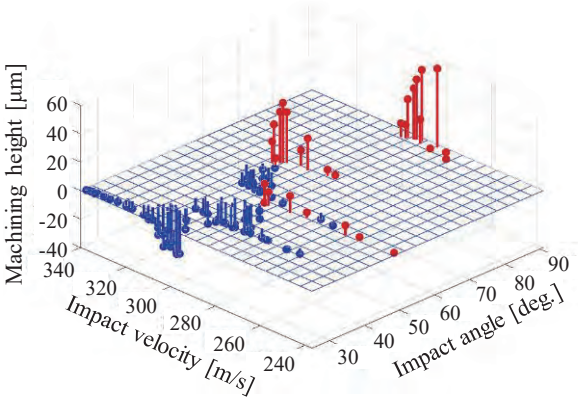

図6　3次元プロセスマッピング[11)]

4. PJM における破砕挙動と応力状態の評価

衝突粒子径が同一の場合，α と v に依存して AJM と PJD は遷移する．その際，HA 粒子と HA 基板がどのような力を受けて変形し，加工に寄与するのかを調査した．**図 7** は SPH 法により求めた PJM における HA 粒子および HA 基板の破砕挙動と応力分布である [13)]．全ての図は y ＝ 0 μm における xz 断面であり，色調は応力値を意味する．HA 粒子が HA 基板へ衝突した時間を t = 0 s とした場合の t = 0.5～2.5 ns の 1.0 ns ごとの応力分布を示しており，図 7(a), (b)は α = 30°，図 7(c), (d)は α ＝ 90°，図 7(a), (c)は垂直応力，図 7(b), (d)はせん断応力を示している．z 軸正方向が垂直応力値の正方向，x 軸負方向がせん断応力値の正方向である．HA 基板内では α = 30°の条件では粒子の衝突方向に偏った応力が生じ，α = 90°の条件では x = 0 μm の yz 平面に応力が対象に分布した．HA 粒子内では，α = 30°の場合に HA 粒子右下の領域に応力が伝播し，圧縮応力，せん断応力ともに衝突界面で最大となった．α = 90°の場合，HA 粒子は細かく破砕され，HA 粒子内の破断界面に応力が集中した．破断界面の応力方向は HA 粒子をせん断破壊する向きに印加され，衝突界面において最大の圧縮応力が働いた．せん断応力は x = 0 μm の yz 平面に対象に分布した．

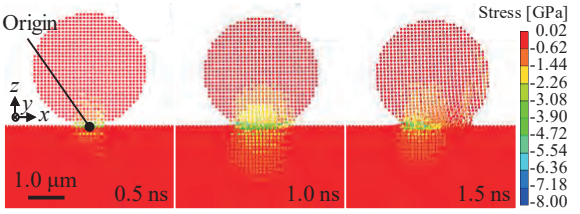

(a) α = 30°の垂直応力分布

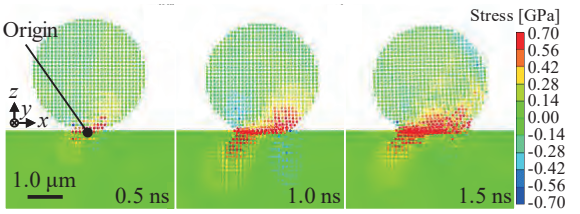

(b) α = 30°のせん断応力分布

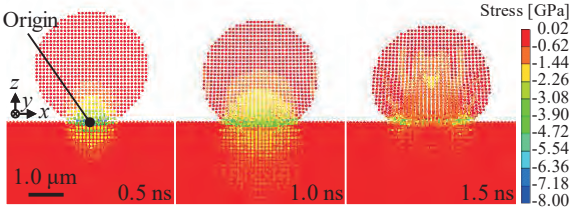

(c) α = 90°の垂直応力分布

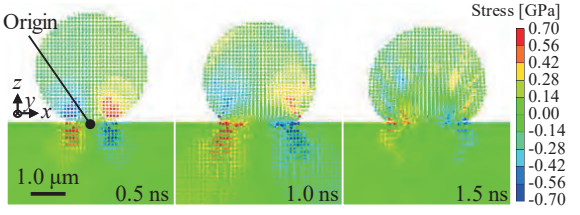

(d) α = 90°の垂直応力分布

図7　SPH法によるPJM解析結果[13)]

一般に材料に内在する引張残留応力はき裂進展を促進させ，逆に圧縮残留応力は抑制する効果がある [19)]．図 7 の通り，PJM では z 軸方向の垂直応力と x 軸方向のせん断応力が同時に発生する．α が大きくなるにつれ HA 基板内の圧縮応力値は大きく，より広域に発生することから，α= 90°で最も亀裂進展が抑制されると推測される．引張残留応力に影響を及ぼすせん断応力は，α= 90°では相殺する方向に発生し，α= 30°では一方向に発生する．そのため，α が小さいほどき裂進展を促進する引張残留応力が大きくなると考えられる．α が小さい場合，衝突界面での熱勾配が大きく，熱応力による脆性破壊も誘発するため [10)]，AJM が支配的になると考えられる．

5. PJD における粒子付着ダイナミクスの解明

PJDにおける粒子付着ダイナミクスを明らかにするため，未使用およびθ = 90°のPJD後に回収したHA粒子，作製したHA膜のTEM観察を行った．**図8**(a)は未使用のHA粒子であり[12)]，直径約0.5～1 μmの結晶からなる多結晶体であった．図8(b)はPJD後の回収粒子であり，図中の粒子Aは緻密な微結晶体へと変質した領域（図8(c)）や，極度の変形を示すひずみの集中領域（図8(d)）が粒子外周部に現れた．図7(c), (d)の通り，HA粒子の破断界面には応力集中が生じるため，粒子Aは PJDに寄与したと推察される．一方，図8(b)の粒子Bのような小粒形のHA粒子は，図8(a)のような均質な結晶性を保ったままであった．小粒形の粒子は質量が小さいため，基板に衝突せずに吹き飛ばされたと推察される．**図9**はθ ＝ 90°のPJDにより作製したHA膜のTEM像であり[13)]，HA膜は図8(c)のHA粒子外周部に確認された微結晶体と同様の数ナノメートルオーダの微結晶体から構成されていた．さらに，HA膜内にはHA基板に対して平行に層状のフレネル縞が生じた．このことから，HA粒子は衝突時の応力付加により微結晶化され，その微結晶領域が層状に堆積してHA膜を形成することが示唆された．また，本研究に用いたHA基板は人歯エナメルと同様の柱状の多結晶構造であるが，HA膜との界面には結晶構造を有さないアモルファス領域が出現した．SPH法から，α ＝ 90°のPJDにおいて，HA粒子とHA基板の衝突界面では最大4.69 GPaの垂直応力，3.85 GPaの圧力が生じたことが明らかとなっている．つまり，PJDの加工面では強加工が行われており，HA基

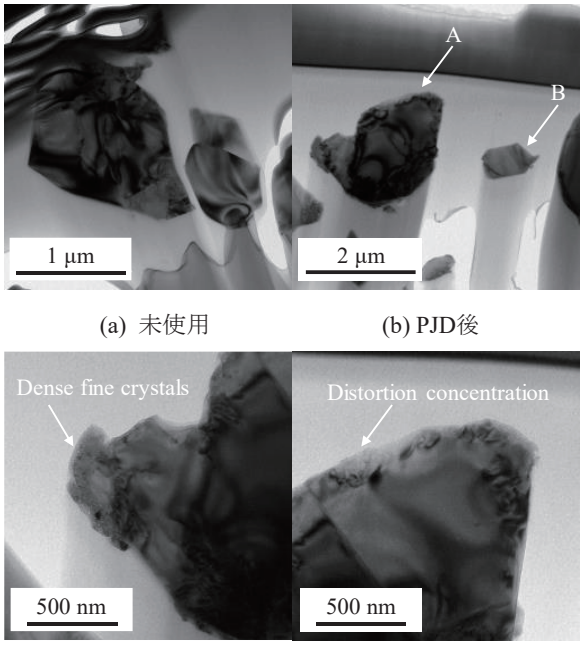

(a) 未使用　(b) PJD後

(c) 微結晶化領域　(d) ひずみ領域

図8　HA粒子のTEM観察結果[12)]

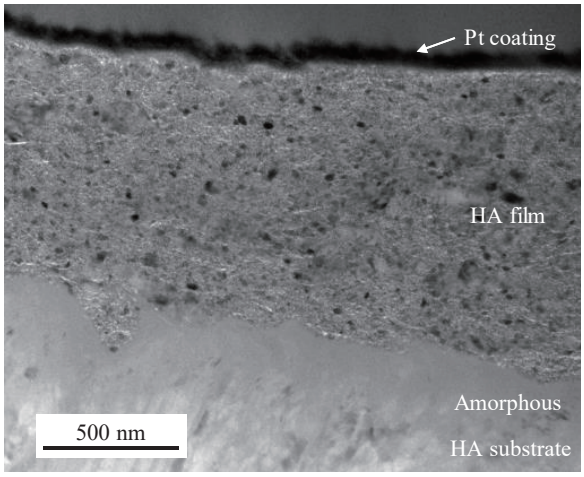

図9　HA膜のTEM観察結果[13)]

板の柱状多結晶構造はHA粒子衝突時の応力に誘起され，固相反応によってアモルファス化したと考えられる．

次に，なぜ粒子が付着するかを調査するため，CMD法による粒子衝突解析を行った[12)]．すると，衝突界面のHA粒子とHA基板の間には新たにクーロン結合が生じており，衝突速度が200～400 m/sの条件で衝突界面での新たな結合原子数が増加することを明らかにした．**図10**は衝突速度300 m/sの原子挙動の経時変化であり[12)]，HA粒子は計算時間3.0 psで最大の押し込みを示し，その後振動しながら結晶構造の安定位置へと移動した．衝突界面の圧力の最大値は，原子の押し込み量が最大となった時点で1.48 GPaを示した．衝突界面に生じた新たなクーロン結合は，衝突時のエネルギが最大となる計算時間3.0 psで最も発生すると考えられる．そこで，PJDでの衝突時に1.48 GPa以上の圧力となったHA粒子の領域を付着可能領域と定義し，SPH法の解析結果から1粒子あたりの付着可能領域の体積割合を導出した．**図11**は，PJDにおける

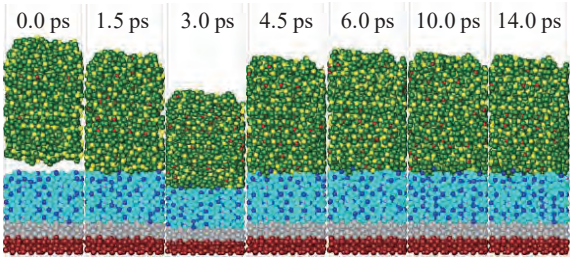

図10　原子挙動の経時変化[12)]

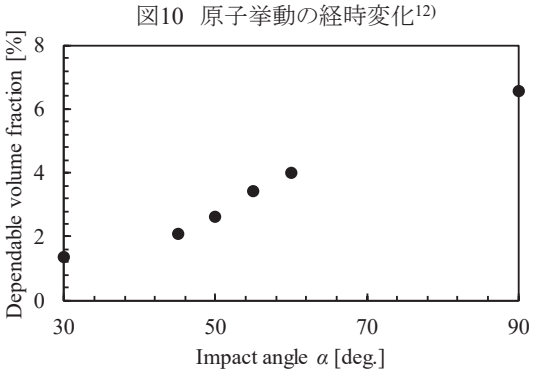

図11　HA粒子の衝突角度αごとの付着可能体積割合

HA粒子の衝突角度αごとの付着可能体積割合であり，αの増加に伴い付着可能領域の体積割合は増加することがわかる．しかしながら，最も付着効率が高いα = 90°の条件であってもその値は6.57%に留まった．すなわち，PJDにおける付着加工の効率は極めて低いと言え，付着効率の向上が求められる．

7. 歯科治療への適用と今後の展望

著者らの基礎検討を基に，歯科応用を目的とした臨床試験，さらに実機での活用を見据えた応用研究に取り組んだ．その後開発された製品「アパジェット」が，令和4年9月9日に知覚過敏用の歯科用医療機器として医療機器承認を受けた．これは，工学部内のみならず歯学部の研究者，さらには関連企業研究者との連携を強力に推進し，共同研究開発に邁進した結果である．医療機器承認に向けた道は困難を極めたが，関係者間の連携をより密にすることで実現するとこができた．

さらに，近年筆者らは，PJDにより作製したHA膜の口腔内耐酸性が人歯エナメルよりも高いことを明らかにした[13)]．人歯エナメルの場合，柱状多結晶構造の粒界から酸の侵入が促進され，時間経過に伴い徐々に溶解する．一方，PJDにより作製したHA膜の粒界は図9のように方向性が低く，人歯エナメルのように有機物などの不純物を含まないため，酸塩基反応により緻密な膜へと改質し，酸の侵入を防ぐのである．しかしながら，θ < 90°で作製したHA膜は膜内に導入された引張残留応力により，耐酸性試験中に剥離してしまう．そのため今後は，剥離の原因となる引張残留応力の導入を抑制する，高効率なPJD加工条件を探索していきたい．

7. 結言

本研究では，複数の数値解析手法と実験を組み合わせ，PJMの加工現象を遷移させる加工条件の1つであるαについて検討を行い，以下の結果が得られた．

(1) 衝突粒子径が同一の場合，αとvに依存してAJMとPJDは遷移し，加工現象の遷移角度はおおよそα = 60°である．PJDはα > 60°かつ240 m/s <310 m/sの条件においてAJMはα < 35°かつv > 310 m/sの条件において加工高さが大きくなる．

(2) PJMにおけるHA粒子とHA基板の衝突時には，z軸方向の垂直応力とx軸方向のせん断応力が同時に発生する．衝突界面において最大の圧縮およびせん断応力が発生し，αが大きくなるにつれHA粒子は細かく破砕される．破砕されたHA粒子の破断界面には応力集中が生じる．αが小さいほどき裂進展を促進する引張残留応力がHA基板内で大きくなり，熱応力による脆性破壊も誘発されるため，AJMが支配的になる．

(3) HA膜は，衝突時の応力付加により微結晶化されたHA粒子が層状に堆積して形成される．衝突界面は新たなクーロン結合が生じており，1粒子あたりの付着可能領域の体積割合はα = 90°の条件で6.57%となる．

6. 謝 辞

本奨励賞へご推薦頂きました東北大学名誉教授 厨川常元先生，絶えずご指導頂きました東北大学教授 水谷正義先生，日本大学准教授 嶋田慶太先生に厚く御礼申し上げます．また本研究を進めるにあたり，歯学的立場から常にご指導・ご協力を頂いた宮城大学学長・東北大学名誉教授 佐々木啓一先生ら，透過電子顕微鏡観察において絶えず親身なご指導頂けた東北大学名誉教授 今野豊彦先生ら，分子動力学法による解析の際にご指導とご鞭撻を賜った東北大学教授 久保百司先生ら，絶えずご援助頂いた株式会社サンギの皆様に深く御礼申し上げます．

7. 参考文献

1) J. W. V. van Dijken: Direct resin composite inlays/onlays: an 11 year follow-up, J. Dent. 28 (2000) 299.
2) H. Askar, J. Krois, G. Göstemeyer and F. Schwendicke: Secondary caries risk of different adhesive strategies and restorative materials in permanent teeth: Systematic review and network meta-analysis. J. Dent. 104 (2021) 103541.
3) R. Melentiev and F. Z. Fang: Recent advances and challenges of abrasive jet machining, CIRP J. Manuf. Sci. Technol., 22 (2018) 1.
4) C. Nishikawa, K. Mizutani, T. Zhou, J. Yan and T. Kuriyagawa: Investigation of particle impact phenomena in powder jet deposition process, Key Eng. Mater., 523-524 (2012) 184.
5) L. Pawlowski: Suspension and solution thermal spray coatings, Surf. Coat. Technol. 203 (2009) 2807.
6) N. Bala, H. Singh, J. Karthikeyan and S. Prakash: Cold spray coating process for corrosion protection: a review, Surf. Eng. 30 (2014) 414.
7) M. Schubert et al: Powder aerosol deposition method - novel applications in the field of sensing and energy technology. Funct. Mater. Lett. 12 (2019) 1930005.
8) L. L. Hench: Bioceramics, J. Am. Ceram. Soc., 81 (1998) 1705.
9) N. Hongo, H. Yamamoto, T. Sunouchi, A. Tomie, K. Izumita, K. Sasaki, K. Shimada, M. Mizutani and T. Kuriyagawa: Restoring tooth color by Powder Jet Deposition, J. Jpn. Soc. Abras. Technol., 65 (2021) 556 (in Japanese).
10) A. TOMIE, C. KUJI, R. AKATSUKA, K. SASAKI, K. SHIMADA, M. MIZUTANI and T. KURIYAGAWA: Study on particle impact angle in powder jet machining (Dental treatment by hydroxyapatite film coating), Trans. JSME, 83, 856 (2017) 17-00169 (in Japanese).
11) C. Kuji, K. Izumita, K. Shimada, M. Mizutani, K. Sasaki and T. Kuriyagawa: Influence of the impact angle on machining in powder jet processing, Int. J. Automation Technol., 17, 1 (2023) 5.
12) M. MIZUTANI, C. KUJI, H. OHISA, S. NISHIMURA, K. MIZUTANI, R. AKATSUKA, K. SASAKI, S. XU, K. SHIMADA and T. KURIYAGAWA: Particle fracture behavior and deposition mechanism in powder jet deposition (PJD), J. Jpn. Soc. Abras. Technol., 61, 1 (2017) 28 (in Japanese).
13) C. Kuji, K. Izumita, K. Shimada, M. Mizutani, K. Sasaki, T. Kuriyagawa: Acid resistance of hydroxyapatite dental films fabricated through powder jet deposition, Mater. Today Commun., 40 (2024) 109564.
14) E. R. Dumont: Mammalian enamel prism patterns and enamel deposition rates, Scan. Microsc., 9 (1995) 429.
15) Ansys Inc.: ANSYS FLUENT 12.0 Theory Guide, (2010) 4-11.
16) G. Yagawa, Y. Kanto, H. Okuda: Computational mechanics, Iwanami Shoten, Tokyo, (2005).
17) K. SATO, C. NISHIKAWA, T. HAGIWARA, K. SHIMADA, W. HORIUCHI, K. MATSUMURA, R. AKATSUKA, K. SASAKI, T. ISHIZAKI, T. ARAKAWA, K. OHTA, M. MIZUTANI and T. KURIYAGAWA: Creation of hydroxyapatite film on human enamel utilized powder jet deposition, Trans. JSME, 79, 808 (2013) 4634 (in Japanese).
18) T. Tanabe, T. Higai, H. Umehara and J. Niwa: Concrete structure, Asakura Shoten Co., Ltd., Tokyo, (1992).
19) J. Vaara, A. Kunnari and T. Frondelius: Literature review of fatigue assessment methods in residual stressed state, Eng. Fail. Anal., 110 (2020) 104379.

Fe-Si-B 系アモルファス合金の組成が熱的組織変化と機械的特性に及ぼす影響

Effect of Fe–Si–B Based Amorphous Alloys Composition on Thermal Microstructural Changes and Mechanical Properties

○学　菅原　悠多（東北大）　　正　久慈　千栄子（東北大）
正　水谷　正義（東北大）

Yuta SUGAWARA, Tohoku University,6-6-01 Aoba, Aramaki, Aoba-ku Sendai, Miyagi
Chieko KUJI, Tohoku University
Masayoshi MIZUTANI, Tohoku University
Key Words: Amorphous alloy, Crystallization, Thermal analysis, X-ray diffraction analysis, Vickers hardness

1. 緒　言

アモルファス合金とは結晶構造を持たない金属材料であり，結晶構造を持つ一般的な金属材料と比較して，さまざまな優れた特性を示す．その中でも Fe 基アモルファス合金は優れた軟磁性を示すため，モータコアへの応用が期待されている．その一方で高強度などの優れた機械的特性が，加工の観点からは悪影響となり，いわゆる難加工性材料でもある．そのため，同合金を製品へ実装するためには加工部における加工性の改善が必要不可欠である．

この課題に対して著者らは同合金の構造変化を利用した加工性改善手法を提案している．アモルファス構造は準安定な構造であり，加熱によって原子のわずかな移動による構造緩和を経て安定な結晶構造へ変化する．例えば著者らの先行研究では，加熱による熱的組織変化によって機械的特性が変化し，アモルファス相と結晶相が混在している組織で最も加工性が向上することを明らかにしており[1,2]，この現象を利用すれば加工性の改善が可能になると考えている．しかしそのアモルファス相がすべて結晶化すると再び加工性が低下することも明らかにしており[1]，結晶化過程の熱的組織変化挙動とそれに伴う機械的特性の変化を詳細に評価することが必要であるといえる．

とくに本研究で対象にしている Fe 基の代表的な組成系である Fe–Si–B 系アモルファス合金の結晶化過程は，Si/Fe と B/Fe の組成比に依存して変化する[3,4]．ただし，そうした複数の組成比の Fe–Si–B 系アモルファス合金に対する詳細な結晶化過程の熱的組織変化挙動と，それに伴う機械的特性の変化を併せて調査した文献は存在しないのが現状である．

そこで本研究では，Si/Fe と B/Fe の組成比が特徴的な 2 種類の Fe–Si–B 系アモルファス合金に対する熱的組織変化挙動を解明し，それが機械的特性に及ぼす影響について検討・考察を加えた．

2. 実験装置および方法

本研究では，厚さ約 25 μm，長さ約 5 mm，幅約 3 mm の組成の異なるアモルファス合金箔，Metglas®2605SA1（以降 SA1 と呼ぶ）と Metglas®2605HB1M（以降 HB1M と呼ぶ）を用いた．

各供試材の組成比はマイクロ波プラズマ発光分光分析装置（MP-AES）と誘導結合プラズマ（ICP）質量分析装置により評価した．また，各材料の熱的組織変化挙動は示差走査熱量計（DSC）による熱分析により調査した．その際，各試験片は Al 製パンに封入し，323 K から 873 K まで 20 K/min で加熱した．873 K 到達後 10 分間等温保持したのち，373 K まで 20 K/min で冷却した．

この熱分析の結果をもとに，各試験片の熱処理温度 T を決定し，示差熱・熱重量同時測定装置（TG-DTA）を用いて熱処理を行った．各試験片は Al_2O_3 製パンに入れ，323 K から T まで 20 K/min で加熱した．T 到達後は等温保持せずに 373 K まで 20 K/min で冷却した．なお，試料の酸化を防ぐため Ar-H_2 還元雰囲気で熱処理を行った．

加熱前の試験片と熱処理を行ったすべての試験片に対して，X 線回折法（XRD）を用いて析出した結晶を同定した．X 線は Cu-Kα 線，管電圧は 45 kV，管電流は 200 mA とした．また，走査型透過電子顕微鏡（STEM）を用いて，試験片の内部組織を観察した．

それぞれの試験片の内部組織と硬さの関係を調査するため，ビッカース硬さ HV を測定した．試験荷重は 500 mN，荷重保持時間は 10 s とした．

3. 実験結果および考察

本研究で用いた 2 種類のアモルファス合金に対して組成比を評価した．その結果，SA1 は Si/Fe が 0.0914，B/Fe が 0.123 であり，HB1M は Si/Fe が 0.0368，B/Fe が 0.150 であることが確認された．すなわち，各合金の Si/Fe と B/Fe の組成比は顕著に違うことが本研究の結果からも確認できた．

以上の各合金に対し，熱的組織変化挙動を調査するために行った DSC による熱分析結果の模式図を Fig. 1 に示す[5]．q_p は熱流束 q の極大値，T_p は q が q_p となる T の値，a は定数である．準安定なアモルファス構造は，安定な結晶構造に相変態する際に発熱が起こる．熱分析ではその発熱を検知し，基準試料との温度差から相変態の挙動を調査できる．同分析の結果，結晶化温度 T_x は SA1 が 781 K，HB1M が 768 K であった．なお，いずれの試料でも 2 つの重複した発熱ピークが確認され，1 つ目の q_p よりも 2 つ目の q_p の方が大きかった．DSC 曲線では，q は極大値をとった後，指数関数的に減少することが知られており，以下の式で表される[5]．

$$q = q_p \exp\left(-\frac{T - T_p}{a}\right) \tag{1}$$

上式より，1 つ目の発熱ピークの減少挙動を表す近似式を最小二乗法により求め，2 つのピークを分離した．すると，1 つ目の発熱反応は 2 つ目の発熱反応と同時に進行したことが推察された．

熱分析の結果からいずれの試料でも 2 つの発熱ピークに起因した相変態が起こっていることが確認できたが，さらに熱的組織変化について詳細に検討するため，XRD による構造解析により析出した結晶を同定した．その結果，いずれの試料でも熱処理を行っていない試料ではアモルファス相によるブロードなピークのみが出現した．Si/Fe が大きい

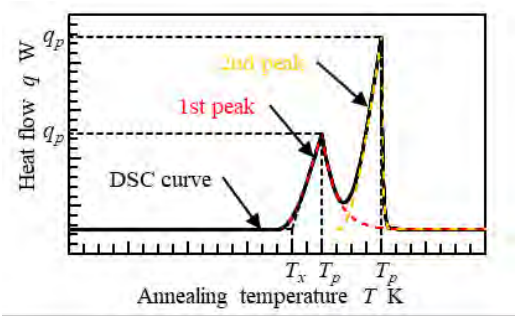

Fig. 1 Schematic diagram of DSC curve

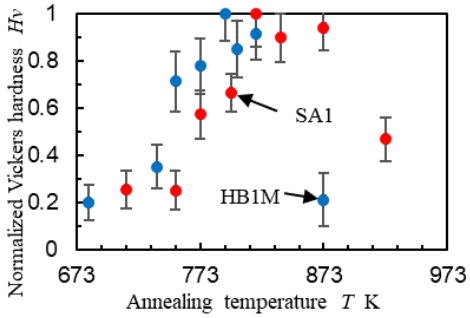

Fig. 2 Change in normalized Vickers hardness by annealing

SA1 では，T = 753 K で Si が固溶した α-Fe が析出した．続いて T = 773 K では Fe_3B，T = 818 K では Fe_2B が析出し，T = 923 K では Fe_3B の存在が確認できなくなった．このことから，準安定な Fe_3B は Fe_2B へと変態したと考えられる．次に HB1M では T = 738 K で α-Fe が析出したが，Si/Fe が小さいため Si は固溶しなかった．その後，SA1 と同様に T = 773 K で Fe_3B，T = 793 K では Fe_2B が析出し，T = 873 K では Fe_3B の存在が確認できなくなった．

熱分析と XRD の結果を比較すると，いずれの試料でも熱分析の 1 つ目の発熱ピークは α-Fe の析出に伴うものであり，2 つ目の発熱ピークは Fe_3B の析出と Fe_2B への変態に伴うものであると考えられる．Zaluska らは，SA1，HB1M と組成比が近い Fe–Si–B 系アモルファス合金において，1 つ目の反応で Fe(Si)固溶体が析出し，2 つ目の反応で Fe_2B が形成されるとしており[3]，この結果とも一致する．また，XRD では SA1 が 753 K，HB1M が 738 K で初めて結晶の析出が確認でき，ともに熱分析により求めた T_x と約 30 K の差があった．これは熱分析と熱処理の際に用いたパンの熱伝導率の違いによるものであると考えられる．

析出した結晶の形状が機械的特性に及ぼす影響を調査するため，走査型透過電子顕微鏡（STEM）像を用いて内部構造を観察した．SA1 では T = 753 K の試料で初晶となる円形の α-Fe(Si)と星形の Fe_3Si が確認された．HB1M では T = 738 K の試料で，デンドライト形状の α-Fe の析出が確認された．この初晶の形状の違いは組成の違いが原因であると考えられる．SA1 では T の増加に伴い結晶相の体積割合が増加し，T = 838 K で完全に結晶化した．また，T = 923 K では結晶成長により，T = 838 K に比べ結晶粒径が大きくなった．HB1M でも同様の傾向が見受けられ，T = 818 K で完全に結晶化し，T = 873 K では結晶粒径が大きくなった．

機械的特性にはさまざまな指標が存在するが，まずは簡便かつ単純に内部構造と機械的特性の関係を調査するため，*HV* を測定した．T と *HV* の関係を Fig. 2 に示す．*HV* は加熱前の *HV* を 0，*HV* の極大値を 1 として正規化したものである．SA1 では結晶が析出していない T = 713 K で加熱前の試料よりもわずかに *HV* が増加した．さらに，T の増加に伴い *HV* が増加し，T = 818 K で極大値をとり，T = 923 K では *HV* が減少した．HB1M でも同様の傾向が確認でき，結晶が析出していない T = 683 K で加熱前の試料よりもわずかに *HV* が増加し，T = 793 K で極大値をとり，T = 873 K では *HV* が減少した．STEM 像と併せて考察すると，SA1 と HB1M は組成の違いに関わらず，結晶が析出するまで（SA1 では 713 K，HB1M では 683 K）は構造緩和によって *HV* がわずかに増加し，結晶化が開始すると結晶相の体積割合が増加するにつれて *HV* が増加した．完全に結晶化が完了すると，T の上昇に伴い結晶粒の粗大化が進み，ホールペッチ効果によって *HV* が減少したと考えられる．また，SA1，HB1M のいずれとも組成および結晶化過程の異なる Fe–Si–B 系アモルファス合金 Metglas®2605S3A でも，同様の傾向が見られた[1]．したがって，アモルファス合金の結晶化と *HV* の関係は，組成や析出する結晶の種類ではなく，結晶相の体積割合に依存すると考えられる．そのため，熱分析や XRD，STEM 像より結晶体積分率を定量的に評価し，引張強度などのより詳細な機械的特性を調査する必要がある．

4．結　　言

本研究では，組成の異なる 2 種類の Fe–Si–B 系アモルファス合金に対して，組成比が熱的組織変化と硬さに及ぼす影響を調査した．本研究で得られた結果を以下に示す．

(1) 組成比の違いによって，熱的組織変化過程が異なる．
(2) 熱処理温度 T の上昇に伴い，はじめに α-Fe の析出が起こり，つづいて Fe_3B の析出と Fe_2B への変態が起こる．
(3) いずれの試料でも，熱処理温度 T が上昇するにつれてビッカース硬さ *HV* が増加し，ある T で極大値をとった後，減少する．結晶化の進行によって *HV* が増加するが，完全に結晶化した後は結晶が粗大化し，ホールペッチ効果によって *HV* が減少する．
(4) 熱的組織変化による *HV* の変化は，結晶相の体積割合に依存する．

謝　　辞

本研究の一部は，JSPS 科研費（23K13228）の助成を受け，文部科学省マテリアル先端リサーチインフラ事業（東北大学構造解析プラットフォーム）（JPMXP1223TU0057）の支援を受けて実施された．

文　　献

(1) C. Kuji, K. Takenaka, M. Mizutani, K. Shimada, T. Kuriyagawa and T. J. Konno, Crystallization Behavior and Machining Properties of Annealed Fe–Si–B–Cr Amorphous Alloys, Journal of Materials Science, Vol. 56, No. 29, (2021), 16697–16711
(2) C. Kuji, M. Mizutani, K. Shimada, K. Suzuki, H. Miura and T. Kuriyagawa, Evaluation of Fracture Properties of Annealed Fe–Si–B–Cr Amorphous Alloys Using Micro-tensile Tests and Blanking Machinability, Materials Science & Engineering A, Vol. 848, (2022), 143483
(3) A. Zaluska and H. Matyia, Crystallization Characteristics of Amorphous Fe–Si–B Alloys, Journal of Material Science, Vol. 18, No. 7, (1983), 2163–2172
(4) M. A. Gibson and G. W. Delamore, Nucleation Kinetics of Primary Crystallization Products in FeSiB Metallic Glasses, Journal of Material Science, Vol. 27, No. 13, (1992), 3533–3538
(5) 齋藤安俊，物質科学のための熱分析の基礎，共立出版，(1990), 111–120

Additive-manufacturing-inspired control for the uniform placement of abrasive grains in grinding wheels

Haruki Matsuzuka[1,*], Yoshinori Izawa[2], Toru Kosemura[2], Masayoshi Mizutani[1,3]

1 Graduate School of Engineering, Tohoku University, Sendai, Japan
2 Nissan Motor Co., Ltd. Yokohama, Japan
3 Tohoku University Green Goals Initiative Research Center for Green X-Tech, Sendai, Japan
*Corresponding Author: haruki.matsuzuka.s2@dc.tohoku.ac.jp

Abstract:
Grinding wheels are made by mixing abrasive grains and bonding materials and then hardening the mixture. However, this process can result in uneven sharpness and reduced machining accuracy. The study puts forth a novel layer-by-layer uniform arrangement of abrasive grains, similar to additive manufacturing. This approach allows significant control over the arrangement of the grains on the surface of the wheel. A blasting technique was used to embed the grains into a bonding-material layer. Uniform placement was achieved by adjusting the air pressure and drying time of the binder. This versatile method based on additive-manufacturing is a promising way to control the placement of abrasive grains.

Keywords : Additive-manufacturing, Blasting technique, Grinding wheels

1. Introduction

Grinding wheels are fabricated by combining abrasive grains and bonding materials and hardening the mixture at high temperatures. However, the random arrangement of abrasive grains in this process reduces the machining accuracy of the grinding wheel. Therefore, controlling the distribution of abrasive grains is important to improve the machining accuracy of grinding wheels[1]. The utilization of additive-manufacturing technology to uniformly place the abrasive grains in one layer at a time can solve this problem[2,3]. An operational method for embedding abrasive grains into the bonding-material layer of a wheel has been developed. However, agglomeration of the grains arranged in layers leads to a loss of uniformity. This study aimed to eliminate the agglomeration and achieve a uniform placement of abrasive grains.

2. Spraying experiments by powder tableting and cutting

2.1 Experimental method

The powder was pressed into a tablet, crushed with a drill, and sprayed to avoid agglomeration. The tablets prepared using the press machine were crushed using a rotating drill to achieve uniform dispersion. The equipment used is shown in **Fig. 1**. The morphologies of the particles before and after cutting were studied using scanning electron microscopy (SEM) to confirm the elimination of agglomeration. Finally, the parameters (of the equipment) were selected to uniformly spray the powder within the target area.

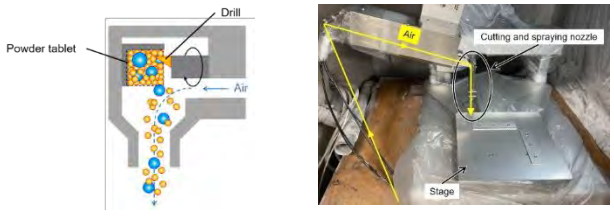

Fig. 1 Tablet cutting method and the appearance of the equipment

2.2 Experimental result

A comparison of the morphology of the particles before and after cutting using SEM is shown in **Fig. 2**, which suggests that the agglomerated powder was crushed during drilling.

Subsequently, the parameters for uniform spraying were selected. The first set of parameters is listed in Condition 1, and the result is shown in **Fig. 3**. Under Condition 1, the spray started before the nozzle moved, and a large amount of powder was sprayed. The tablet was cut before the nozzle passed through the spray area, and a small amount of powder was sprayed at the end of the nozzle movement. Therefore, the waiting time at the starting point was reduced, the scanning method

changed from round-trip to one-way, and the scanning speed increased. The changed parameters are listed in Condition 2, and the result is shown in **Fig. 4**. Under Condition 2, the amount of powder sprayed was no longer biased, and the powder was uniformly sprayed within the target area.

Drill-wear due to the hardness of the particles must be considered when this method is used in the actual production of grinding wheels. Methods for reducing the wear will be considered in the future.

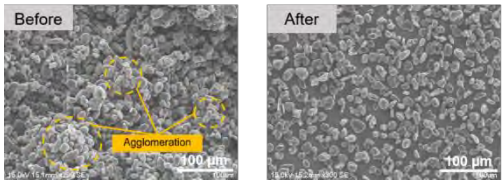

Fig. 2 Comparison before and after cutting

Condition1	
Drill rotation speed[rpm]	1100
Drill feed speed[mm/min]	16
Air pressure[MPa]	0.5
Air flow rate[L/min]	5
Scanning speed[mm/sec]	1
Clearance[mm]	5
Scanning route	Round-trip
Waiting time[sec]	39

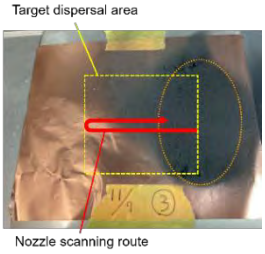

Fig. 3 Spray results under Condition 1

Condition2	
Drill rotation speed[rpm]	1100
Drill feed speed[mm/min]	16
Air pressure[MPa]	0.5
Air flow rate[L/min]	5
Scanning speed[mm/sec]	2
Clearance[mm]	5
Scanning route	One-way
Waiting time[sec]	15

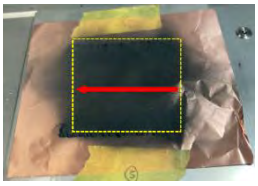

Fig. 4 Spray results under Condition 2

3. Powder blasting experiment on the resin layer

3.1 Powder jet deposition（PJD）method

A powder jet deposition (PJD) method is proposed for embedding abrasive grains in bonding materials. PJD is a precise mechanical coating technique to fabricate functional surfaces with high efficiency[4]. It uses ultrafine particles accelerated to several hundred meters per second by the jet flow of a carrier gas. PJD has been applied to hard materials such as glass and metal substrates. However, in this study, the PJD method was applied to soft resin materials.

3.2 Experimental method

The resin material was applied to the substrate using a squeegee as a bonding agent, dried on a hot plate at 80 °C for 10 min, and then blasted on top of it using a PJD handpiece. Blasting pressure and clearance were set to 0.1 MPa and 5 mm, respectively, and the handpiece was moved back and forth.

3.3 Experimental result

The result of the blasting process is shown in **Fig. 5**. The center of the surface was not sufficiently hardened, resulting in a nonuniform surface. By contrast, the resin attained an appropriate hardness in the peripheral area, and the powder was uniformly distributed.

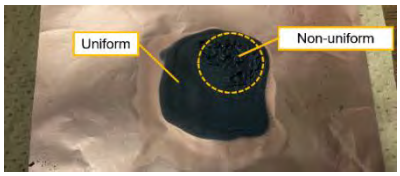

Fig. 5 Result of blasting process

4. Conclusion

The experiments involving powder tableting, cutting, and blasting on the resin layer yielded the following results.

(1) Agglomerated powder was broken into primary particles via tableting and cutting.

(2) Uniform deposition on a desired area was achieved by setting the appropriate parameters.

(3) The powder was placed uniformly by drying the resin to an appropriate hardness value.

In the future, the resin and powder layers will be stacked to approximate the shape of an actual grinding wheel, and the machining accuracy will be evaluated.

ACKNOWLEDGEMENT

This work was supported by Nissan Motor Co., Ltd. (Yokohama, Japan). We would like to thank Editage (www.editage.jp) for English language editing.

REFERENCE

1. Qiu, Y.F. and H. Huang, Research on the fabrication and grinding performance of 3-dimensional controllable abrasive arrangement wheels. International Journal of Advanced Manufacturing Technology, 2019. 104(5-8): p. 1839-1853.
2. Kashimura, S., et al., Development of Resin Fibrous Grinding Wheels Using Twin Nozzle PELID and Analysis of Their Grinding Performance. International Journal of Automation Technology, 2021. 15(1): p. 49-56.
3. Qiu, Y., H. Huang, and X.P. Xu, Effect of additive particles on the performance of ultraviolet-cured resin-bond grinding wheels fabricated using additive manufacturing technology. International Journal of Advanced Manufacturing Technology, 2018. 97(9-12): p. 3873-3882.
4. Kuji, C., et al., Influence of the Impact Angle on Machining in Powder Jet Processing. International Journal of Automation Technology, 2023. 17(1): p. 5-13.

アモルファス合金の組織制御による革新的加工法の開発

Development of Innovative Machining Method by Microstructure Control of Amorphous Alloys

TOHOKU UNIVERSITY

MIZUTANI Lab. × KUJI Lab. Sustainable Manufacturing

アモルファス合金とは

『アモルファス』とは『非晶質』という意味です。アモルファス合金は、一般的な金属材料に特有の『結晶構造』を持たない特殊な構造をしています。この構造は、結晶材料以上の様々な優れた材料特性をもたらします。

アモルファス合金の特性は、元素の種類によって変わります。例えば、鉄を主成分とする(鉄基)アモルファス合金をモータのコア材料として使用すると、エネルギ変換の電力ロスを従来の約1/10まで抑えられる可能性があります。そのため、優れた省エネルギ材料として着目されています。

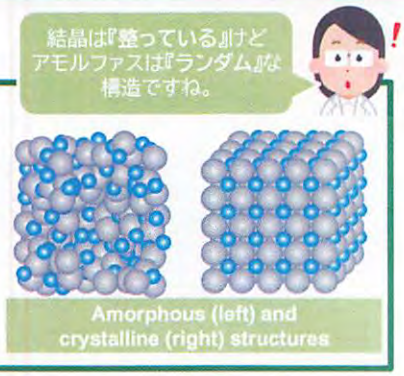

Amorphous (left) and crystalline (right) structures

打ち抜き加工

アモルファス合金のような薄い材料の加工には、『打ち抜き加工』が用いられます。

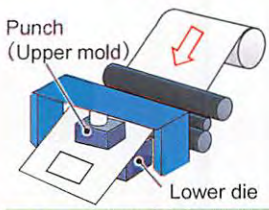

Schematic of blanking

特 徴

- ○薄板/箔の加工
- ○高い生産性
- ○複雑形状も可能
- △工具(金型)が高価

加工の課題

アモルファス構造による『硬くて強くて粘る』という材料特性は、様々な加工不良を引き起こします。

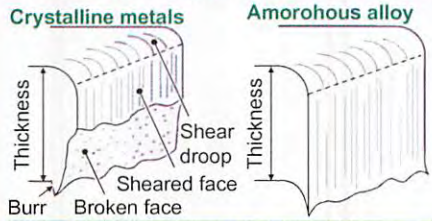

Difference in blanked surfaces

加工不良

- ×巨大なバリ・カエリ
- ×過剰なせん断面
- ×切断不良
- ×深刻な工具摩耗

低品質、高コスト

アモルファス合金の組織制御による革新的加工法

すべての材料特性を支配するアモルファス構造は不安定なため、加熱により容易に組織が変化(結晶化)
⇨ 組織が変化すると、製品に必要な省エネ性も、難加工性をもたらす材料の強さも変化

提案する革新的加工法の概要

①加工で変形・破断する局所領域のみを熱により最適組織に変化

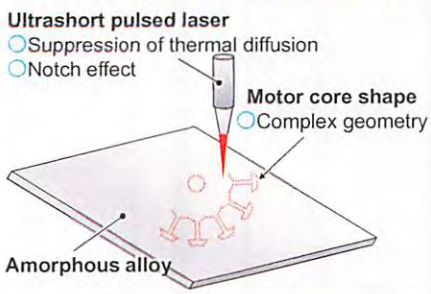

Local heating by ultrashort pulsed laser

②精密打ち抜き加工

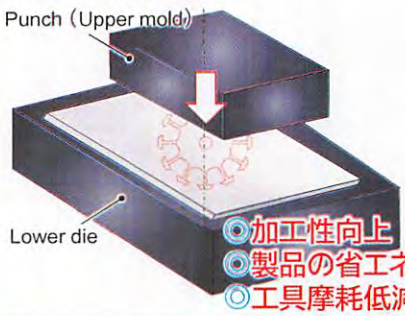

High-machinability blanking

本研究の流れ

材料:Fe基アモルファス合金(Metglas 2605 S3A)

①均質加熱したアモルファス合金に対する基礎検討

熱分析:相転移に伴う発熱/吸熱反応から、結晶化などの相転移現象を調査

熱処理:熱分析結果を基に条件決定

構造解析:X線回折法(XRD)や透過型電子顕微鏡(TEM)観察により、熱処理前後の構造を調査

微小引張試験:加工中に変形・破断する領域に相当する数マイクロメートルサイズの微小試験片の強度を評価

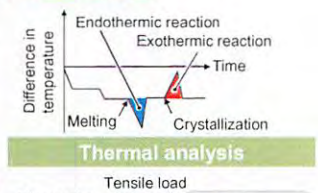

Thermal analysis

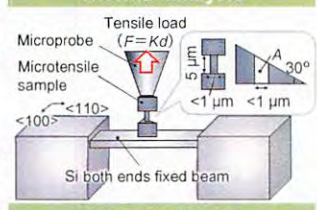

Microtensile test

②局所加熱手法の検討

照射時間がfs～psのパルス光を繰返し照射するレーザを『超短パルスレーザ』と呼びます。瞬時に材料が蒸発するために一般には『非熱加工』が行われますが、熱拡散を抑えながら局所領域のみを加熱する新たな手法を確立します。

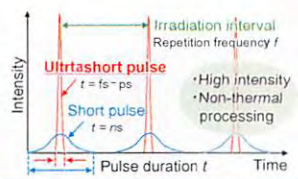

Ultrashort pulsed laser

③打ち抜き加工試験

局所加熱した試料に対し、打ち抜き加工試験を実施

アモルファス合金の組織制御による革新的加工法の開発

Development of Innovative Machining Method by Microstructure Control of Amorphous Alloys

TOHOKU UNIVERSITY

KUJI Lab. Sustainable Manufacturing × MIZUTANI Lab.

①均質加熱したアモルファス合金に対する基礎検討

熱分析：737Kよりも高温で結晶化開始

Heating rate 20K/min

T_g : Grass transition temperature
T_c : Curie temperature

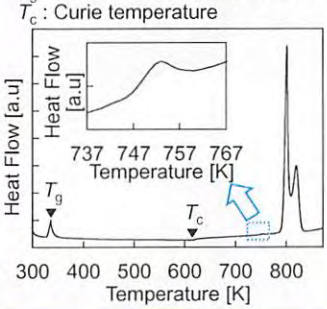

Result of thermal analysis

熱処理：精密な温度制御が可能な熱分析装置内で熱処理

Heat treatment conditions

Sample size	3 mm x 5 mm
Heating/cooling rate	20 K/min
Maximum temperature	713, 753, 763, 773, 873 K

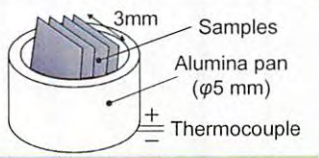

Heat treatment setting

構造解析：試料表層が結晶化したのち、試料内部が徐々に結晶化

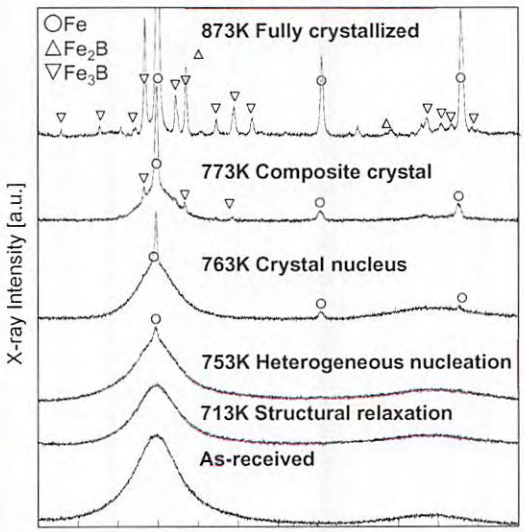

X-ray diffraction (XRD) measurement results

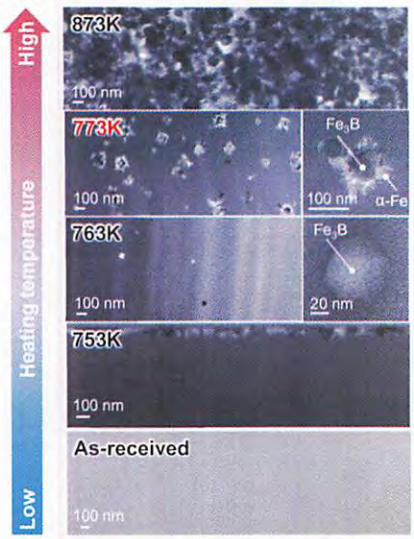

Transmission electron microscope (TEM) images of annealed alloy

微小引張試験：まばらに結晶が析出した構造で強度特性が最も低下

Stress $\sigma = \frac{Kd}{A} = \frac{BEwt^3}{l^3} \cdot \frac{d}{A}$ Strain $\varepsilon = \frac{L' - L}{L}$

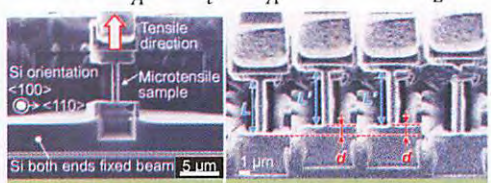

Microtensile test | Snapshots during the test

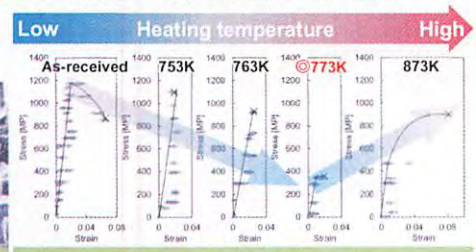

Stress-strain curves

②局所加熱手法の検討

照射条件の調整により非熱加工用途のレーザであってもアモルファス合金が結晶化するほどの熱加工が可能

Laser irradiation conditions

Oscillation central wavelength	1,030 nm
Power	3 W
Repetition frequency	200 kHz
Pulse duration	260 fs
Shot number	100,000

温度勾配が発生し、傾斜組織が形成

Secondary electron image (left) and composition image (right) | Transmission electron microscope (TEM) images of area A to D

Image of thermal processing of ultrashort pulsed laser

③打ち抜き加工試験

Blanking conditions

Blanking velocity	20 mm/s
Size of punch	4 x 12 mm
Clearance between punch and die	2 μm
Radius of tool edge	3 μm
Local heating interval	

Laser irradiation conditions

Oscillation central wavelength	1,030 nm
Power	1 W
Repetition frequency	200 kHz
Pulse duration	10 ps
Shot number	20,000

加工抵抗低減と加工品質向上に成功

As-received (Blanking force：1007.5 N) ⇒ ◎ Local heated sample (Blanking force：881.9 N)

×Excessive sheared face　◎High quality processing

Comparison of blanked surfaces

水谷・久慈研究室

研究室HPは左のQRコードを読み取って下さい。

もっと詳しく知りたい！という方は右の論文QRコードを読み取って下さい。

組織調査　引張試験　品質評価　新加工法

ウルトラファインバブルを用いた高粘度インクの管内摩擦低減

東北大学大学院工学研究科　○松塚　悠希，久慈　千栄子，水谷　正義，日産自動車　魚谷　明日香，髙畑　和弘，小瀬村　透

1. 緒言

自動車産業を始めとする各種産業において，インクジェットプリンティング技術が注目されている．かかる技術は塗着効率が100 %であるとともに，デジタル印刷によるパターニングが可能であることから，無駄のない種々の塗布工程の実現が期待できる．とくにデジタル印刷は従来のアナログ印刷と比較して，CO_2 と揮発性有機化合物（VOC）の排出量を削減できることが示されており[1]，世界的なカーボンニュートラルへの貢献も含めて今後の発展が期待される技術である．しかしその一方で，実際にはインクジェットプリンティング技術は未だ広く採用される状態には至っていない．その理由の一つに，プリンティング時に使用されるヘッドの流路配管が狭く入り組んでおり，圧力抵抗が大きく，高粘度のインクを安定的に吐出することが困難である点が挙げられる．

この課題に対し，著者らはウルトラファインバブル（UFB）を利用し，管内摩擦を低減することで圧力抵抗を下げ，インクの安定吐出を図る新たな手法を提案している．UFB とは直径 1 μm 以下の目に見えない気泡であり，液体中に長期間残存することが知られている．また，この UFB は負に帯電していること，崩壊時に OH ラジカルを生み出すこと，壁面や溝に付着しやすいなどの性質を有していることが知られており[2][3]，様々な分野への応用が期待されている．トライボロジーの観点では，流体中の UFB の存在が流体と固体表面との間の摩擦抵抗を低減させる役割を果たすことが分子動力学シミュレーションによって示されており[4]，摩擦調整剤としても機能することが確認されている[5]．ただし，これまでの研究では水や水溶性クーラントなどの比較的粘度が低い液体に対して UFB が生成され，その効果が検討されてきたが，本研究ではインクという高粘度の液体を対象にすることで UFB の工学的な利用可能性をさらに拡大することができると考えられる．

以上の背景に基づき，本研究では UFB を利用してインクジェットプリンティングにおける高粘度インクの流動特性を改善することを試みた．とくに本報では，配管を想定した流路内の流量について UFB の有無による変化を調べるとともに，その変化とインクに対する接触角との対応について検討・考察を行った．

2. 流量計測実験

2.1 実験方法

本実験の目的は，配管内を流れるインクの流量に対する UFB の影響を調べることである．UFB に管内摩擦を低減する効果があると仮定すると，UFB を生成したインクの流量は UFB を生成していないものよりも大きくなると予想される．本実験ではインクの循環，UFB の生成，流量の計測を同時に行うことができるユニットを構築した．このユニットの外観を**図 1** に示す．また，ここで用いた UFB 生成装置（ノリタケ製）の断面図を**図 2** に示す．この装置はインライン型と呼ばれ，インクが循環する流路の中に組み込むことができる．装置内部には多孔質セラミックス製の管が設置されており，この管の中を通過するインクに対し，外面よりエアーを供給することで UFB が生成されるという機構になっている．この装置を使用し，以下の 3 つの条件で流量の測定を行った．

図 1 装置外観

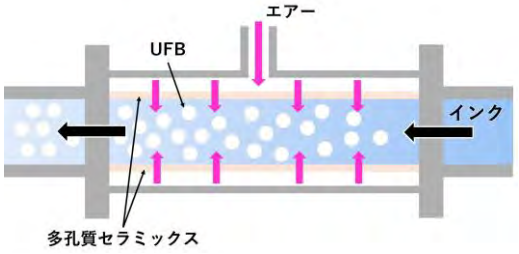

図 2 UFB 生成装置の断面図

表 1 UFB 生成条件

気体種	エアー
気体流量	16 mL/min
気体圧力	0.3 MPa
ポンプ回転数	60 rpm
循環時間	60 min

(i) UFB-generation：UFB 生成ユニットとクランプオン式流量計（キーエンス製 FD-X）をインクが循環する流路に設置し，UFB を生成しながらインクを循環させた．

(ii) Unit：UFB 生成ユニットは設置したままエアーの供給を断ち切り，UFB を生成せずにインクを循環させた．

(iii) Tube：UFB 生成ユニットをチューブに置き換えてインクを循環させた．

(i)における UFB 生成条件を表 **1** に示す．全ての条件において，ポンプの回転数は 60 rpm，インクの循環時間は 60 min に設定し，15 min ごとに流量の測定を行った．

2.2 実験結果および考察

流量測定の結果を**図 3** に示す．0 min 時点での流量は Tube, Unit, UFB-generation の順に大きかったが，15 min 以降は UFB-generation の流量が最も大きく，次いで Tube，Unit の順であった．60 min 時点での UFB-generation の流量は 940.5 mL/min であり，Tube の 743.5

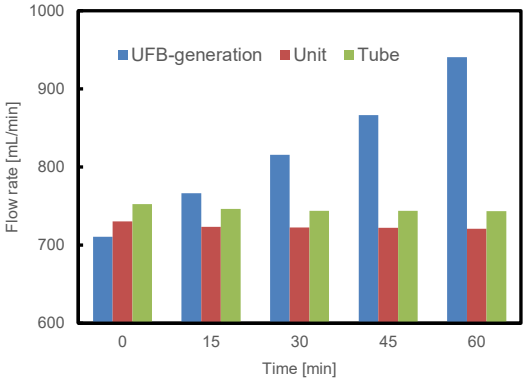

図 3 流量測定結果

mL/min と比較して約 27 %大きかった．循環開始直後の UFB-generation の流量は 710.5 mL/min であることから，UFB の生成によって 60 min で約 32 %流量が増加したことがわかる．Tube, Unit ではそのような傾向は認められず，循環時間が長くなるにつれてわずかに流量が減少した．この結果を踏まえると，UFB を生成しながらインクを循環する条件においては UFB 生成装置を設置することで流路の形状が複雑になり，循環当初は流量が減少するが，循環を続けるにつれて UFB の存在がこの欠点を補い，最終的にはチューブのみの場合と比較して大きな流量をもたらしていると考えられる．この結果は，UFB がチューブの壁とインクとの間の摩擦を減少させることにより，高粘度インクの流れを改善し，インクジェットプリンティングの吐出の安定性を向上させる可能性があることを示唆している．

3. 接触角測定実験

3.1 実験方法

UFB によるインクの流量増加の詳しいメカニズムを検討するため，接触角の測定を行った．接触角は一般的に固体表面の濡れ性を評価するために使用されるパラメータである．水や水溶性クーラントなどの液体に UFB を生成すると液体の表面張力が低下し，接触角が低下することが知られている[6]．前章で認められた流量増加がインクの濡れ性の変化によるものだと仮定すると UFB を生成したインクは生成していないインクよりも接触角が小さくなると予想される．この実験では前章と同様に図 1 の装置を使用し，表 1 の条件でインク内に UFB を生成した．生成後，自動接触角計（協和界面科学製 DM-501Hi）を用いた液滴法によりインクの接触角を測定し，UFB を含まないインクの接触角と比較した．これにより UFB がインクの濡れ性に与える影響について評価した．

3.2 実験結果および考察

接触角測定時の様子と測定結果を**図 4** に示す．左の写真が UFB を生成したインクで，右の写真が UFB を生成していないインクである．測定はそれぞれ 6 回ずつ繰り返し行い，その平均値を記載している．同図より，UFB を生成したインクは，生成していないインクに比べて左は約 11 %，右は約 15 %接触角が低下した．このデータから，水や水溶性クーラントと同様に，高粘度インクにおいても UFB の存在が表面張力の低下につながり，濡れ性を向上させていることが示唆される．このように濡れ性が向上すると，液体と固体表面との界面が滑らかになるため摩擦が減少し，インク

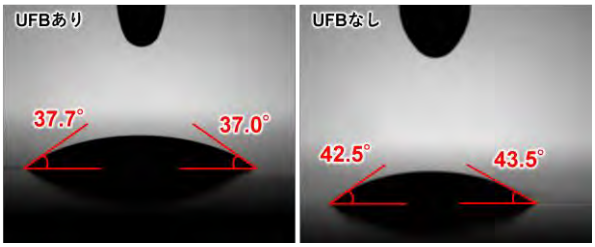

図 4 接触角測定結果

が流れやすくなる可能性がある．以上の結果から，図 3 で得られた流量変化は，UFB の有無によるインクの濡れ性の変化に起因するものだと考えられる．

4. 結言

本研究では，インクジェットプリンティングに用いられる高粘度インクに対する UFB の管内摩擦低減効果を明らかにするため，インク中に UFB を生成し，その流量と接触角を測定する実験を行った．その結果，以下の結論を得た．

(1) UFB を生成しながらインクを循環させ，一定時間が経過すると UFB を生成していないものに比べて流量が大きくなった．また，その流量差は循環時間が長くなるにつれ大きくなった．

(2) UFB を生成したインクは生成していないものよりも接触角が低下し，濡れ性が向上した．

これらの結論は，UFB が高粘度インクの管内摩擦を効果的に低減することを示唆するものである．

謝辞

本研究は日産自動車株式会社との共同研究のもとで行われたことを記し，謝意を表す．

参考文献

[1] Kozake, K, T Egawa, S Kunii, H Kawaguchi, T Okada, Y Sakata, M Shibata, and N Itsubo. 2021. "Environmental Impact Assessment of Flexible Package Printing with the "LUNAJET(R)" Aqueous Inkjet Ink Using Nanodispersion Technology." SUSTAINABILITY 13. https://doi.org/10.3390/su13179851.

[2] 安井久一, 2017. “ウルトラファインバブル” 日本音響学会誌 73 巻 424-431.

[3] 久保和弘, 2020 “ファインバブルの機能特性” 日本家政学会誌 71 巻 124-128

[4] Lu, Y. 2019. "Drag reduction by nanobubble clusters as affected by surface wettability and flow velocity: Molecular dynamics simulation." TRIBOLOGY INTERNATIONAL 137: 267-273. https://doi.org/10.1016/j.triboint.2019.05.010.

[5] Nakagawa, M, A Kioka, and K Tagomori. 2022. "Nanobubbles as friction modifier." TRIBOLOGY INTERNATIONAL 165. https://doi.org/10.1016/j.triboint.2021.107333.

[6] 小林秀彰, 上條雄樹, 平野正浩, 荒木和成, 2020.” ウルトラファインバブル生成技術のクーラントへの適用と研削加工の高能率化” 2020 年度精密工学会春季大会学術講演会講演論文集, I41.

Reduction of friction in high-viscosity ink tubes using ultrafine bubbles

Haruki Matsuzuka[1], Asuka Uotani[2], Kazuhiro Takahata[2], Toru Kosemura[2] and Masayoshi Mizutani[1,3,#]

1 Graduate School of Engineering, Tohoku University, Sendai, Japan
2 Nissan Motor Co., Ltd. Yokohama, Japan
3 Tohoku University Green Goals Initiative Research Center for Green X-Tech, Sendai, Japan
Corresponding Author / Email: masayoshi.mizutani.b6@tohoku.ac.jp , TEL/FAX: +81-22-795-6946

KEYWORDS: Ultrafine bubbles, Friction, High-viscosity ink

This study explores the use of ultrafine bubbles (UFBs) to tackle a major challenge in inkjet printing technology: reducing friction in pipes that carry high-viscosity ink. Inkjet printing, known for its 100% coating efficiency, has substantial potential to contribute to global carbon neutrality, especially in industries like automotive manufacturing. However, the narrow and complex flow channels in inkjet systems create high-pressure resistance, impeding the stable dispensing of high-viscosity ink. UFBs—bubbles smaller than 1 μm—help reduce this friction. This research measured ink flow rates with and without UFBs, revealing that UFBs significantly increase flow rates over time, indicating reduced friction and improved stability in ink discharge. Furthermore, ink with UFBs exhibited a smaller contact angle compared to ink without UFBs, enhancing wettability. These findings suggest that incorporating UFBs into inkjet printing could improve the reliability and efficiency of industrial applications, fostering future technological advancements.

1. Introduction

Inkjet printing technology has the potential to significantly advance global carbon neutrality, particularly in industries such as automotive manufacturing, due to its 100% coating efficiency and digital printing capabilities. Digital inkjet printing has been shown to reduce CO_2 emissions and volatile organic compounds (VOCs) compared to conventional analog printing[1]. However, the technology's widespread adoption is limited by challenges associated with high-viscosity inks used in certain applications. Specifically, the narrow and complex flow channels in inkjet printers create high-pressure resistance, complicating the maintenance of stable and efficient ink flow. To address this issue, this study explores the use of ultrafine bubbles (UFBs) as a novel solution. UFBs—invisible bubbles smaller than 1 μm—have unique properties that allow them to remain suspended in liquids for extended periods. Previous studies have confirmed through molecular dynamics simulations that UFBs reduce the frictional resistance of fluids and act as friction modifiers[2][3]. This research investigates the potential of UFBs to improve the flow characteristics of high-viscosity ink in inkjet printing, aiming to enhance the technology's reliability and broaden its industrial applicability.

2. Flow Rate Measurement

2.1 Experimental method

The experiment aimed to investigate the effect of UFBs on reducing friction in pipes carrying high-viscosity ink. The setup included a UFB generation device and a flow meter installed in the flow channel, as shown in **Fig. 1**. Three ink configurations were tested: (1) UFB-generation, where UFBs were introduced into the ink flow; (2) Unit, where the ink flowed without UFB generation; and (3) Tube, where the UFB device was replaced with a simple tube. Flow rates were measured at 15 min intervals over a 60 min period.

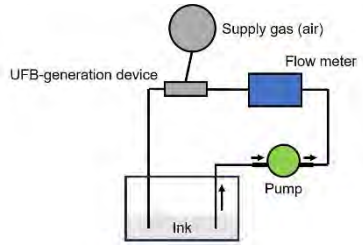

Fig. 1 Schematic of the ultrafine bubble injection setup

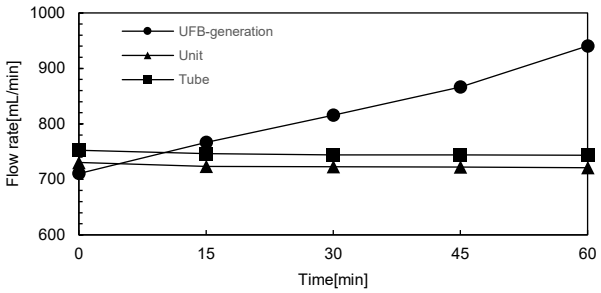

Fig. 2 Flow measurement results

2.2 Result and discussion

The flow measurement results are shown in **Fig. 2**. Data indicated that the flow rate was highest in the UFB-generation configuration, followed by the Tube, and then the Unit. The flow rate of the UFB-generation ink increased over time, while the other configurations remained constant. Although the installation of the UFB-generation device complicated the flow path and initially reduced the flow rate, the generation of UFBs ultimately compensate for this disadvantage, resulting in a higher flow rate compared to tubing alone. These findings suggest that UFBs reduce friction in the pipes, thereby improving the flow of high-viscosity ink and potentially enhancing inkjet printing efficiency.

3. Contact angle measurement

3.1 Experimental method

Contact angle measurement experiments were conducted to evaluate the effect of UFBs on ink behavior. The contact angle is commonly used to assess the wettability of solid surfaces. **Fig. 3** illustrates the contact angle, θ. In this experiment, UFBs were generated in the ink for 60 min using the equipment described in Chapter 2. After this period, the contact angle of the ink was measured and compared to the contact angle of ink without UFBs. The aim was to assess the impact of UFBs on the wetting properties of ink by analyzing the differences between the contact angles of UFB-treated and untreated ink.

3.2 Result and discussion

The contact angle measurement results are shown in Fig. 4. The data indicate that ink with UFBs has a smaller contact angle compared to ink without UFBs, suggesting that UFBs enhances the wettability of liquids. Improved wettability may reduce friction, as the liquid becomes a more effective lubricant and the interface between the liquid and solid surface becomes smoother.

4. Conclusion

In this study, UFBs were generated in ink, and the flow rate and contact angle were measured to assess their effect on reducing friction in high-viscosity ink for inkjet printing. The following conclusions were drawn:

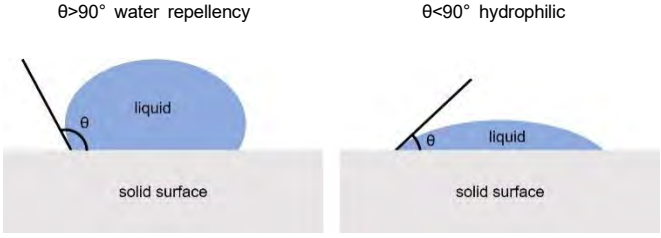

Fig. 3 Definition of contact angle

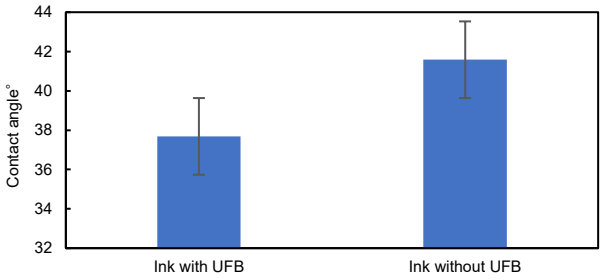

Fig. 4 Contact angle measurement results

(1) The flow rate increased when the ink was circulated through the channel with UFB generation.
(2) Ink with UFBs exhibited a smaller contact angle and better wettability compared to ink without UFBs.

These findings suggest that UFBs effectively reduce friction in high-viscosity ink pipes. Further research is needed to examine the long-term effects of UFBs on ink properties and to optimize the technology for broader industrial applications.

ACKNOWLEDGEMENT

This work was supported by Nissan Motor Co., Ltd. (Yokohama, Japan).

REFERENCES

1. Katsuyuki Kozake, Tsuyoshi Egawa, Satoshi Kunii, Hiroki Kawaguchi, Toru Okada, Yushi Sakata, Manabu Shibata and Norihiro Itsubo, “Environmental Impact Assessment of Flexible Package Printing with the “LUNAJET®” Aqueous Inkjet Ink Using Nanodispersion Technology” Sustainability 2021, 13(17), 9851.
2. Yan Lu, “Drag reduction by nanobubble clusters as affected by surface wettability and flow velocity: Molecular dynamics simulation” Tribology International 137 (2019) 267–273.
3. Masami Nakagawa, Arata Kioka and Ken Tagomori, “Nanobubbles as friction modifier” Tribology International 165 (2022) 107333.

招待講演

超短パルスレーザーによるアモルファス合金の局所組織改質

Local structural modification of amorphous alloys using ultrashort pulsed lasers

久慈　千栄子(東北大学)

Chieko Kuji (Tohoku Univ.)

1.

1.　はじめに

一般的な金属材料は，原子同士が長周期的な規則性を持ちながら整列する，いわゆる結晶からなる材料組織を有する（図 1(a)）．対してアモルファス合金は，溶湯状態からの急冷により結晶化温度以下でも液体状態を保ち（過冷却液体），ガラス転移温度にて液体のようなランダムな原子状態を保ったまま固化する（図 1(b)）．つまり，アモルファス（Amorphous）とは“非晶質”の意であり，結晶を有さない合金材料をアモルファス合金と呼ぶ．

アモルファス合金は，その稀有な材料組織に起因して結晶金属では得ることが出来ない優れた材料特性を発現する．例えば，結晶粒界や転位，積層欠陥などの腐食の起点となる欠陥を含まないため，耐食性が高い[1]．また，そもそも結晶が存在しないため結晶磁気異方性がなく，形状磁気異方性の原因となる粒界や介在物による磁壁のピン止め効果を示さないため高い軟磁性を示す[2]．加えて，アモルファス合金は製造方法に起因して厚み 20 μm 程度の箔帯形状となるため（図 2），材料厚みに依存して発生する渦電流損失もほとんど無視できる．さらに，結晶金属特有の転位のすべりによる変形形態を持たず，加工硬化も生じないため，高硬度，高強度と共に強靭性も有する．以上の様々な材料特性の中でも特に磁気的特性が着目されており，高い磁束密度を示す Fe 基合金は省エネ性を活かしたモータ磁心材料として期待されている[3]．これらの優れた材料特性を有するにも関わらず，現状のアモルファス合金の生産量は軟磁性材料の総生産量の 2～3%に留まっている[4]．

著者らは，本合金の普及を妨げる最大の要因である難加工性を克服するため，アモルファス合金の組織と材料特性の関係に着目した加工手法開発を推進している．本稿では，超短パルスレーザーの活用を中心として著者らのこれまでの取り組みを紹介する．

2.　逆転の発想から生まれた加工法開発
～光で加熱し“弱く”する～

アモルファス合金のような薄い材料の量産加工には，プレス加工の一種である打ち抜き加工が用いられる．この加工では，パンチとダイという一対の工具を使用する．工具間の隙間（クリアランス）で生じる材料の塑性変形と破断を活用し，目的形状へと切断する加工法である．一般的

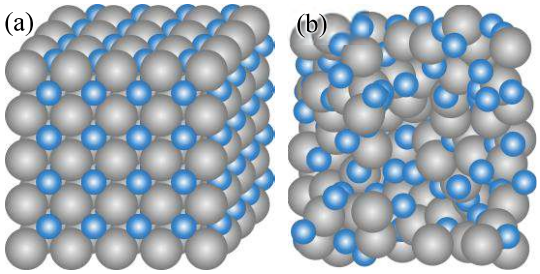

図 1　(a)結晶金属および(b)アモルファス合金の原子配列の模式図


図 2　アモルファス合金の箔帯形状

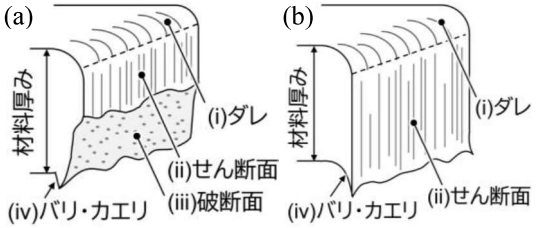

図 3　(a)結晶金属および(b)アモルファス合金の打ち抜き加工面の模式図

な結晶金属の打ち抜き加工面は，(i)塑性変形によって生じるダレ，(ii)材料の延びにより形成されるせん断面，(iii)クラックの進展により形成される破断面，(iv)加工不良の一種となるバリやカエリの 4 つの領域から構成される（図 3(a)）．しかしアモルファス合金の場合，極端に靭性が高いため，(ii)のせん断面が加工面全面に出現し，結果として(iv)のバリやカエリが生じる．さらに，高強度という特性は切断に必要な力（加工抵抗）の上昇をもたらす．特に，(ii)のせん断面は工具と材料の摩擦によって形成されるため，深刻な工具の損傷を引き起こす．打ち抜き加工に用いられる工具の相場価格は 1 組当たり数千万円であり，高価な工具の寿命低下が加工費の高騰をもたらし，製品の採算が合わなくなる．この点が，アモルファス合金の普及を妨げる最大の課題といえる．

そこで著者らは，アモルファス合金の全ての材料特性を支配するその特徴的な材料組織に着

目した．アモルファス合金は準安定な材料であるため，加熱により安定な組織へと変化する（結晶化）．この結晶化は，脆化や軟磁性の低下をもたらすことが知られており，従来は材料の劣化として捉えられていた．しかしながら著者らは，逆転の発想により，加工に寄与するクリアランスの局所領域のみを熱により変質させて弱くすれば，製品性能は維持したまま加工性のみを向上させることができるのではないかと考えた．その際，熱変質領域が大きくなるほど軟磁性の低下をもたらすため，あえて“非熱加工”に用いられる超短パルスレーザーに着目し，熱拡散の抑制を狙ったのである．

3. 超短パルスレーザーによる局所組織改質の一石三鳥の効果

基礎検討のため，Fe 基アモルファス合金の熱的組織変化挙動[5]，および局所領域の強度・靭性の評価[6]を行った．すると，アモルファス合金の機械的特性は組織に依存して大きく変化し，アモルファス相中に結晶がまばらに存在する“結晶化途中の組織”で最も強度や靭性が低下することを明らかにした．この組織において，加工抵抗の大幅な低減も確認されたが[6]，大規模な脆性破壊が生じ，加工品質が低下した[7]．

そこで著者らは，超短パルスレーザーによる局所組織改質を試みた[8]．非熱加工に用いられる超短パルスレーザーであっても，高い繰り返し周波数の場合に蓄熱効果が生じる[9]との報告を受け，蓄熱効果の検証を行った．まず，レーザー照射後のアモルファス合金に対し，走査型電子顕微鏡（SEM）を用いて照射痕の観察を行った．SEM の二次電子像ではレーザーアブレーションによる貫通穴が確認され，組成の影響を示す反射電子像では，前述の貫通穴を中心として等方的に広がる円形のグレーのコントラスト（Glay-area）が確認された．興味深いことに，反射電子像で見られた Glay-area は二次電子像では確認されなかった．これは，何かしらの組成の変化がレーザー照射痕を中心に生じたことを示唆している．この Glay-area の組織を透過型電子顕微鏡（TEM）を用いて詳細に観察した結果，レーザー照射痕中心は粗大な結晶が析出し，照射痕から離れるにつれて結晶の析出が少ない傾斜組織が形成されることを明らかにした．レーザー照射痕中心に出現した組織を著者らの先行研究[5]と照らし合わせると，少なくとも 1073 K 程度の温度で熱処理されたことが推察された．つまり，組織を変質させるほどの高温の熱処理が超短パルスレーザーにより可能であることが確認できたのである．さらに，熱による組織変化の範囲と Glay-area の範囲が一致することも示し，SEM の反射電子像を用いた組織変化領域の簡便な評価手法も確立した．この評価手法を用いて，様々なレーザーの照射条件で蓄熱効果と組織変化の関係を調査したところ，組織変化の程度（結晶化度）と範囲はパルス幅や照射回数の調整により制御できることが判明した．

以上の調査結果を基に，複数の局所組織改質状態のアモルファス合金を作製し，その打ち抜き加工性を評価した．なお，レーザーは工具形状に沿って切取り線のように照射し，局所組織改質した領域をめがけて打ち抜き加工を行った．その結果，基礎検討[6]と同様に，加工抵抗は組織に依存して低減することが判明した．さらに特徴的であったのは，どのような組織の状態であっても材料の切断不良による過剰な延びや脆化による割れの無い高品質な加工面が得られたことである[10]．著者らは，この加工品質向上がレーザーアブレーションにより形成された穴による応力集中の効果であると考察している[11]．さらに，局所的な組織改質では，軟磁性の低下がほとんど生じないことも示している[11]．つまり，レーザーによる局所組織改質は，加工抵抗低減と加工品質向上を両立させるとともに磁気特性も低下させない“一石三鳥”の効果があることが明らかになったのである．

現在著者らは，本技術の社会実装を目指し，生産性向上に向けた検討を進めている．

謝辞

当該研究の遂行にあたり，多大なご指導を頂いた東北大学名誉教授厨川 常元先生らに深く謝意を表します．本研究の一部は，JSPS 科研費（23K13228）および天田財団（AF-2022238-C2）の助成を受けたものです．

参考文献

1) 佐藤　駿，実務表面技術 **28** (1981) 556.
2) 若宮　正行，材料 **42** (1993) 771.
3) J. M. Silveyra et al., Science **362** (2018) eaao0195.
4) Amorphous Soft Magnetic Materials Market Forecasts to 2028 (Market Research Consulting Pvt Ltd., 2023) p. 21.
5) C. Kuji et al., J. Mater. Sci. **56** (2021) 16697.
6) C. Kuji et al., Mater. Sci. Eng. A **848** (2022) 143483.
7) C. Kuji et al., Prec. Eng. **82** (2023) 33.
8) C. Kuji et al., Prec. Eng. **81** (2023) 135.
9) S. M. Eaton et al., Opt. Express **13** (2005) 4708.
10) C. Kuji, Proc. 3rd Int. Conf. Adv. Surf. Enhance., Lect. Notes Mech. Eng. (2024) 309.
11) C. Kuji et al., Proc. 20th Int. Conf. Prec. Eng. (2024). (in press)

Relationship between Thermal Microstructural Change Behavior and Mechanical Properties of Fe–Si–B based Amorphous Alloys

Yuta Sugawara

Abstract

Amorphous alloys are metallic materials with no crystalline structure and material properties that differ from those of common metallic materials. Amorphous alloys are expected to be applied to motor cores by taking advantage of their high soft magnetic properties, one of the material properties. The use of amorphous alloys in motor core materials is expected to improve the conversion efficiency of motors and significantly reduce domestic electricity consumption. However, one of the other material properties, excellent mechanical properties, makes machining difficult. In previous studies, new machining techniques that take advantage of thermal microstructural changes in the specific Fe–Si–B based amorphous alloys and the associated changes in mechanical properties have been shown to improve machinability. The alloy had the best machinability with a mixture of amorphous and crystalline phases. Thermal microstructural changes in amorphous alloys vary with composition, but whether the new machining techniques described above will be applicable to other amorphous alloys is not revealed. The relationship between the composition of amorphous alloys, thermal microstructural changes, and changes in mechanical properties is not fully understood, so these relationships need to be clarified for the practical application of amorphous alloys in motor cores.

Chapter 1 outlines preparation methods, compositions, and material properties of amorphous alloys. It is also shown that amorphous alloys are expected to be applied to motor cores by taking advantage of their high soft magnetic properties. It is also noted that a new processing method utilizing thermal microstructural changes has been proposed to solve the difficult processing properties, and that the thermal microstructural change behavior and mechanical properties of amorphous alloys need to be investigated in more detail to develop generic processing methods.

In Chapter 2, differences in thermal microstructural changes with composition were investigated. First, the compositions of two Fe-Si-B based amorphous alloys were analyzed. The composition ratio of Metglas®2605SA1 and Metglas®2605HB1M was Si/Fe = 0.0914, B/Fe = 0.123, and Si/Fe = 0.0368, B/Fe = 0.150, respectively. Therefore, Metglas®2605SA1 is referred to as “Si-rich sample” and Metglas®2605HB1M as “B-rich sample”. Thermal analysis by differential scanning calorimeter (DSC) revealed that each sample had two exothermic peaks, and the crystallization temperatures of the Si-rich and B-rich samples were 780.9 K and 767.8 K, respectively. The peak temperatures and the magnitude of the peak intensity of two exothermic peaks were found to be different. To evaluate the thermal microstructural changes in more detail, several samples were heated at different temperatures, the crystal species were identified by X-ray diffraction method (XRD), and the microstructures were observed using scanning transmission electron microscope (STEM). From these results, Si atoms melted into α-Fe in Si-rich samples, but not in B-rich samples. The contours of the crystals precipitated in the Si-rich samples were linear or curvilinear, while those in the B-rich samples were saw-toothed. Consequently, the activation energies calculated from DSC results by using the Kissinger method reflected the differences in the crystal species precipitated in the amorphous matrix, which was identified by XRD. The elemental distribution was also

investigated by energy dispersive X-ray spectroscopy (EDS), and it was found that the composition affected the type of nucleus crystal and the mechanism of crystal growth.

In Chapter 3, the crystal volume fraction was calculated from XRD, STEM, and DSC results to quantitatively express the relationship between microstructure and mechanical properties. The separation of the exothermic peaks in the DSC curves identified the reaction that caused the two exothermic phenomena. In the first peak on the low-temperature side, crystallization of α-Fe(Si) occurred in the Si-rich samples and α-Fe in the B-rich samples. In the second peak at the high-temperature side, in addition to α-Fe(Si) or α-Fe crystallization, metastable Fe_3B crystallization and transformation from Fe_3B to stable Fe_2B occurred in both samples. In the temperature range where only crystallization occurred, the crystal volume fraction calculated by the three methods agreed precisely. In contrast, in the temperature range where transformation occurs in parallel with crystallization, the crystal volume fraction calculated by XRD and STEM did not agree with those calculated by DSC. This is because the crystal volume fraction calculated by DSC was overestimated due to the effect of heat generated by the transformation. Because the observation of microstructure and the calculation of the crystal volume fraction by STEM require a lot of time and skills, it is preferable to calculate the crystal volume fraction by XRD.

In Chapter 4, Vickers hardness and micro-tensile tests were conducted to investigate the relationship between microstructure and mechanical properties. Atomic stabilization by structural relaxation caused an increase in Vickers hardness. The microstructural strengthening by crystallization caused a rapid increase in Vickers hardness; both the Si-rich and B-rich samples showed similar trends in Vickers hardness and crystal volume fraction. Therefore, the increase in Vickers hardness with crystallization is independent of composition ratio and thermal microstructural behavior and depends only on the crystal volume fraction. In addition, the increase and decrease in the volume fraction of each crystalline species caused the increase and decrease in Vickers hardness in the temperature range where transformation occurred. After crystallization was completed, Vickers hardness decreased rapidly with grain coarsening, partly due to the Hall-Petch effect. Fracture morphology changed from ductile to brittle fracture due to crystallization. Embrittlement by crystallization was caused by the solid solution of Si in the crystals, which contributed to the decrease in tensile strength. The susceptibility to embrittlement due to microstructural changes depended on the position of the alloy composition in the alloy state diagram. The embrittlement susceptibility of the Si-rich and B-rich samples, which are in the hypoeutectic composition, was lower than that of the other amorphous alloys, which are in the hypereutectic composition. The B-rich samples had lower embrittlement susceptibility than the Si-rich samples.

Chapter 5 summarized the results and conclusions of this thesis, also discussing the engineering and industrial significance of this study. In this study, the effects of compositional differences of Fe-Si-B based amorphous alloys on thermal microstructural changes and mechanical properties were investigated. Consequently, the crystal volume fraction, a parameter used not only in amorphous alloys, but also in polymers and other fields, is preferred to be calculated from XRD results. These are engineering significances of this study. Furthermore, the tensile strength of annealed amorphous alloys is closely related to embrittlement, and its tendensy varies depending on the composition. This knowledge can infer mechanical properties such as tensile strength from the results of compositional analysis. This study is of industrial significance because it presents important findings for the practical application of new processing methods for amorphous alloys.

Study on Debris Behavior during Jump Flushing in Die-sinking EDM

Toyoki Hayashi

Abstract

In the Die-sinking electrical discharge machining (Die-sinking EDM) process, an electrode is made of conductive material in a shape that is inverted concerning the shape to be machined, mainly in machining oil, and continuous pulse electrical discharges of thousands to tens of thousands of times per second are generated between the gap between the tool electrode and the workpiece. The heat generated by the electrical energy melts and removes the workpiece, transferring the shape of the electrode to the workpiece. EDM is used in the machining of dies and precision parts, and there is a growing demand for more efficient EDM machining. However, there is a problem the debris generated by the machining process accumulates in the gap between the electrode and the workpiece, causing abnormal electrical discharges. The jump flushing method, in which the electrode is periodically moved up and down to discharge debris from the gap, is used as a means of discharging the debris, but it is difficult to understand the phenomena in the gap, and various analysis methods have been studied to date.

The geometry of the electrode has a significant effect on the process of shaving ejection in the Die-sinking EDM process. Therefore, it is necessary to clarify how the geometry of the electrode influences the shavings ejection process in order to improve the shavings ejection process. The objective of this study is to observe the behavior of debris during jump flushing, compare it with jump flushing simulations, evaluate the validity of the simulations, and study the effect of electrode geometry on the evacuation of debris.

In Chapter 1, the characteristics of EDM in terms of machining methods and the principles of EDM are described. In particular, the jump flushing method, which is a method for discharging debris in the die-sinking EDM process, and the status of analytical methods in Die-sinking EDM are introduced, and the purpose of this study is described.

In Chapter 2, the ejection behavior of simulated debris due to the vertical motion of the electrode in the machining fluid was clarified. Differences between the simulated debris, the effect of jump parameters, and the behavior of the simulated debris were evaluated by particle tracking. For observation experiment, SiC #600 was suitable for observing the simulated debris. When the jump parameter was changed, the simulated debris pulled up by the electrode showed a whirling motion at jump speeds (JS) of 3 m/min or higher. Observation was difficult when the jump-up amount (JU) was less than 1 mm, and the discharge of simulated debris from the machined hole was confirmed at jumps of 2 mm or more. In addition, particle tracking was conducted under SiC #600, JS: 7 m/min, and JU: 5 mm, which were considered optimal based on the above experiments. The results showed that the particle velocities on both sides of the electrode were almost identical, and the maximum velocity of the simulated debris during electrode descent was about 25 mm/s.

In Chapter 3, to investigate the effect of electrode geometry on the evacuation of debris, three-dimensional measurements of a copper electrode were taken, and comparative observation experiments were conducted by rotating the orientation of the electrode sides. The jump-flushing simulations conducted by previous studies were then extended to allow comparison with the observational experiments conducted in Chapter 2. The results of the observation experiments showed that the direction of the discharge of simulated debris was determined by the shape of the bottom surface of the electrode. In the jump-flushing simulation, it was confirmed that in the flat geometry simulation, gas ejection occurred from the moment the electrode descended 0.8 mm, and that a large amount of gas was ejected by the time the electrode descended 2 mm. The simulation with a 100 μm taper showed

that the timing of gas ejection was almost identical to the flat simulation, and the flow velocity was 3.7 m/s near the gap exit, 1 m/s faster than in the flat simulation. In the simulation with a 20 μm taper, the timing of gas discharge was almost the same as in the flat simulation, and the flow velocity was 3.1 m/s near the gap exit, 0.4 m/s faster than in the flat simulation. These results suggest that the tapered shape of the bottom surface of the electrode has little effect during the ascent of the electrode and at the moment of gas discharge, but has a significant effect on the flow velocity near the gap exit when the electrode begins to descend, and that the flow velocity near the gap exit may be proportional to the height of the taper. Comparison between the observation experiment and the simulation showed that the moment of the simulated debris discharge and the moment of gas discharge in the simulation were almost identical, indicating that the simulation results were sufficiently valid.

In Chapter 4, we conducted an observation experiment of simulated debris discharge using a worn electrode, followed by normal electric discharge machining using a worn electrode and three-dimensional measurement of the workpiece surface and electrode to investigate the effect of the taper shape of the electrode on the workpiece surface. As a result, the tapered shape of the bottom surface of the electrode was reduced after a short time of EDM. The results showed that a worn electrode with a 20 μm taper discharged simulated debris from both the left and right sides of the electrode, and that a smaller taper enhanced the effect of debris discharge compared to the discharge of debris with a 40 μm taper. In EDM with a worn electrode, the amount of removal at the corners of the workpiece surface was less than that at the center of the surface due to the effect of electrode wear. This indicates that the influence of electrode wear was more dominant in the shape of the workpiece surface than the taper shape of the electrode bottom surface.

In Chapter 5, the general conclusions of this study are summarized.

Study on Mold Release Phenomenon in Optical Lens Molding

Hiromu FUJII

Abstract

Optical lenses are used in many optical devices such as single-lens reflex cameras, in-vehicle cameras, and projectors. Optical lenses are mass-produced by mold forming, in which glass is heated and melted in a mold and pressed to form glass lenses. However, due to the shrinkage of glass lenses during mold release, wrinkle-like steps with a height of several nanometers to several tens of nanometers may appear on the glass lens surface in concentric circles. These minute steps adversely affect the performance of glass lenses, rendering them unusable as products. In addition, the detection and inspection of two-step mold release is costly, leading to a decrease in production efficiency. Therefore, it is important to eliminate the occurrence of two-step mold release, but the mechanism of this phenomenon itself is currently unknown. In this study, we considered that the two main causes of the step generation mechanism are "(i) the phase transition from the liquid phase to the solid phase of the glass lens during cooling in mold molding" and "(ii) friction between the deteriorated mold surface and the glass lens during molding. Therefore, we simulated the phase transition and molding of glass lenses using the finite element method (FEM) and examined the effects of the phase transition and the friction coefficient of the mold surface on the generation of steps. The friction coefficients of the surfaces of molds that generate steps and those of new, unused molds were measured and compared, and the effects of the friction coefficients of the mold surfaces on the generation of steps were discussed.

Chapter 1 is an overview of this study. The demand for aspherical glass lenses and their molding method, molding, are introduced. The phase transition of glass and mold friction as possible causes of the molding defects that occur during the molding process are also outlined. Finally, the mechanism of step generation is described to elucidate the mechanism from "phase transition of glass lens" and "friction on the mold surface," and the structure of this paper is presented.

In Chapter 2, we focused on the phase transition of glass lenses as the cause of step generation. To visualize the thermal conduction and phase transition, we performed thermal conduction and phase transition simulations on glass lens and mold models. The results of the heat conduction simulation showed that the cooling was insufficient due to the difference in the mold geometry. When cooling across the glass transition temperature (T_g), the phase change progresses from the bottom surface of the center of the glass lens, and the phase state is not uniform on the glass lens surface. The presence of the solid and liquid phases on the glass lens surface causes a difference in shrinkage rate, suggesting that steps are generated at the interface between the two phases.

In Chapter 3, we focused on friction on the mold surface as the cause of step generation. The surfaces of the molds with and without steps were observed using a scanning electron microscope (SEM), and it was confirmed

that the surfaces of the molds with steps had numerous scratches. We also conducted a molding simulation by changing the coefficient of friction on the mold surface and confirmed that the contact force does not work uniformly on the glass lens surface when the coefficient of friction increases. The friction coefficients of the surfaces of the molds with steps and the unused molds were measured, and it was found that the friction coefficient of the surface of the mold with steps was higher. The reduction of the frictional force, which constitutes the contact force, contributes to the improvement of mold release. When the contact force does not work uniformly on the glass lens surface, there is a difference in mold release. Therefore, it is suggested that a difference in shrinkage rate also occurs, and a step is generated at the interface.

In Chapter 4, we introduced the surface coating techniques used in the actual glass lens manufacturing to prevent degradation of the mold surface as shown in Chapter 3. However, few studies have investigated the effect of different mold surface coatings on friction. In this chapter, friction tests were conducted on specimens treated with different coatings to confirm the reduction in the coefficient of friction due to the coatings. To investigate the temperature dependence of the coefficient of friction on the mold surface, friction tests were conducted at different temperatures. The results showed that the coefficient of friction increased with increasing temperature for all coating materials. Based on the results of the friction tests, the coefficient of friction at the actual forming temperature range was predicted. These results suggest that a mold coated with a mold release agent on the precious metal film has the lowest coefficient of friction and prevents the occurrence of steps.

Chapter 5 summarizes the results and conclusions of this thesis, also discussing the engineering and industrial significances. Although there have been studies on molding conditions that inhibit the occurrence of molding defects, there have been no studies that have examined the mechanism of the generation of steps on the surface of glass lenses. In this respect, this study is significant from an engineering viewpoint. It is suggested that the surface treatment by applying a mold release agent with excellent heat resistance to the precious metal film is the best way to suppress the generation of steps on the surface of glass lenses. This is industrially significant.

Study on Efficiency Improvement of Lithium-ion Battery Production with Fine Particles and Bubbles

Haruki MATSUZUKA

Abstract

Lithium-ion batteries (LIBs) are widely used in various applications, such as in portable electronic devices and electric vehicles, due to their high energy density and lightweight properties. However, conventional manufacturing processes for LIBs involve high costs and significant CO_2 emissions. To address these issues, this study aims to improve the efficiency of LIB production using fine particles and microbubbles.

Previous studies on LIB manufacturing have primarily focused on conventional methods, which involve multiple steps such as slurry mixing, coating, drying, and pressing. These conventional manufacturing processes face challenges such as high production costs and significant CO_2 emissions, highlighting the need for a new method to address these issues. This study proposes a novel electrode manufacturing method inspired by additive manufacturing technology, called the 3D printing method. In this method, electrodes are fabricated through three processes: (i) active material dispersal process in which active material particles are dispersed on a current collector, (ii) binder dispensing process in which binder is discharged from the top of the active material layer to form a slurry electrode layer, and (iii) binder drying process in which the entire electrode layer is dried and solvents in the binder evaporate to bond active material particles to the current collector, and between active material particles. This method involves fewer steps compared to conventional methods, making it promising for reducing both production costs and CO_2 emissions. However, each process within this method presents its own challenges. This study aims to address these challenges by developing new techniques based on the deposition of fine particles and resin materials.

In Chapter 1, an overview of lithium-ion batteries, which are widely used in society, is provided, including their history, structure, charging and discharging principles, materials, and conventional manufacturing methods. A new manufacturing method, the 3D printing method, is proposed as an alternative to conventional methods. This method is an electrode manufacturing method consisting of three processes: (i) active material dispersal

process, (ii) binder dispensing process, and (iii) binder drying process. The active material dispersal process has the problems of agglomeration of active material particles and non-uniform placement due to the particles not being fixed. The binder dispensing process has the problem of poor binder dispensing stability. The binder drying process has the problem of long drying time. These challenges of 3D printing as a manufacturing method are discussed, and the purpose and structure of this thesis are outlined.

In Chapter 2, the focus is on the active material dispersal process in the 3D printing manufacturing method. We worked on the disintegration of agglomerated particles and the embedding of particles in the electrode layer. The "tablet cutting method" was proposed as a new approach to break up agglomerated particles. In this method, active material particles are first pressed and hardened into a tablet to create a regular initial state. A drill is then used to cut the tablets of particles at equal intervals to evenly distribute the particles. This is thought to break up agglomerated particles into primary particles, as the distance between molecules is equalized and the force is evenly applied. We developed an apparatus to realize this method, conducted particle dispersal experiments, measured the size distribution of particles before and after cutting, and observed the results using scanning electron microscope (SEM). The findings confirmed that the tablet cutting method can be used to break up agglomerated particles and disperse them as primary particles without further crushing. We also proposed a method for embedding active material particles in the binder layer using blasting and conducted experiments to verify the effectiveness of this method. The binder was discharged onto the current collector to form a binder layer. Active material particles, accelerated by air, were discharged from a blast nozzle to embed them in the binder layer. The blast nozzle scanned the area where the binder was being discharged, ensuring a uniform distribution of particles throughout the binder. Finally, the current collector was placed on a heated hot plate to dry the binder and fix the particles. This method was confirmed to effectively fix active material particles in the binder layer. However, we pointed out that the fixation performance of particles in the electrode layer depends on the drying conditions of the binder and emphasized the need to control the drying rate to fix the active material particles effectively.

In Chapter 3, we studied the binder dispensing and drying processes in the 3D printing method to reduce friction in the tube, improve droplet separation characteristics, and control the drying rate. We proposed the use of microbubbles to improve binder dispensing stability. Microbubbles were generated by installing a microbubble generator with a porous ceramic tube in the circulation channel. The contact angles of the binder with and without microbubbles were measured. The results showed that the contact angle of the binder was reduced by the microbubbles, improving its wetting property. The flow rate was measured under three conditions: with microbubbles, without microbubbles, and when the microbubble generator was replaced with a tube. The results showed that the flow rate of the binder increased with microbubbles, indicating that microbubbles may reduce

friction in the tube. To confirm the effect of microbubbles on droplet separation characteristics, high-speed camera images of the discharge were captured. The results showed that droplet separation from the outlet of the binder with microbubbles improved, though higher pressure was required for droplet discharge. In order to confirm the effect of microbubbles on drying time, the drying time was measured and compared with and without microbubbles. The results showed that microbubbles accelerated the drying rate of the binder. This finding may solve the problem of insufficient fixation performance in the electrode layer discussed in Chapter 1.

Chapter 4 summarizes the key findings of this study. This study proposes a new 3D printing method for the manufacture of lithium-ion batteries, and shows new ways to use technologies related to material discharge, such as tablet cutting, blasting, and microbubbles. In addition, it has the potential to contribute to the realization of carbon neutrality in following the concept of life cycle assessment. These points indicate that the engineering and industrial significance of this research is significant.

【令和６年度卒業生】

	氏名	研究テーマ	所属先・勤務先
学部生	岩藤　誠	ウルトラファインバブル（UFB）と超音波照射の複合による工業汚れの洗浄	進学（工学研究科）
	村上　大空	レーザメタルデポジション（LMD）により積層造形した硬質材の内部組織評価	進学（工学研究科）
修士課程	菅原　悠多	Fe-Si-B 系アモルファス合金の熱的組織変化挙動と機械的特性の関係	株式会社ブリヂストン
	林　豊樹	形彫り放電加工におけるジャンプフラッシング時の加工屑挙動に関する研究	オークマ株式会社
	藤井　大睦	光学レンズのモールド成形における離型現象に関する研究	東京エレクトロン株式会社
	松塚　悠希	微粒子および微小気泡を利用したリチウムイオン電池の製造効率化に関する研究	いすゞ自動車株式会社

【研究室だより】

昨年度の記録的な暖冬とは異なり、本年度の冬は厳しい冷え込みとなりました。しかし、三月を迎え、仙台の地にも春の温もりが感じられるようになり、寒暖差に戸惑いながらも、季節の移ろいを実感しております。

水谷先生・久慈先生による教授・助教の体制となり、早くも 1 年が経過しました。先生方は研究や学生への指導、鞭撻など忙しい日々を送っております。藤田技術補佐員には、事務手続き等の研究室の仕事をサポートしていただいております。

現在研究室には、博士課程（社会人）が 2 名、博士課程後期学生は 1 名、博士課程前期学生（修士）は 2 年生が 3 名、1 年生が 4 名、学部 4 年生が 2 名在籍しております。

本年度も私たち水谷・久慈研究室メンバーは一丸となり、勉学や研究をはじめあらゆる活動に励み、有意義な一年を過ごしていきたいと思います。

令和 7 年 4 月

博士課程前期 1 年　岩藤　誠